DIPLOMARBEIT

Titel der Diplomarbeit

Experimental realization of an interferometric quantum circuit to increase the computational depth

Verfasser

Yannick Ole Lipp

angestrebter akademischer Grad

Magister der Naturwissenschaften (Mag. rer.nat.)

Wien, 2011

Studienkennzahl lt. Studienblatt:	A 411
Studienrichtung lt. Studienblatt:	Diplomstudium Physik
Betreuer:	o. Univ.-Prof. Dr. DDr. h.c. Anton Zeilinger

Contents

1 Quantum computation **1**
1.1 Introduction 1
1.2 Photonic qubits 2

2 The quantum optics toolbox **5**
2.1 Single-photon source 5
2.2 Wave plates 7
2.3 Beamsplitters 8
2.4 Mirrors, fibres and free space 9
2.5 Single-photon detection 12

3 Arbitrary single-qubit unitaries with wave plates **15**
3.1 Implementation with wave plates 16
3.2 A demonstration 18

4 Experimental realization of a Controlled-NOT gate **23**
4.1 Properties of the CNOT gate 23
    4.1.1 Implementation scheme 24
    4.1.2 Optimal components 26
    4.1.3 Modelling imperfect components 27
    4.1.4 Modelling imperfect interference 29
4.2 Experimental realization 32
    4.2.1 Construction notes 32
    4.2.2 Components 36
4.3 Testing the gate: Indicative measures 37
    4.3.1 Truth table 39
    4.3.2 Bell state visibility 41
4.4 Testing the gate: State measures 41
    4.4.1 Quantum state tomography 41
    4.4.2 State measures 43
    4.4.3 Error estimation 44
4.5 Testing the gate: Process measures 45
    4.5.1 Quantum process tomography 45

4.5.2 Process measures 49
4.5.3 Error analysis 51

5 Increasing the computational depth 53
5.1 Universal two-qubit quantum computer 53
5.2 Towards an experimental implementation 55
5.3 Possible issues 60
5.4 Applications 63
5.4.1 Quantum algorithm for systems of linear equations 63
5.4.2 Simulating the two-qubit Heisenberg XY model 67

6 Conclusion and outlook 71

A Useful tables 73

B Source code 75

List of Figures 79

List of Tables 81

Bibliography 83

Chapter 1

Quantum computation

1.1 Introduction

When Richard Feynman first introduced the concept of a quantum computer [1] his motivation was a different one than what should lead to its popularization. He suggested that the difficult task of simulating generic quantum systems might be better suited to a machine operating on the quantum level itself, than it is to a classical computer. But with the beginning coherent control of quantum systems the focus had drifted to a different direction. A series of proof of principle implementations of quantum algorithms that had been developed in the meantime was initiated [2, 3, 4]. Their potential speedup over classical programs, albeit arguably of any practical value here, is most visible in Deutsch's algorithm [5]. Public interest, however, is incited by the opportunities offered through Shor's factoring algorithm [6], the Grover search algorithm [7] and more recently Lloyd's algorithm for systems of linear equations [8].

Sensation has dulled a little as it became clear that practical implementations require resources beyond what quantum systems can offer presently. It is still unclear which system will provide the basis for future applications. Photons, for instance, struggle with the lack of strong nonlinearities that imposes the use of linear optics, but at the same time offer desirable features found in none of the competing quantum systems. Photonic qubits can be manipulated at room temperature, together with their speed and low decoherence, this makes them the obvious candidate for combining aspects of computation and communication. It should be considered that classical computers have found a variety of new applications with the advent of networks, most prominently the Internet. Blind quantum computation [9], for instance, is a procedure that allows to securely, i.e. without revealing the content, perform a (quantum) computation on a remote server.

All quantum system are confronted with the urge of being scalable. KLM [10] have addressed this question with a proposal that shows a path to near-deterministic quantum circuits. Though several refinements [11, 12, 13] the resource requirements remain demanding. Most implementations of photonic circuits therefore rely on a clever use of interference and a measurement-induced nonlinearity. That is, to sift the observed detection events by some indication of success, e.g. a coincidence detection. Fast, efficient and photon-number resolving detectors are required to distinguish the individual outcomes. For miniaturization and to improve the interferometric stability, free-space optics experiments are replaced by chips with integrated waveguides [14, 15, 16].

Currently, the most pressing problem concerns the deterministic creation of single photons. The standard spontaneous parametric down-conversion source [17] impedes the transition from a handful to hundreds and more qubits due to their probabilistic nature and insufficient efficiency.

A new perspective is offered by the one-way computational scheme [18]. Until then quantum computation followed the methodology of the circuit model [19, 20]. The quantum circuit model mimics a proven concept of classical computing. Any quantum algorithm– some unitary operation –is decomposed into a universal set of logic gates. In the one-way computational scheme an entangled state, typically a cluster state [21], serves as an initial resource. Being separated from the actual computation it may be created by probabilistic means without interrupting the process [22]. An algorithm is executed by performing a certain sequence of single-qubit measurements on the cluster qubits. The concept was readily adopted with photons [23]. The required error-correction, a consequence inseparably tied to the nonunitary evolution through measurements, was also demonstrated [24].

Recently, the view has shifted again [25] to Feynman's original intent of using quantum computers to simulate physical systems. In [26] this idea has been concretized by showing how to approximately simulate the unitary evolution of a time-independent Hamiltonian with a quantum circuit. In particular the field of quantum chemistry has attended to this concept [27, 28]. Later the repertoire was extended by a quantum version of the ubiquitous Metropolis algorithm that allows to simulate the equilibrium and static properties of quantum systems [29].

This work is intended to increase the computational depth of photonic quantum systems for both quantum computation and simulation by laying the basis for a universal two-qubit quantum computer.

1.2 Photonic qubits

The quantum analogue to a classical bit is a qubit [30], a two-level system that can live in any superposition of these discrete states. Single photons can serve as a physical body to a qubit. Both its internal (polarization, orbital angular momentum, etc.) and external (spacial path, arrival time, etc.) degrees of freedom can be utilized. It is also possible to use a combination of these which helps to increase the number of available qubits [31, 32]. Most common are *polarization encoding* in which a horizontally polarized photon represents the logical value of 0 and a vertically polarized photon is a logical 1; and *path encoding*, where the presence of a single photon in one of two paths is mapped to a logical 0 and 1, respectively.

A single-qubit state has a graphical representation as a vector on the Bloch sphere (see Figure 1.1).

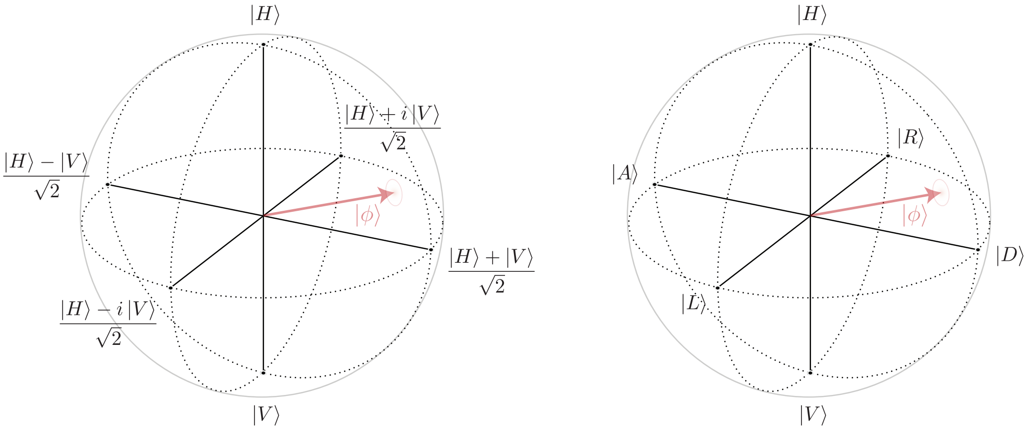
$|H\rangle$
$\frac{|H\rangle + i|V\rangle}{\sqrt{2}}$
$\frac{|H\rangle - |V\rangle}{\sqrt{2}}$
$|\phi\rangle$
$\frac{|H\rangle + |V\rangle}{\sqrt{2}}$
$\frac{|H\rangle - i|V\rangle}{\sqrt{2}}$
$|V\rangle$
$|H\rangle$
$|R\rangle$
$|A\rangle$
$|\phi\rangle$
$|D\rangle$
$|L\rangle$
$|V\rangle$

Figure 1.1: *Bloch sphere. Any pure single-qubit state can be written as a superposition of the computational basis states:* $|\phi\rangle = \eta\,|H\rangle + \nu\,|V\rangle$*, where the amplitudes,* η *and* ν*, are complex numbers restricted by the normalization constraint* $|\eta|^2 + |\nu|^2 = 1$*. A general density matrix* $\rho = \frac{1}{2}(\mathbb{1} + \vec{b}\vec{\sigma})$ *can be described by a Bloch vector* $\vec{b}$*, where* $\vec{\sigma}$ *is the vector of the Pauli matrices* X*,* Y *and* Z*. Pure states lie on the surface, while mixed states are situated in the body of the sphere.*

Chapter 2

The quantum optics toolbox

This chapter briefly introduces the tools available to linear optics quantum computation (LOQC) [33].

2.1 Single-photon source

The interaction of an electromagnetic field induces dipole moments in a dielectric medium. The macroscopic sum thereof is the polarization $\vec{P}$. Expansion with respect to the field $\vec{E}$ yields [34]

$$P_i = \chi^{(1)}_{ij} E_j + \chi^{(2)}_{ijk} E_j E_k + \chi^{(3)}_{ijkl} E_j E_k E_l + \dots \, , \tag{2.1}$$

where the coupling to the field is described by $\chi^{(n)}$ the n-th order susceptibility tensor and $i, j, k, l = \{1, 2, 3\}$. In most materials the nonlinear $\chi^{(n>1)}$ are small and the presence of a strong incident pump light field is necessary to observe higher-order effects. That way a medium with a nonvanishing $\chi^{(2)}$-term can show spontaneous parametric down-conversion (SPDC) [35]. A pump photon with energy, $\hbar\omega_p$, and momentum, $\hbar\vec{k}_p$, spontaneously converts into two photons[1] with energies, $\hbar\omega_s$ and $\hbar\omega_i$, and momenta, $\hbar\vec{k}_s$ and $\hbar\vec{k}_i$. To see a significant contribution a phase matching condition

$$\vec{k}_p = \vec{k}_s + \vec{k}_i \tag{2.2}$$

and energy conservation $\omega_p = \omega_s + \omega_i$ have to be satisfied simultaneously. This can be achieved by setting a specific angle between the pump beam and the orientation of the optical axis in the birefringent crystal [36]. With type-II phase matching [37] signal and idler photon are orthogonally polarized as defined by the orientation of the optical axis. Figure 2.1 explains how to align a crystal such that ordinary and extraordinary axis correspond to H/V polarization, respectively. The correlation in the polarization degree of freedom can be used to generate entangled states [17]. For the purpose of quantum computation this feature is often unnecessary, but here the fact that pairs of photons are created in distinct time intervals is appreciated.

---

[1] They are historically referred to as *signal* and *idler*, as they always appear in pairs. The detection of the signal photon implies the presence of its partner, the idler.

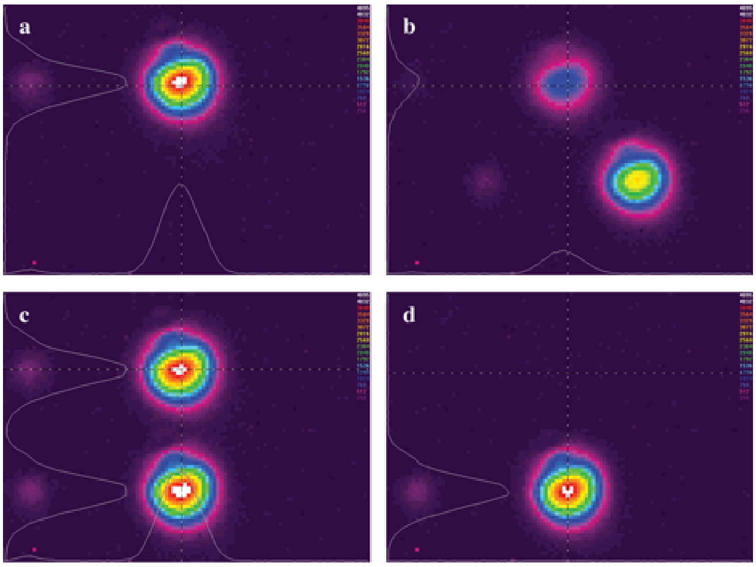

Figure 2.1: *Aligning a nonlinear crystal to be used for SPDC. The crystal is mounted such that it can be rotated in the plain perpendicular to the incident, horizontally polarized light. (a) By convention H is supposed to travel along the ordinary axis. (b) Ordinary and extraordinary axis can be distinguished by rotating the mount. The intensity wanders between two spots. One remains at the same position (ordinary), while the other prescribes a circle around it (extraordinary). (c) Change to D-polarized light to place both spots above each other. (d) Send in V-polarized light to verify that it is aligned to the extraordinary axis.*

The conversion process can occur at random along the length of the medium causing a horizontal walk-off effect. Likewise, the crystal's birefringence is responsible for a transversal walk-off in the extraordinary beam. Both effects can be compensated by another nonlinear crystal with half the thickness [36, 38].

To increase the probability for a coherent multi-pair emission the high energy density of pulsed lasers can be used. Coherence between the pairs is preserved when the pulse length that limits the temporal uncertainty associated with the creation time of the photon pairs is smaller than their coherence time. A shorter pulse duration, however, leads to a broader spectral bandwidth of the pump beam. As a consequence the overlap between energy conservation and the phase matching condition (2.2) increases and a larger range of frequencies is found in the down-converted beams. On the other hand, the coherence time can be extended by spectral filtering. Both the pulse length and the bandwidth of the filter should be adjusted to optimize the count rates. Due to an asymmetry in the phase matching function one of the down-converted spectra grows more quickly than the other [39]. Accordingly, filtering is asymmetric as the spectral bandwidth of ordinarily and extraordinarily polarized photons differ. Therefore an imbalance between H and V is observed.

For the experiments described in this work a femto-second pulsed laser at 789nm was frequency-doubled to pump a 2mm beta-barium borate (BBO) crystal in a non-colinear type-II configuration. In addition filters of 3nm bandwidth were used.

2.2 Wave plates

The polarization state of photons can be manipulated with wave plates. Commonly made of uniaxial birefringent crystals, they induce a relative phase shift between the (linear) polarization component aligned with the ordinary and the extraordinary axis [40]

$$\Delta\varphi = \frac{2\pi}{\lambda} d(|n_o - n_e|)\,, \tag{2.3}$$

where the thickness d can be set. Note that there is a dependence on the wavelength limiting the intended effect to a certain spectral range. Mostly, two kinds of wave plates are used: half-wave plates (HWP) and quarter-wave plates (QWP); introducing a phase shift of $\Delta\varphi = \pi$ and $\Delta\varphi = \frac{\pi}{2}$, respectively.

Rotating the wave plate in the plain perpendicular to the incident light corresponds to a change in basis and affects how the polarization amplitudes are split. The effect of HWP and QWP can be written as unitary operators [41]

$$U_{\text{HWP}}(\theta) = e^{i\frac{\pi}{2}} \begin{pmatrix} cos\,2\theta & sin\,2\theta \\ sin\,2\theta & -cos\,2\theta \end{pmatrix}\,, \tag{2.4}$$

$$U_{\text{QWP}}(\theta) = \frac{1}{\sqrt{2}} \begin{pmatrix} 1 + i\,cos\,2\theta & i\,sin\,2\theta \\ i\,sin\,2\theta & 1 - i\,cos\,2\theta \end{pmatrix}\,, \tag{2.5}$$

where the angle θ denotes the orientation of the optical axis with respect to horizontal polarization. For some common angles the effect of HWP and QWP on the standard bases states is listed in Tables A.1 and A.2 in the appendix.

Their property to alter the polarization state of a photon makes them suitable for implementing single-qubit unitaries. An arbitrary single-qubit unitary operation $U-$ a rotation on the Bloch sphere[2] –can be decomposed into a combination of three wave plates [41]

$$U = U_{\text{QWP}}(\gamma)\, U_{\text{HWP}}(\beta)\, U_{\text{QWP}}(\alpha)\,. \tag{2.6}$$

To transform any polarization state to H or V, two wave plates, a QWP and a HWP, are enough

$$U_{\to H/V} = U_{\text{HWP}}(\beta)\, U_{\text{QWP}}(\alpha)\,. \tag{2.7}$$

The QWP brings a potentially elliptical state to the x-z plane, where states with linear polarization are situated. For these states applying a HWP corresponds to a rotation about the y axis and can thus map any such state to H/V. Table 2.1 lists the required angles for some common polarizations.

---

[2] $U = e^{i\delta}\, R_{\vec{b}}(\omega)$, where $R_{\vec{b}}(\omega)$ is a rotation of ω about the axis defined by the unit Bloch vector $\vec{b}$. The global phase $e^{i\delta}$ is usually ignored. The remaining three free parameters are set by the wave plate angles α, β and γ.

Input →	QWP	HWP	→ *Output*
H/V	0°	0°	H/V
D/A	45°	22.5°	H/V
R/L	45°	45°	H/V

Table 2.1: *How to transform standard bases to the H/V basis using a* QWP *and a* HWP*. Note that* QWP *and* HWP *do not commute, so the angles are specific to the given order.*

Before a wave plate can be used the position of the optical axis needs to be determined (Figure 2.2).

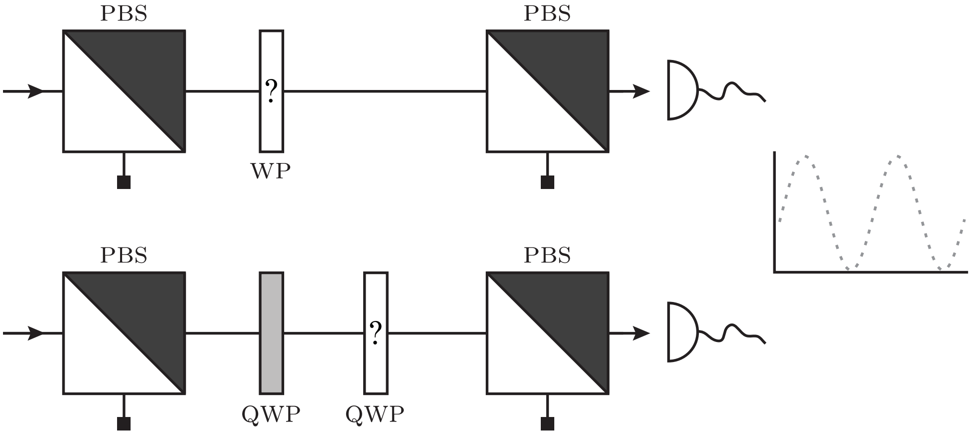

Figure 2.2: *Aligning a wave plate. Place an unknown wave plate between two polarizing beam splitters and monitor the intensity, while rotating it in the plain perpendicular to the incident light. For some angle the intensity reaches a minimum: (*HWP*) when the polarization is flipped from H to V; (*QWP*) the linear polarization is transformed to circular polarization. Refer to Tables A.1 and A.2 to determine the axis position from this information. Attention must be given that all* QWP*s are aligned to the same axis, ordinary or extraordinary. Use a reference* QWP*: two* QWP*s aligned to the same axis will act as an effective* HWP*, while compensating each other when not.*

2.3 Beamsplitters

A beam splitter (BS) is a probabilistic device mediating between two spacial input and output modes. It is characterized by its transmission (reflection) probability T (R). The most common configuration is a 50/50 beam splitter with $\frac{T}{R} = 1$.

Beam splitters can be designed to have different properties with respect to the polarization of the incident light, then called polarizing beam splitters (PBS). The usual setting is that a PBS transmits H- and reflects V-polarized light. By sandwiching a PBS between a set of wave plates it can be changed to operate in a basis other than the default H/V (Figure 2.3a). Moreover, it can be used to translate from a polarization encoded qubit to a path encoded qubit and vice versa (Figure 2.3b).

A subclass of polarizing beam splitters are polarization-dependent beam splitters (PDBS) that behave asymmetrically for H and V. PDBSs form a crucial component of the two-qubit gate presented in Chapter 4. The variant to be used there, transmits all H-polarized light, while a V-polarized photon passes through in one third and is reflected in the remaining two thirds of the cases.

Occasionally, both input modes of a beam splitter are used to produce a Hong-Ou-Mandel two-photon interferometer type effect [42]. For a pair of photons, originating from a SPDC source, one is fed into the BS from either side. When the paths are shifted towards equal lengths, a decrease in the coincidence count rates is observed. The counts drop to a minimum when the difference is within the coherence length of the photons.

It is tempting to conclusively picture this as the result of interference between two individual photons indistinguishable at the BS. It was however clarified [43] that not the indistinguishability of the single photons at the BS, but of the two-photon amplitudes describing the various alternatives leading to a coincident count at the detectors is decisive. In the BS scenario four such alternatives exist: two cases where the photons exit at the same port, one transmitted one reflected (t-r & r-t), and two cases where they split up (r-r & t-t). When the paths are of exactly the same length, the cases t-t and r-r are indistinguishable and happen to interfere destructively in correspondence with the observed coincidence count rates.

A slightly modified experiment can rule out the single-photon interpretation (Figure 2.4). A relative delay is introduced such that the photons no longer arrive at the same time at the beam splitter. This clearly eliminates the first interpretation. But when the delay is compensated afterwards, producing the same relative time difference at the detectors for both alternatives, t-t and r-r, which makes them indistinguishable again, the dip in coincidence count rates returns.

2.4 Mirrors, fibres and free space

It is a common situation that two distinct parts of a setup need to be connected. Usually, the experimenter wants the state of the quantum system to remain the same before and after the passage. In contrast to other quantum systems photons are mostly unaffected by the environment. However, there are certain pitfalls to be avoided.

Frequently, light travels in free space. Dust particles floating in the air can cause deformations in the (Gaussian) beam profile of high-intensity laser beams. To recover a clean Gaussian shape the following procedure can be employed:

1. Assuming the incident laser beam to be collimated. Use a convex lens to focus

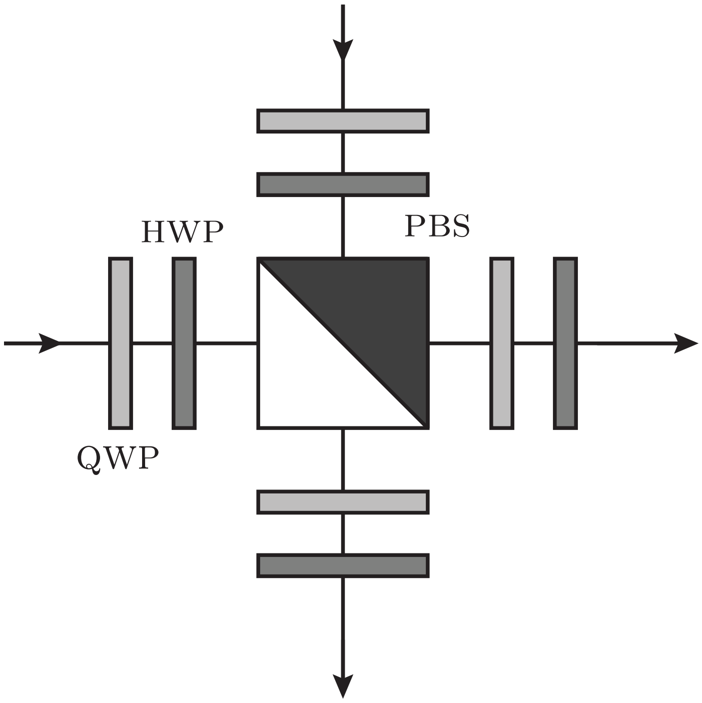

(a) *Polarizing beam splitters are usually manufactured to operate on H/V polarization. Using wave plates an arbitrary basis PBS can be emulated. Before the photons enter the PBS they pass through a* HWP *and* QWP *with angles set such that they transform from the desired operation basis to the H/V basis. The procedure is reversed at the output ports of the PBS.*

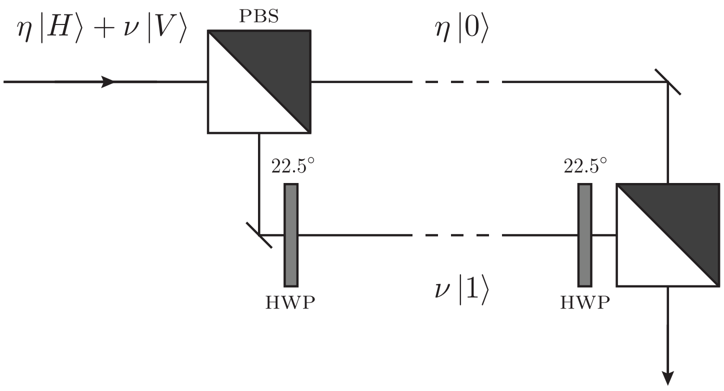

(b) *Converting between polarization encoding and path encoding of a photonic qubit. A PBS separates H and V components into distinct paths faithful to their respective amplitudes. To make them indistinguishable by the polarization degree of freedom a* HWP *at* 45° *transforms* $|V\rangle \leftrightarrow |H\rangle$*. Backtransformation is feasible by reversing the order of the components.*

Figure 2.3: *Some applications of wave plates and beam splitters.*

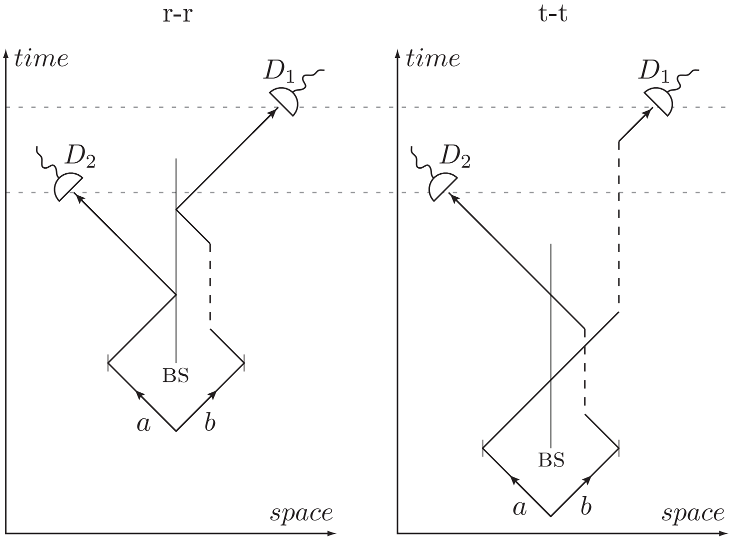

Figure 2.4: *Postponed compensation experiment [43]. One of two photons is delayed (indicated by the dashed line), so they no longer meet at the beam splitter. An additional delay for the t-t case assures that detector D_2 fires first in both situations. As the relative time difference stays constant r-r and t-t become indistinguishable. Accordingly, the dip in the coincidence count rates is observed, despite the single-photon interference interpretation no longer applicable.*

the beam and calculate the beam waist at the focal point.

2. The image at the focal point is the Fourier transform of the image at the object-side focal point [40]. Finer details, like deformations, require higher spatial frequencies to be resolved. The higher the frequency, the further off the corresponding amplitude lies from the centre of the Fourier image [44]. With a suitable iris the outer parts containing the frequency information of the deformations can be cut away.

3. Use another identical lens to undo the Fourier transform and collimate the beam again.

When the beam shape has become elliptical, e.g. after the up-conversion process in a LBO crystal [45], the sequence of two cylindrical lenses can be used to correct it back to a circular form. See [46] for instructions on how to select the ratio of their focal lengths.

To change the propagation direction of a laser beam mirrors are used. It is important to respect the mirror's angle of incident (AOI) specification. One discriminates between mirrors (AOI $= 0°$) and turning mirrors (AOI $= 45°$). When the polarization of photons is an issue a mirror is no longer a neutral element, but has the effect of a half-wave plate set to $0°$, hence it flips $D/A \rightarrow A/D$ and $R/L \rightarrow L/R$.

Whenever there is an unbalanced number of mirrors[3] in the setup this has to be compensated for, e.g. with a half-wave plate. Additionally, most mirrors have different reflection coefficients for H- and V-polarized light. This means that the amplitudes are treated unequally and a drift in the polarization is observed.

When light is coupled into an optical fibre, again its polarization state needs to be controlled. In an ideal fibre each polarization mode would propagate with identical velocity. Slight asymmetries in the fibre core cross-section and external stresses applied on the fibre such as bending alter the refractive index along the fibre. Differing velocities between the polarization modes in the fibre introduce a relative phase shift between them. This leads to a change in polarization.

The stress-induced birefringence of the fibre can also be used to compensate for these effects. In most cases the intermediate polarization state of the light in the fibre is unimportant as long as there is no effective change in the output state. Fibre polarization controllers (FPC) are used to intentionally apply stress on the fibre. To perform an arbitrary single-qubit operation the usual QWP-HWP-QWP combination of a free-space setting is replaced by three fibre coils inlaid in the FPC paddles. Coiling the fibre induces stress, producing birefringence inversely proportional to the square of the coils' diameters [47]. The number of turns specifies the wave plate's type. One turn corresponds to a QWP, two to a HWP. Adjusting the paddles rotates the fast axis of the fibre, which lies in the plane specified by the paddle.

To build a polarization conserving fibre path it is necessary to pinpoint both angles, θ and φ, that define a single-qubit state with respect to the Bloch sphere. A common choice is to fix $|H\rangle$ and $|D\rangle$. Obviously, one cannot align them simultaneously, so the procedure has to be carried out iteratively in general. Note that fixing the orthogonal states $|H\rangle$ and $|V\rangle$ is not sufficient, as this imposes no constraint on the azimuthal angle φ.

2.5 Single-photon detection

An important part in linear optics quantum computation falls to the detection system, as most implementations rely on a measurement-induced nonlinearity through postselection. What are the properties of a good detector?

- *Capability to detect single photons*
- *High detection efficiency*
- *Low dark count rates*
- *Fast recovery time*
- *Photon-number resolving*

---

[3] Note that this may also apply to the reflected arm of a beam splitter.

The experiments presented here use avalanche photodiodes (APD) that are fast and can resolve single photons, but cannot distinguish between one and many and have a rather low detection efficiency of about 40%. This is a serious downside as it further lowers the observed count rates, especially since one is usually interested in coincidence detections[4]. For a twofold-coincidence the detection probability degrades already to about 16% with these detectors. Many new developments in this field offer considerable improvements. An overview of current single-photon detection architectures is found in [48].

In general detectors do not distinguish between photons of different polarizations. This is, however, a common requirement in many applications, e.g. quantum state tomography (see Section 4.4.1). Figure 2.5 describes how to experimentally measure the polarization state of a photon in an arbitrary basis using wave plates, polarizing beam splitters and single photon detectors.

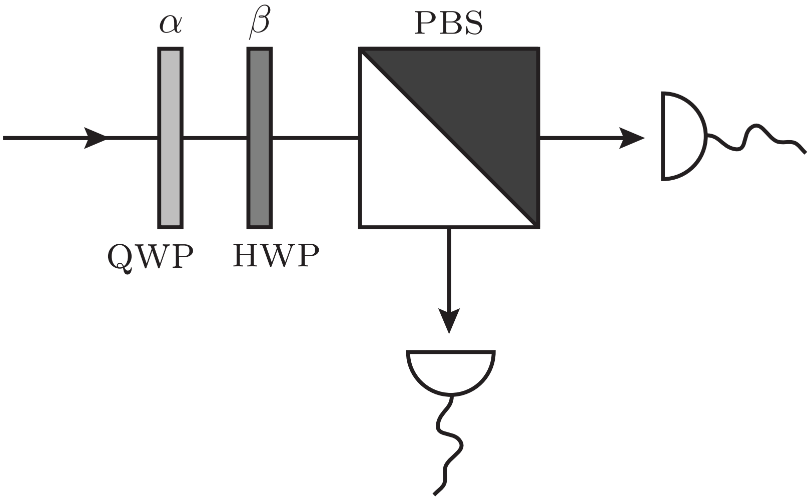

Figure 2.5: *Polarization analysis of light in an arbitrary basis follows a general procedure: The state of the incoming photon is considered to be decomposed with respect to the desired measurement basis. The basis vectors of this basis are then mapped to the H/V basis (vectors) by applying a* QWP *and a* HWP *with specific angle settings, α and β (cf. (2.7)). Next a PBS is used to separate H- and V-polarization. Finally, each output is fed into a single photon detector. A click at the detector for horizontally polarized photons reveals the photon to have carried the polarization determined by the chosen map. To measure in the D/A basis, for example, the map (wave plate setting) needs to transform $|D\rangle \rightarrow |H\rangle$ and $|A\rangle \rightarrow |V\rangle$. When the detector for $|H\rangle$ is triggered, one can deduce that the photon carried polarization $|D\rangle$.*

---

[4] A coincidence is the simultaneous detection of single photons at different detectors. To achieve nonzero count rates, a time window shorter than the gap between two successive pulses from the source is defined to characterize *simultaneous* events.

Chapter 3

Arbitrary single-qubit unitaries with wave plates

With photons single-qubit unitaries are generally considered the *easy* part. The main challenges come with the implementation of two-qubit gates (see Section 4). In principle this is true; applying single-qubit gates is a solved problem and can be accomplished by the use birefringent elements; typically wave plates. A few common single-qubit gates, along with the corresponding wave plate setting for their implementation, are listed in Table 3.1.

Single-qubit gate	Symbol	Wave plate setting
Identity	$\mathbb{1}$	$\text{QWP}(0) \cdot \text{HWP}(0) \cdot \text{QWP}(0)$
Pauli-X	X	$\text{HWP}(\frac{\pi}{4})$
Pauli-Y	Y	$\text{HWP}(\frac{\pi}{4}) \cdot \text{HWP}(0)$
Pauli-Z	Z	$\text{HWP}(0)$
Hadamard	H	$\text{HWP}(\frac{\pi}{8})$
X-rotation	$R_x(\theta)$	$\text{QWP}(\frac{\pi}{2}) \cdot \text{HWP}(-\frac{\theta}{4}) \cdot \text{QWP}(\frac{\pi}{2})$
Y-rotation	$R_y(\theta)$	$\text{QWP}(\frac{\pi}{2} + \frac{\theta}{2}) \cdot \text{HWP}(\frac{\theta}{4}) \cdot \text{QWP}(\frac{\pi}{2})$
Z-rotation	$R_z(\theta)$	$\text{QWP}(\frac{\pi}{4}) \cdot \text{HWP}(-\frac{\pi}{4} - \frac{\theta}{4}) \cdot \text{QWP}(\frac{\pi}{4})$

Table 3.1: *Single-qubit gates and how to experimentally realize them using wave plates. Note that any gate may also introduce a global phase. The angle θ specifies the rotation as observed on the Bloch sphere, while the arguments of* HWP *and* QWP *are the corresponding physical angle settings of the wave plates.*

There is, however, an easily overlooked aspect that needs to be considered. The operation of half and quarter-wave plate do not translate directly into rotations on the Bloch sphere. For general unitaries and with the interest of keeping the number of wave plates small[1] this property becomes manifest. For each particular single-qubit gate the angle settings of the wave plates need to be determined.

---

[1] It would be possible to use the known patterns of $R_x(\theta), R_y(\theta)$ and $R_z(\theta)$ to apply some arbitrary rotation, but this would lead to an inefficient use of wave plates.

3.1 Implementation with wave plates

Scenario I: One-way computational model

In the one-way computational model [18] an algorithm is defined by the shape of the entangled resource– a cluster state [21] –and a specific pattern of single-qubit measurements in directions along the x-y plane of the Bloch sphere. This includes, apart from the standard D/A and R/L, all states in between: $|\pm\varphi\rangle = \frac{1}{\sqrt{2}}(|H\rangle \pm e^{i\varphi}|V\rangle)$. In view of the polarization analysis setup described in Figure 2.5 a HWP and a QWP are needed

$$\text{HWP}(\beta)\ \text{QWP}(\alpha)\ |\pm\varphi\rangle \quad \longrightarrow \quad |H\rangle\,/\,|V\rangle\ . \tag{3.1}$$

To successfully perform this transformation we need the angles α and β. This is not as simple a task as it might seem at first sight. The wave plates perform nontrivial operations on the Bloch sphere. They introduce a global phase, which might have no effect in the experiment, but complicates the computational task of finding the correct angles. Additionally, the elements of the unitary matrices corresponding to the wave plates (cf. (2.4) and (2.5)) are trigonometric functions and thus α and β are given only implicitly. Nonetheless, it appears there is a simple relation for determining the angles in this case

$$\alpha = \frac{\pi}{4}\,, \tag{3.2}$$

$$\beta = \frac{\pi}{8} + \frac{\varphi}{4}\,. \tag{3.3}$$

Scenario II: Arbitrary measurement basis

Measuring in the x-y plane is only a subproblem of the more general problem to perform measurements in an arbitrary basis. Again, we have to determine the angles for the wave plates. Rewriting the problem in matrix form

$$\text{HWP}(\beta)\ \text{QWP}(\alpha) \begin{pmatrix} s_1' \\ s_2' \end{pmatrix} \equiv \begin{pmatrix} s_1 \\ s_2 \end{pmatrix} = |s\rangle \quad \longrightarrow \quad \begin{pmatrix} 1 \\ 0 \end{pmatrix} = |H\rangle \quad \text{or} \quad \begin{pmatrix} 0 \\ 1 \end{pmatrix} = |V\rangle \tag{3.4}$$

provides a helpful insight. One component of the column vector representation of both $|H\rangle$ and $|V\rangle$ is zero. If we manage to find a transformation such that one component of $|s\rangle$ is zero or at least smaller than a given threshold, we have found a solution regardless of the global phase factor. A simple numerical implementation of this strategy delivers correct results [49].

After a series of manipulations we also arrive at an analytical formula

$$\alpha = \arctan\left(\tan\theta\,\cos\frac{\varphi}{2}\right)\,, \tag{3.5}$$

$$\beta = \frac{1}{2}\,\frac{\arctan\left(\cos\theta\,\sin 2\alpha\,\cos 2\alpha + \sin\theta\,(\cos\varphi\,(\sin 2\alpha)^2 + \sin\varphi\,\cos 2\alpha\right)}{1 + \cos\theta\,(\cos 2\alpha)^2 + \sin\theta\,\sin 2\alpha\,(\cos 2\alpha\,\cos\varphi - \sin\varphi)}\,, \tag{3.6}$$

with Bloch sphere angles θ and φ defined by

$$\vec{s'}(\theta,\varphi) = \cos\frac{\theta}{2}\,|H\rangle + e^{i\varphi}\sin\frac{\theta}{2}\,|V\rangle\ . \tag{3.7}$$

Scenario III: Arbitrary to arbitrary single-qubit transformation

Apparently, the numerical procedure of Scenario II works only on the special cases–$|H\rangle$ or $|V\rangle$ –where the target state vector $|t\rangle$ has one zero component. What about transformations from some arbitrary to another arbitrary single-qubit state? From (2.6) we know that three wave plates should suffice

$$\text{QWP}(\gamma)\ \text{HWP}(\beta)\ \text{QWP}(\alpha)\begin{pmatrix} s'_1 \\ s'_2 \end{pmatrix} \equiv \begin{pmatrix} s_1 \\ s_2 \end{pmatrix} = |s\rangle \quad\longrightarrow\quad \begin{pmatrix} t_1 \\ t_2 \end{pmatrix} = |t\rangle\ . \tag{3.8}$$

Let us try to adopt the previous numerical approach to this problem. When the corresponding components, $s_1 = t_1$ and $s_2 = t_2$, are the equal, $|s\rangle$ and $|t\rangle$ represent the same state. Minimizing the sum of the absolute values of the differences

$$\underset{\alpha,\beta,\gamma}{min}\quad |s_1 - t_1| + |s_2 - t_2| \tag{3.9}$$

would give a valid solution. But the potential global phase factor complicates the situation. Suppose that $|t\rangle = |D\rangle = \frac{1}{\sqrt{2}}\binom{1}{1}$; a set of angles $\{\alpha,\beta,\gamma\}$, producing $|s\rangle = \frac{1}{\sqrt{2}}\binom{i}{i}$ is a correct solution. However, the minimization (3.9) returns

$$\left|\frac{i}{\sqrt{2}} - \frac{1}{\sqrt{2}}\right| + \left|\frac{i}{\sqrt{2}} - \frac{1}{\sqrt{2}}\right| = 2\,. \tag{3.10}$$

This solution is likely to be missed as many wrong angles lead to smaller values. To ensure a trustworthy result one would require (3.9) to be less than some threshold, certainly smaller than 2.

The problem is obviously due to a different global phase in $|s\rangle$ and $|t\rangle$. To cope with it we must bring them into a standardized form. One component of $|s\rangle$ can always be made a real number by multiplying it with $\kappa = e^{-arg(s_1)}$. This has the effect of setting a default phase factor of $+1$. Without loss of generality we can assume $|t\rangle$ also to have this form, as it is chosen by the experimenter. The adapted method

$$\underset{\alpha,\beta,\gamma}{min}\quad |\kappa s_1 - t_1| + |\kappa s_2 - t_2| \tag{3.11}$$

returns valid solutions for all but a single case. When $|t\rangle = |V\rangle$, the described phase problem persists[2]. Fortunately, this issue is easy to resolve, as we can fall back to the solution of scenario II whenever this happens.

---

[2] For $s_1 = 0$ the introduced global phase is hidden and κ is unable to bring $|s'\rangle$ to the standard form with phase $+1$.

The closed-form solution we found for measuring in an arbitrary basis suggests that one can also find a solution for this problem. From (3.6) we know how to use a QWP to transform a general state to a linear-polarization state. When we apply this technique from both ends, $|s'\rangle$ and $|t\rangle$, we receive two states located in the x-z plane of the Bloch sphere. The intermediate HWP can map two such states onto each other. Appendix B contains a *Mathematica*[3] implementation of the outlined strategy.

3.2 A demonstration

We have acquired the means to perform any single-qubit transformation with just three wave plates. For each case, the initially unknown angles, α, β and γ, can be determined.

This calls for a demonstration. Consider two randomly chosen states

$$|s'\rangle = \begin{pmatrix} 0.979 \\ -0.142 - 0.148i \end{pmatrix} \qquad \xrightarrow{\alpha,\beta,\gamma} \qquad |t\rangle = \begin{pmatrix} 0.892 \\ 0.404 - 0.202i \end{pmatrix},$$

scattered around the Bloch sphere; see Figure 3.1a and 3.1d. We find

$$\alpha = 90.8036, \quad \beta = 18.2966 \quad \text{and} \quad \gamma = 18.8240\,.$$

It is instructive to visualize each step of the transformation individually. Figure 3.1 shows the intermediate Bloch vector after the application of each wave plate.

To confirm the correctness of the angles, the experimentally obtained density matrices of the input state, $|s'\rangle$, and the final state are compared in Figure 3.2 and 3.3. Note the nonvanishing imaginary parts also in the theoretical values (cones). The state fidelities F_S between experimental and theoretical data[4]

$$|s'\rangle : F_S = 99.3\%, [98.8; 99.7] \quad \text{and} \quad |t\rangle : F_S = 99.6\%, [98.0; 99.9]$$

express a high level of agreement.

---

[3] http://www.wolfram.com/mathematica/

[4] The fidelity is restricted to the interval $[0; 1]$. Close to the boundaries its distribution is insufficiently described by a Gaussian fit. Instead, a bounded Johnson distribution [50] was used. A confidence interval containing approximately 68% of the values is given in brackets.

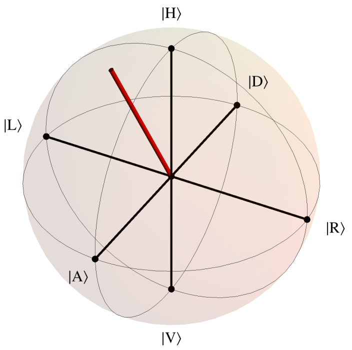

(a) *Input state:* $|s'\rangle \rightarrow$

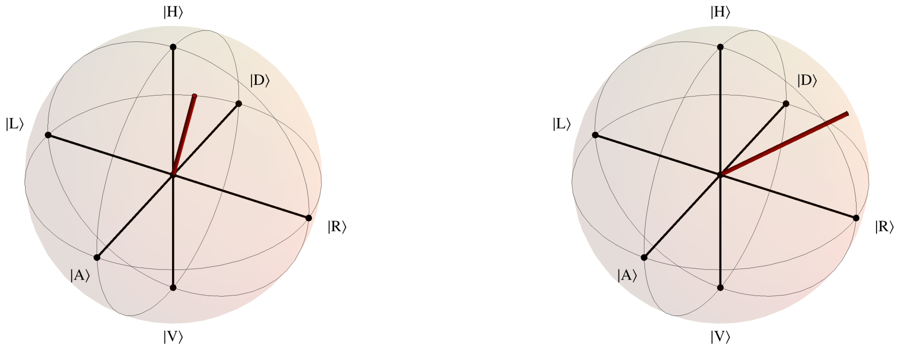

(b) *Intermediate state 1: after* QWP$(\alpha) \rightarrow$ **(c)** *Intermediate state 2: after* HWP$(\beta) \rightarrow$

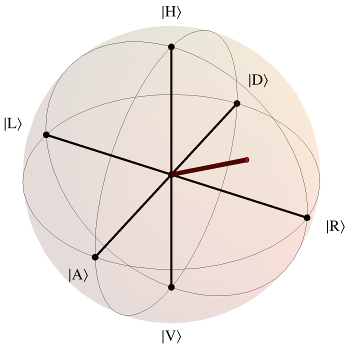

(d) *Final state*

Figure 3.1: *The transformation process visualized on the Bloch sphere. For each step the resulting Bloch vector is shown.*

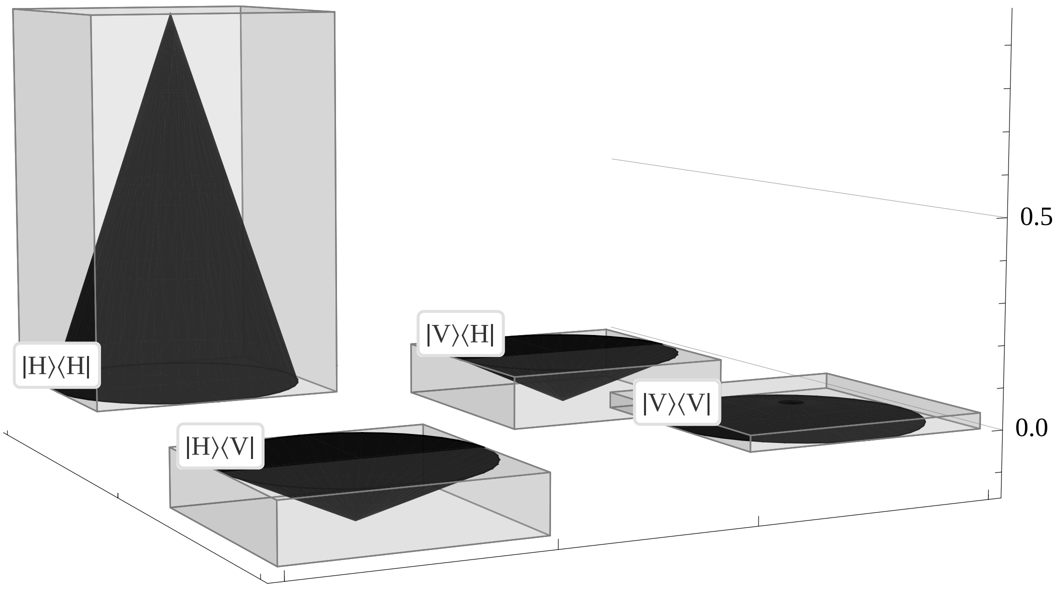

(a) *Input state density matrix - Real*

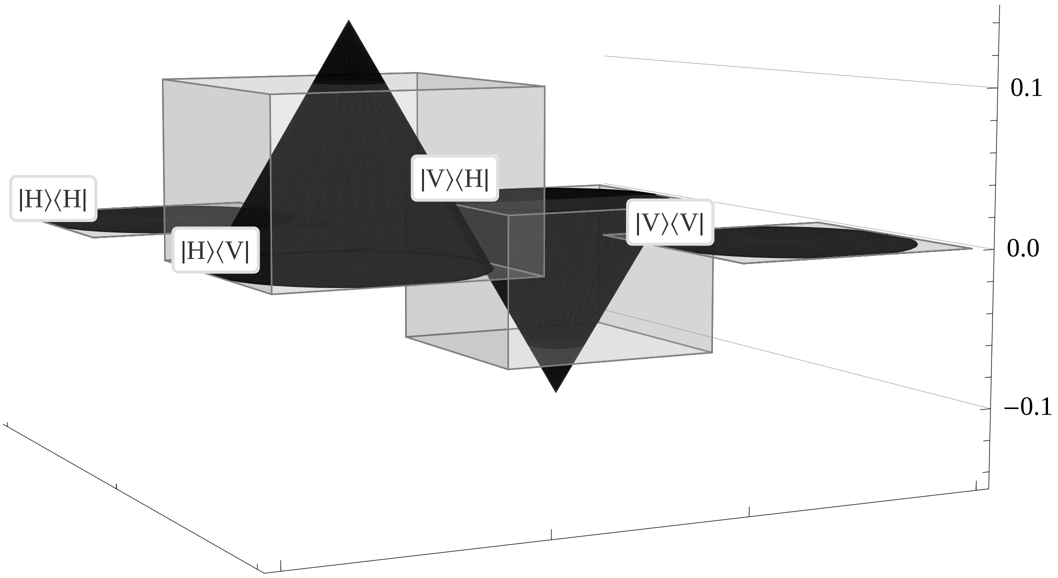

(b) *Input state density matrix - Imaginary*

Figure 3.2: *Theoretical (cones) and experimental (bars) density matrices of input state* $|s'\rangle$.

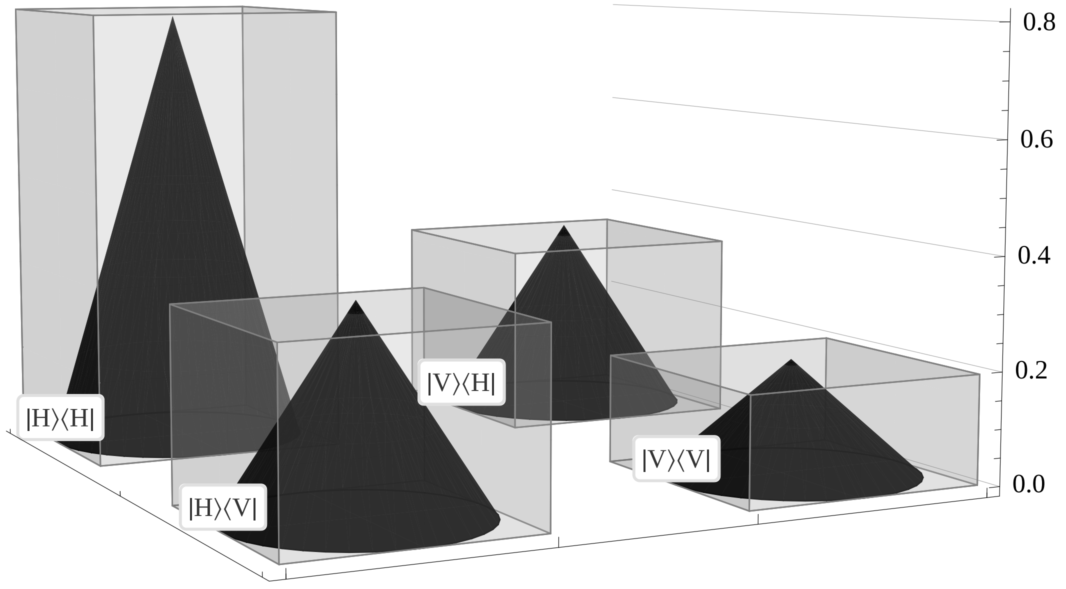

(a) *Final state density matrix - Real*

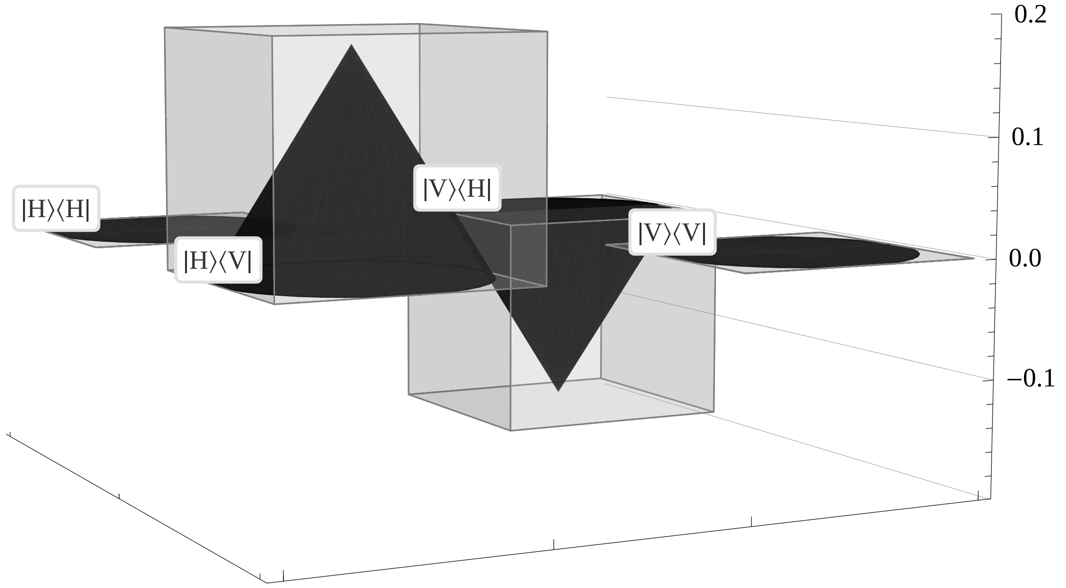

(b) *Final state density matrix - Imaginary*

Figure 3.3: *Theoretical (cones) and experimental (bars) density matrices of the state after applying* $U_{qhq} = \mathrm{QWP}(\gamma)\,\mathrm{HWP}(\beta)\,\mathrm{QWP}(\alpha)$ *to* $|s'\rangle$*. The angles* α*,* β *and* γ *were determined by the described method.*

Chapter 4

Experimental realization of a Controlled-NOT gate

Inspired by its classical counterpart a circuit model for quantum computation was developed [19, 20]. In this scheme an algorithm is implemented via unitary transformation of a quantum state representing the input register. In analogy to a classical computer– e.g. NAND –a set of operations (gates) is sufficient to construct a universal quantum computer capable of implementing generic quantum algorithms. As explained in more detail in [51] the set of all single-qubit unitaries together with a two-qubit gate[1]– e.g. CNOT –is universal for quantum computation. In brief; a quantum process on an input register of N qubits may be decomposed into smaller entities, because the corresponding multi-qubit unitary can be written as a product of operators that each act non-trivially only on a two-dimensional subspace. Single-qubit and CNOT gates, on the other hand, suffice to implement any such two-level unitary operation.

4.1 Properties of the CNOT gate

A controlled two-qubit operation assigns different roles to either qubit. One qubit (usually the first) is referred to as control qubit. Its state– a superposition of $|H\rangle : |0\rangle :$ FALSE and $|V\rangle : |1\rangle :$ TRUE –controls the operation applied to the other qubit, the target qubit. Apart from the already mentioned CNOT, we look at another controlled gate called[2] CSIGN. Their operation can be written as 4×4 unitary matrices

---

[1] Single qubit unitaries alone are not enough because some sort of interaction is needed to create entanglement between qubits. Interestingly the mere presence of entanglement is not enough to gain the exponential speedup of some quantum algorithms either. As can be inferred from the Gottesman-Knill theorem [52] it is necessary to include gates outside the Clifford group for an algorithm not to be efficiently simulable on a classical computer, i.e. in the stabilizer formalism [53].

[2] sometimes CPHASE

$$\text{CSIGN} = \begin{pmatrix} 1 & 0 & 0 & 0 \\ 0 & 1 & 0 & 0 \\ 0 & 0 & 1 & 0 \\ 0 & 0 & 0 & -1 \end{pmatrix} \tag{4.1}$$

$$\text{CNOT} = \begin{pmatrix} 1 & 0 & 0 & 0 \\ 0 & 1 & 0 & 0 \\ 0 & 0 & 0 & 1 \\ 0 & 0 & 1 & 0 \end{pmatrix} \tag{4.2}$$

or visualized in BraKet notation:

$$\begin{aligned} |\psi\rangle &= c_{HH}\,|H_1H_2\rangle \,+\, c_{HV}\,|H_1V_2\rangle \,+\, c_{VH}\,|V_1H_2\rangle \,+\, c_{VV}\,|V_1V_2\rangle \\ \text{CSIGN}\,|\psi\rangle &= c_{HH}\,|H_1H_2\rangle \,+\, c_{HV}\,|H_1V_2\rangle \,+\, c_{VH}\,|V_1H_2\rangle \,-\, c_{VV}\,|V_1V_2\rangle \end{aligned} \tag{4.3}$$

The CSIGN gate inflicts a sign flip on the amplitude c_{VV} and acts as an identity operation on the other components.

$$\begin{aligned} |\psi\rangle &= c_{HH}\,|H_1H_2\rangle \,+\, c_{HV}\,|H_1V_2\rangle \,+\, c_{VH}\,|V_1H_2\rangle \,+\, c_{VV}\,|V_1V_2\rangle \\ \text{CNOT}\,|\psi\rangle &= c_{HH}\,|H_1H_2\rangle \,+\, c_{HV}\,|H_1V_2\rangle \,+\, c_{VV}\,|V_1H_2\rangle \,+\, c_{VH}\,|V_1V_2\rangle \end{aligned} \tag{4.4}$$

The CNOT gate interchanges the amplitudes c_{VH} and c_{VV}, while leaving c_{HH} and c_{HV} in place.

A different naming convention refers to CSIGN and CNOT by CZ and CX, respectively, as they apply controlled Pauli Z and X operations on the target qubit. This almost immediately lets us understand the identity relation established by local Hadamard gates[3]

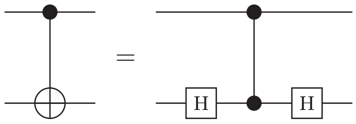

where the symbol on the left hand side corresponds to a CNOT in the circuit representation.

With photons any experimental implementation of one of them, is equally suitable to obtain the other. Transformation is a simple matter of adding a pair of wave plates.

4.1.1 Implementation scheme

A compact scheme for a CSIGN gate has been formulated in [54, 55, 56]. Section 5.2 compares several existing architectures and explains the advantages of this choice. The working principle of the gate unfolds by looking at the properties of a

---

[3] The Hadamard gate H = $\frac{1}{\sqrt{2}}$(X + Z) transforms between the H/V and D/A basis.

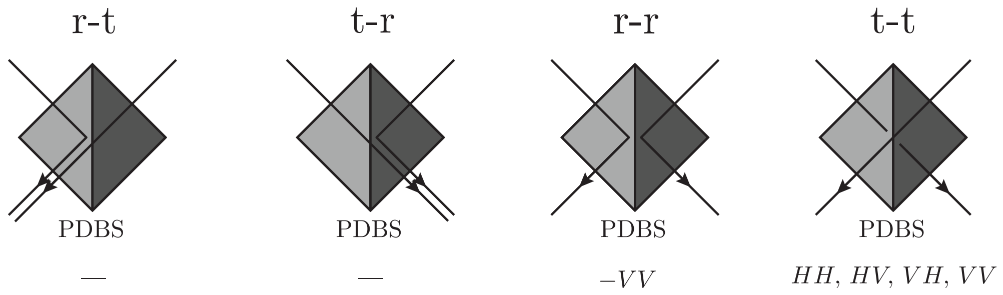

Figure 4.1: *Basic idea for the implementation of a* CSIGN *gate. Two photons entering a PDBS can exhibit four possible exit configurations. Postselecting for coincidence detections from both arms hides the spurious r-t and t-r cases. Below each scenario the possible coincidences are listed. As reflected photons pick up a phase factor, the VV term from r-r and t-t have opposite signs.*

polarization-dependent beam splitter (Figure 4.1). When a pair of photons, one at each input port, is subjected to a PDBS four possible scenarios occur:

r-t : The first photon is *reflected* and the second is *transmitted.*

t-r : The first photon is *transmitted* and the second is *reflected.*

r-r : Both photons are *reflected.*

t-t : Both photons are *transmitted.*

A few important observations can be made. Firstly, the cases r-t and t-r lead to a different detection pattern than r-r and t-t. Assuming that both output ports are fed into separate detectors, the former cases will never trigger a simultaneous detection as both photons exit through the same output port. For the latter, the situation is reversed, it will always lead to a coincident detection.

Secondly, due to the asymmetric behaviour of a PDBS– H-polarized photons are transmitted, while V-polarized photons have a certain chance of being reflected –the r-r case can only occur when both photons have a nonzero V-polarization amplitude. Additionally, the reflected photons pick up a phase shift. This selectively applies a minus sign to the $|VV\rangle$ term of the corresponding two-photon state, as it is expected from a CSIGN gate.

A VV coincidence without the phase change can, however, also happen in the course of a t-t event. When both cases– r-r and t-t –interfere the effective amplitude can be tuned by setting the V-polarization transmission probability of the (main) PDBS. The r-t and t-r events do not contribute to coincidence detections.

Another aspect that we will have to consider is that due to the interference the amplitudes of $|HH\rangle$, $|HV\rangle$, $|VH\rangle$ and $|VV\rangle$ are different. To faithfully implement a CSIGN operation they have to stay equal. Accordingly, we must use some component that can selectively attenuate the amplitudes. This can be done by another two (attenuation) PDBS placed in each arm of the setup.

4.1.2 Optimal components

Starting from a general two-qubit state $|\psi\rangle = c_{HH}\,|H_1H_2\rangle + c_{HV}\,|H_1V_2\rangle + c_{VH}\,|V_1H_2\rangle + c_{VV}\,|V_1V_2\rangle$, where the index suggests that the photons are in two separate modes, 1 and 2, a first PDBS (main) has the following effect

$$\begin{aligned}
|H_1\rangle &\longrightarrow \tau_H\,|H_1\rangle \;+\; i\,\kappa_H\,|H_2\rangle\\
|H_2\rangle &\longrightarrow \tau_H\,|H_2\rangle \;+\; i\,\kappa_H\,|H_1\rangle\\
|V_1\rangle &\longrightarrow \tau_V\,|V_1\rangle \;+\; i\,\kappa_V\,|V_2\rangle\\
|V_2\rangle &\longrightarrow \tau_V\,|V_2\rangle \;+\; i\,\kappa_V\,|V_1\rangle
\end{aligned}$$

$$\tau_X \equiv \sqrt{T_X}, \quad \kappa_X \equiv \sqrt{R_X} \quad \text{with} \quad X = \{H, V\}$$

where T_X/R_X is the corresponding transmission/reflection probability for X-polarized light. Characteristic to a measurement-induced nonlinearity is that we choose to only look at coincidence detections, i.e. when there is a simultaneous click at both the control and the target arm[4]. With any term containing two identical indices already sifted out, the calculation yields[5]

$$\begin{aligned}
|\psi'\rangle = (c_{HH}\,\tau_H\tau_H - c_{HH}\,\kappa_H\kappa_H) &\quad |H_1H_2\rangle\\
+(c_{HV}\,\tau_H\tau_V - c_{VH}\,\kappa_H\kappa_V) &\quad |H_1V_2\rangle\\
+(c_{VH}\,\tau_H\tau_V - c_{HV}\,\kappa_H\kappa_V) &\quad |V_1H_2\rangle\\
+(c_{VV}\,\tau_V\tau_V - c_{VV}\,\kappa_V\kappa_V) &\quad |V_1V_2\rangle
\end{aligned} \tag{4.5}$$

This is of course only possible as soon as no further element in the setup can transfer a photon from one arm to the other.

Each arm is then subjected to another PDBS (attenuator), of which the reflected port is committed to a beam dump. Whenever one photon on either side suffers this fate no coincidence can occur and the corresponding terms can be left out. In general the transmission/reflection amplitudes of these PDBS can be different from the first, hence we prime them

$$\begin{aligned}
|\psi''\rangle = (c_{HH}\,\tau_H\tau_H\tau'_H\tau'_H - c_{HH}\,\kappa_H\kappa_H\tau'_H\tau'_H) &\quad |H_1H_2\rangle\\
+(c_{HV}\,\tau_H\tau_V\tau'_H\tau'_V - c_{VH}\,\kappa_H\kappa_V\tau'_H\tau'_V) &\quad |H_1V_2\rangle\\
+(c_{VH}\,\tau_H\tau_V\tau'_H\tau'_V - c_{HV}\,\kappa_H\kappa_V\tau'_H\tau'_V) &\quad |V_1H_2\rangle\\
+(c_{VV}\,\tau_V\tau_V\tau'_V\tau'_V - c_{VV}\,\kappa_V\kappa_V\tau'_V\tau'_V) &\quad |V_1V_2\rangle\,.
\end{aligned} \tag{4.6}$$

---

[4] When a polarization-aware detector setting (cf. Figure 2.5) is used, this corresponds to the situation when one and only one detector of each arm is firing.

[5] As was mentioned beforehand, the two cases r-r and t-t must interfere for the scheme to work.

As can be seen from (4.3) a CSIGN scales (the modulus of) all amplitudes equally for any c_{HH}, c_{HV}, c_{VH} and c_{VV}. The only nontrivial solutions require either $\kappa_V = 0$ or $\kappa_H = 0$. Choosing the latter the transmission/reflection amplitudes must fulfil the following condition

$$\tau_H \tau_H \tau'_H \tau'_H \overset{!}{=} \tau_H \tau_V \tau'_H \tau'_V \overset{!}{=} -(\tau_V \tau_V \tau'_V \tau'_V - \kappa_V \kappa_V \tau'_V \tau'_V) \tag{4.7}$$

apart from the restrictions due to the transmission/reflection probabilities: $0 < T_X, R_X \leq 1$ and $T_X + R_X \leq 1$. Note the additional minus sign in front of the last term forming the CSIGN operation. $\kappa_H = 0$ already implies $\tau_H = 1$, leaving $0 < \tau'_H \leq \frac{1}{\sqrt{3}}$, $\tau_V = \frac{1}{\sqrt{3}}$ and $\tau'_V = \sqrt{3}\tau'_H$.

What value should we choose for τ'_H? To answer this question we must first determine what an optimal value should do. Scaling the amplitudes in (4.3) by a constant factor f means that only a fraction of the photons is observed at the control and target outputs. This reduces the probability of a successful gate operation by the square of that factor

$$\rho \overset{\text{CSIGN}}{\longrightarrow} (f \times \text{CSIGN})\, \rho \, (f \times \text{CSIGN})^\dagger = f^2 \times (\text{CSIGN}\, \rho \, \text{CSIGN}^\dagger), \tag{4.8}$$

where ρ is the density matrix of some two-qubit state. The optimal value would therefore be $f = 1$. From (4.7) we see that $f(\tau'_H) = \tau'^2_H$, therefore $\tau'_H = \frac{1}{\sqrt{3}} \Rightarrow f = \frac{1}{3}$ is our best option. Accordingly, the setup is expected to apply a successful CSGIN operation in one ninth of the cases ($= 11.\bar{1}\%$).

This is another consequence of the measurement-induced nonlinearity scheme. In most cases the desired operation can only be realized with a certain chance; the gate becomes probabilistic. Fortunately, there is a clear distinction between correct and incorrect runs. A successful gate operation is unambiguously indicated by a coincidence detection.

In Table 4.1 the transmission and reflection probabilities corresponding to $f = \frac{1}{3}$ are given,

$$|\psi''\rangle_{f=\frac{1}{3}} = \frac{1}{3}\ |H_1 H_2\rangle + \frac{1}{3}\ |H_1 V_2\rangle + \frac{1}{3}\ |V_1 H_2\rangle - \frac{1}{3}\ |V_1 V_2\rangle\,. \tag{4.9}$$

4.1.3 Modelling imperfect components

Now that we know what properties ideal components should have, it is advisable to study the impact of deviations from these values on the gate. Let us therefore review the gate's performance under the influence of imperfect components.

Considering the transmission probability T_V of the main PDBS as a free parameter affects the operation of CSIGN on an arbitrary input state ρ in the following way (cf. (4.6))

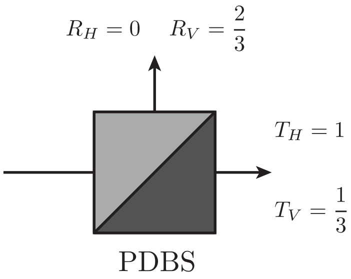

Main PDBS:	
$T_H = 100\%$	$T_V = 33.\dot{3}\%$
$R_H = 0\%$	$R_V = 66.\dot{6}\%$
Attenuation PDBS:	
$T'_H = 33.\dot{3}\%$	$T'_V = 100\%$
$R'_H = 66.\dot{6}\%$	$R'_V = 0\%$

Table 4.1: *Optimal values of transmission and reflection probabilities for the PDBS to be used in the* CSIGN *setup.*

$$\rho \longrightarrow W\rho W^\dagger, \quad \text{where} \quad W(T_V) = \begin{pmatrix} \frac{1}{3} & 0 & 0 & 0 \\ 0 & \sqrt{\frac{T_V}{3}} & 0 & 0 \\ 0 & 0 & \sqrt{\frac{T_V}{3}} & 0 \\ 0 & 0 & 0 & 2T_V - 1 \end{pmatrix}. \tag{4.10}$$

This model is equally valid for a CNOT gate implemented by $(\mathbb{1} \otimes H) \cdot \text{CSIGN} \cdot (\mathbb{1} \otimes H)$, where the single-qubit Hadamard is assumed to be perfect.

The process fidelity F_p is a suitable benchmark parameter[6] to quantify the performance of a gate. In Figure 4.2 its dependence on the transmission probability of the main PDBS is shown. The simulation verifies the ideal value of $T_V = \frac{1}{3}$ we derived earlier. Apart from that it prognoses a moderate degradation when the ratio deviates from that value.

Similar considerations can be given to the influence of the attenuating PDBS. Here the roles of H- and V-polarized light are interchanged. The effect of a variable

---

[6] for a definition see (4.30)

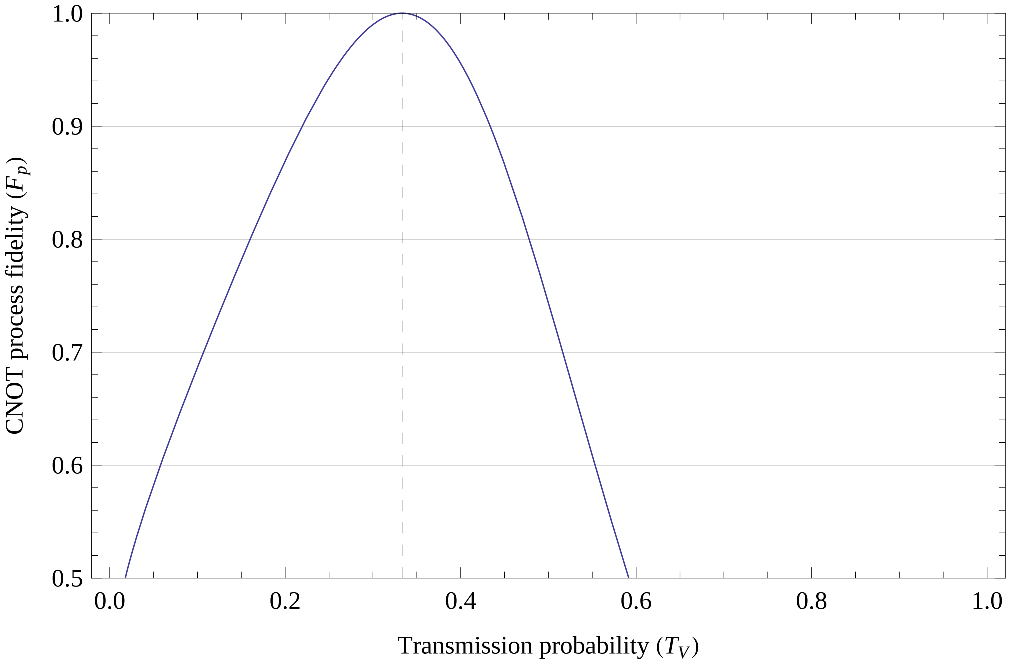

Figure 4.2: *Simulating the* CNOT *process fidelity for a varying transmission probability* T_V *of the main PDBS.*

transmission probability T'_H is modelled by

$$\rho \longrightarrow W' \rho W'^{\dagger}, \quad \text{where} \quad W'(T'_H) = \begin{pmatrix} T'_H & 0 & 0 & 0 \\ 0 & \sqrt{\frac{T'_H}{3}} & 0 & 0 \\ 0 & 0 & \sqrt{\frac{T'_H}{3}} & 0 \\ 0 & 0 & 0 & -\frac{1}{3} \end{pmatrix}. \tag{4.11}$$

The required precision of these components are less demanding (see Figure 4.3). In particular a transmission probability greater than $\frac{1}{3}$ only gradually lowers the gate's performance.

In Figure 4.4 imperfect transmission probabilities for either PDBS are considered (axes). A lighter shading corresponds to a higher CNOT process fidelity. The contour lines represent a lower bound for F_p inside the enclosed region.

4.1.4 Modelling imperfect interference

Until now we tacitly assumed that interference is perfect. In an experimental situation partial mode overlap and distinguishability between the possibilities t-t and r-r is expected to cause undesired behaviour. Let us swap the viewpoint and take this aspect into account. Both cases– t-t and r-r –can be described individually

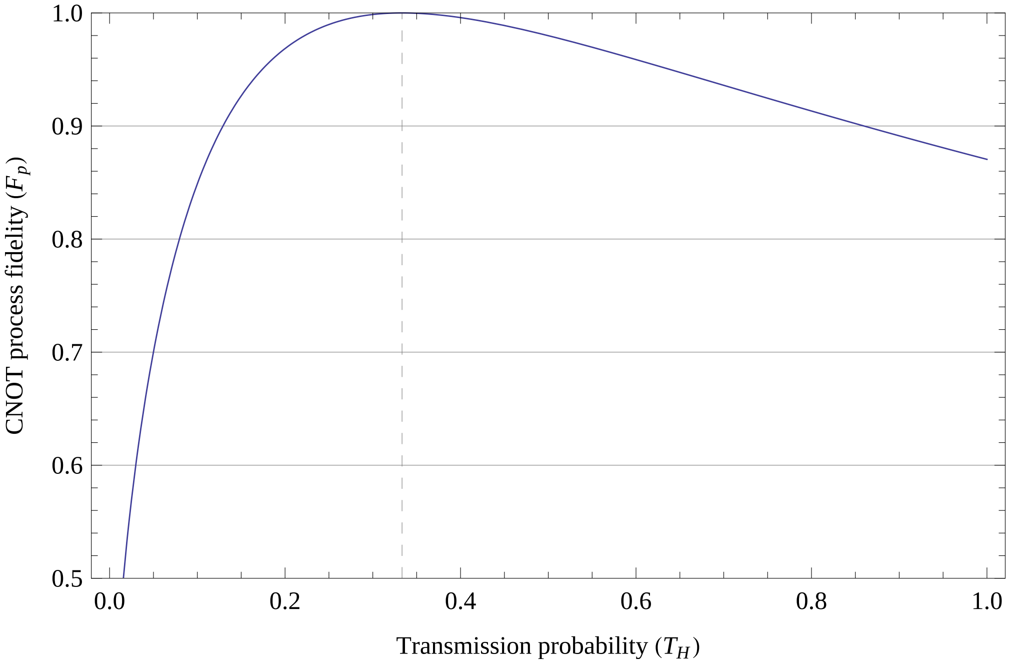

Figure 4.3: *Simulating the CNOT process fidelity for a varying transmission probability T_H of the attenuation PDBS.*

by [55, 37, 57]

$$M_{tt} = \begin{pmatrix} \frac{1}{3} & 0 & 0 & 0 \\ 0 & \frac{1}{3} & 0 & 0 \\ 0 & 0 & \frac{1}{3} & 0 \\ 0 & 0 & 0 & \frac{1}{3} \end{pmatrix} \tag{4.12}$$

$$M_{rr} = \begin{pmatrix} 0 & 0 & 0 & 0 \\ 0 & 0 & 0 & 0 \\ 0 & 0 & 0 & 0 \\ 0 & 0 & 0 & -\frac{2}{3} \end{pmatrix} \tag{4.13}$$

In the domain of interference both matrices add up, i.e. interaction happens on amplitude level and the correct CSIGN operation is performed. Distinguishability leads to an incoherent mixture of M_{tt} and M_{rr}

$$\begin{aligned} \rho \longrightarrow M\,\rho\,M^\dagger = \quad & Q\,(M_{tt} + M_{rr})\,\rho\,(M_{tt} + M_{rr})^\dagger \\ & + (1-Q)\,(M_{tt}\,\rho\,M_{tt}^\dagger + M_{rr}\,\rho\,M_{rr}^\dagger)\,. \end{aligned} \tag{4.14}$$

The probability of each event is determined by Q, a factor that quantifies the amount of distinguishability introduced in Section 4.2.2. We immediately make two observations: (i) the terms $|HH\rangle\,, |HV\rangle$ and $|VH\rangle$ are not affected by Q. The gate will continue to operate as an identity gate. Here the photons are always transmitted

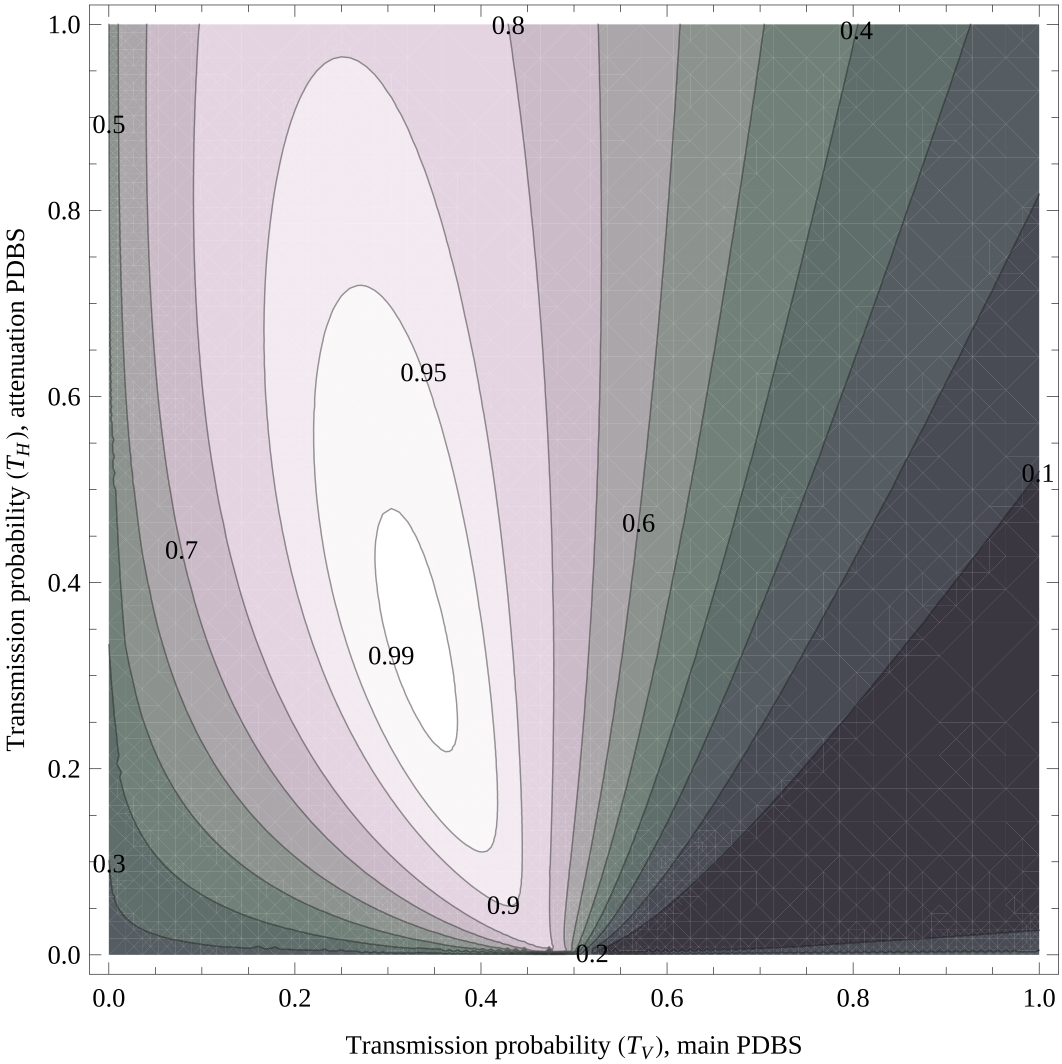

Figure 4.4: *A simulation of the effect of imperfect PDBS on the* CNOT *process fidelity. The transmission probability,* T_V*, of the main PDBS and,* T_H*, of the attenuation PDBS are varied simultaneously. The labels denote the process fidelity in the enclosed region for a given* T_V *and* T_H*. A lighter shading corresponds to a better process fidelity. For either parameter the ideal value is* $\frac{1}{3}$*.*

and interference plays no role. (ii) For $|VV\rangle$ the situation is quite different: When $Q = 0$ there is a chance of $|\frac{1}{3}|^2 + |-\frac{2}{3}|^2 = \frac{5}{9}$ for a VV-coincidence, while for $Q = 1$ it is reduced to $|\frac{1}{3} - \frac{2}{3}|^2 = \frac{1}{9}$. Hence, in contrast to the ideal CSIGN, in this model pure states will in general be mapped to mixed states. Regarding the previous section, Figure 4.5 simulates the effect of Q on the process fidelity F_P.

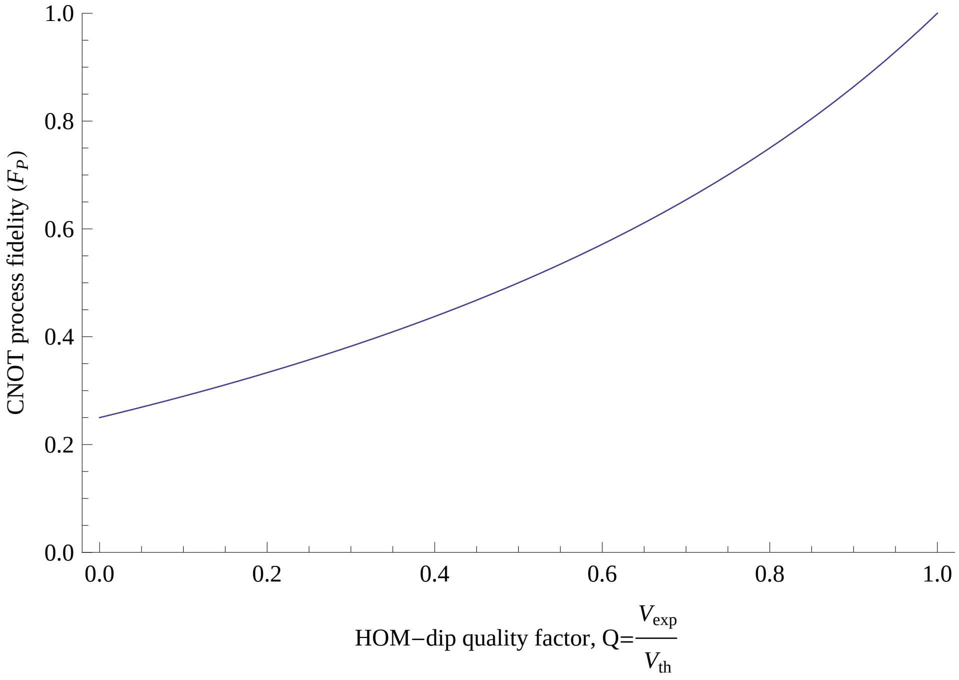

Figure 4.5: *A simulation of the* CNOT *process fidelity based on the model (4.14) for partial interference.*

4.2 Experimental realization

A comprehensive description of how to build this type of gate is found in [57]. Some additional comments specific to our implementation are given in the following section.

4.2.1 Construction notes

Coupler stability

Approximately place two input couplers and four output couplers for polarization analysis on a breadboard as depicted in Figure 4.6. During the initial steps of alignment a diode laser with the correct wavelength can be used. At this moment it is a good idea to shine the laser through each of the six couplers and focus the beam at a wall a few metres away. By that the beam is equally collimated among

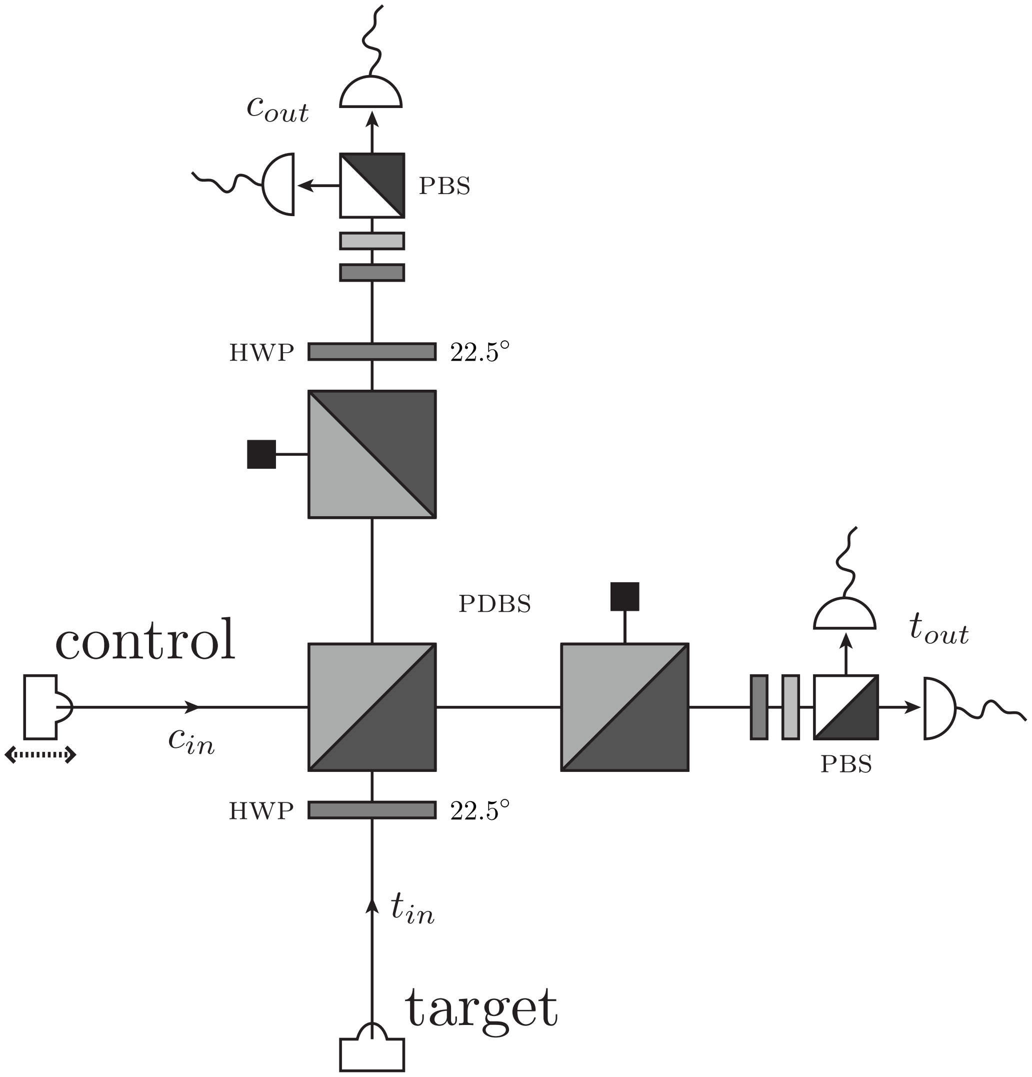
c_{out}
PBS
HWP
22.5°
PDBS
control
c_{in}
t_{out}
PBS
HWP
22.5°
t_{in}
target

Figure 4.6: *A detailed sketch of the PDBS-based* CNOT *gate. One of the input couplers is attached to a motorized translation stage for adjusting the path length. Half-wave plates at* 22.5° *apply a Hadamard gate on the target qubit. This changes the gate operation from* CSIGN *to* CNOT*. Both input beams are superimposed at the main PDBS. The reflected modes of a second pair of PDBS (attenuation) are committed to beam dumps. Four detectors are used for efficient polarization measurements.*

the couplers, which considerably eases coupling and later on will lead to good mode overlap.

One of the input couplers is mounted on a motorized stage providing the freedom to translate along the beam direction. The intensity should stay as constant as possible, while moving the motorized stage from one end to the other (Figure 4.7). Once this is achieved the motorized input coupler should not be moved anymore.

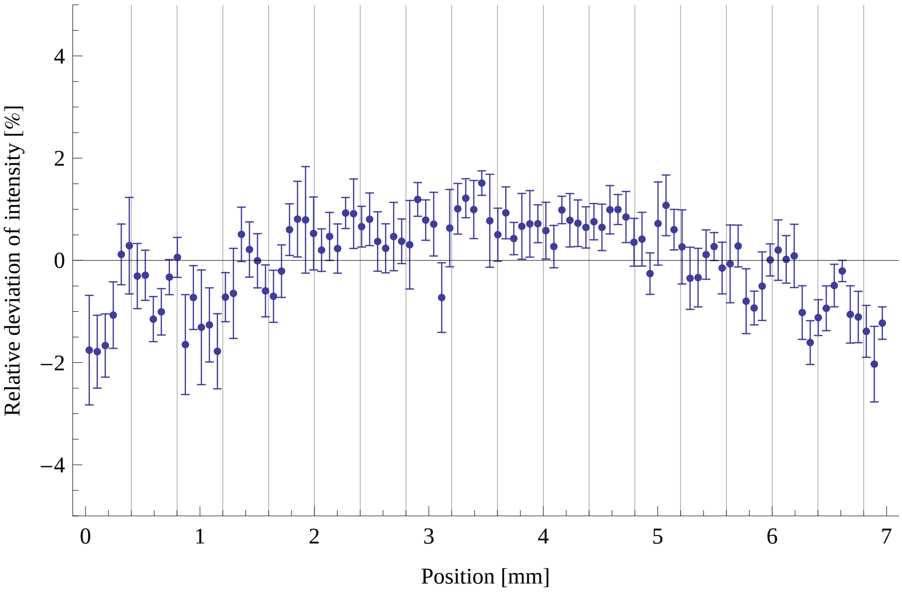

Figure 4.7: *Moving the motorized coupler from on end to the other. The intensity should not change considerably over this period. The vertical grid lines mark bins of 0.4mm. This is approximately the spacial extension of the HOM-dip as can be seen in Figure 4.9.*

Placing the main PDBS

Now it is time to insert the main polarization-dependent beam splitter (see Table 4.1). Both input beams will be superimposed at its position. We can use it to align the remaining couplers. First send the laser beam through the motorized coupler and optimize each output coupler. Then use the second input coupler. It is important to remember that the output coupler cannot be moved, as this would destroy the coupling with the first coupler. Therefore only adjust the second input coupler to increase coupling. If necessary repeat both steps iteratively. Hereafter the transmitted part of one and the reflected part of the other input beam should be overlapping.

To assure the correct reflection/transmission probability ratio of the PDBS ($\frac{R_V}{T_V} = 2$) make sure the laser beam is vertically polarized and check the output intensities of each side. If the PDBS does not show the optimal ratio by default it can be tuned by slightly rotating it about the z axis [57]. Keep in mind that this destroys the orthogonal placement of couplers. Switch to the second input coupler; the PDBS must have the correct splitting ratio for both input couplers simultaneously.

Placing the attenuation PDBS

Two more PDBS, one in each arm, are used to equalize the amplitudes of H- and V-polarized light. Therefore the roles of H and V must be interchanged, either by prepending a HWP set to 45° or, alternatively, rotating the whole PDBS by 90°. Obviously, the ratio of the attenuation PDBS cannot be set directly. To align them send in D-polarized light and adjust their position such that the combination of main and attenuation PDBS leaves D-polarized light unchanged [57].

Single-photon source

The laser diode must now be exchanged with a single photon source as described in Section 2.1. Usually, it is necessary to overhaul the coupling at this point. If not already done so, any additional elements that will be required in the final setup should be added now. In particular you would not want to put in any components that cause a phase shift afterwards.

Finding the Hong-Ou-Mandel dip

The functioning of the gate is based on a second-order interference between the cases of t-t, both photons transmitted, and r-r, both photons reflected. The indistinguishability of these two alternatives can be set by monitoring the VV-coincidence count rate. While there is no interference the chance of getting a VV-coincidence is $\frac{5}{9}$. Translating the motorized input coupler changes the relative phase difference between both inputs. Once the r-r and t-t case start interfering a decrease in the VV counting rate is observed (see Figure 4.9), reaching a minimum for perfect indistinguishability. At the optimal position VV-coincidences occur only with a $\frac{1}{9}$ chance; the HOM-dip visibility

$$\mathcal{V}_{\text{HOM}} = 1 - \frac{\text{MIN}}{\text{MAX}} = 1 - \frac{\frac{1}{9}}{\frac{5}{9}} = \frac{4}{5} = 80\% \tag{4.15}$$

reaches its maximum of 80%. If the dip position lies not within the range of the motorized translation stage there are two options: (i) translate the position of the other input coupler or (ii) deliberately induce a phase shift by placing additional components in one arm. It is also possible to utilize differences in the introduced phase shifts between symmetric components already present in the setup, e.g. swap two wave plates.

To optimize interference send in D-polarized light to both arms. Then try to slightly deadjust the output couplers such that they see only the part of the beam that overlaps. When done correctly the number of HH and VV coincidences, corresponding to the t-t and r-r case, respectively, will equalize. Note that while this has a positive effect on the HOM-dip visibility, it might cause a decrease in the overall count rates.

This concludes the alignment process. A picture of the fully assembled setup is shown in Figure 4.8.

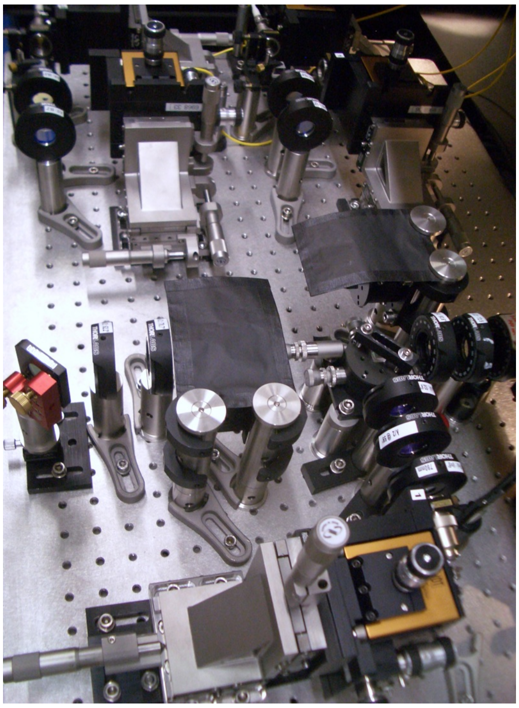

Figure 4.8: *A picture of the completed setup.*

4.2.2 Components

It is useful for later analysis to assess the quality of the individual components.

Polarization-dependent beam splitters

In Section 4.1.2 the optimal reflection/transmission probability ratio of the PDBS $\frac{R_V}{T_V} = 2 \leftrightarrow T_V = \frac{1}{3}, R_V = \frac{2}{3}$ was determined. In general such components are available for purchase. Depending on the specified wavelength it might be necessary to rotate the PDBS about the z axis to achieve the desired ratio. While the transmission probability is quite unaffected by the angle of incident, a small change is observed for the reflection probability. During alignment with a diode laser the ratio can be determined

$$\frac{R_V}{T_V} = 1.99 \pm 0.03$$
$$\Rightarrow \; T_V = 0.334 \pm 0.05 \,.$$

Unfortunately, later on, when using a single-photon source, searching for the HOM-dip may require changing the angle of the input couplers. With all components at their places, several error sources– detectors, wave plates, attenuation PDBS, etc. – make it difficult to reliably readjust the ratio.

Hong-Ou-Mandel dip

A motorized translation stage can be utilized to move one of the input couplers along the direction of the beam path. By changing the position the relative phase difference between the input modes is varied. Figure 4.9 shows the expected behaviour of the VV-coincidence counting rate n. The dip-function is described by [57]

$$n(x) = const. \times \left(1 - \mathcal{V}_{\text{HOM}}\, e^{-\left(\frac{x-x_0}{L}\right)^2}\right) , \tag{4.16}$$

where $\mathcal{V}_{\text{HOM}}$ is the HOM-dip visibility (cf. (4.15)), x the coupler position and L the FWHM of the dip. We further define the HOM-dip quality factor

$$Q \equiv \frac{\mathcal{V}_{\text{HOM}}}{0.8} , \tag{4.17}$$

taking into account the maximal visibility $\mathcal{V}_{\text{HOM}} = 80\%$.

Note that the number of spurious multi-pair emissions greatly influences the HOM-dip visibility. Figure 4.10 plots $\mathcal{V}_{\text{HOM}}$ against the pump laser power that sets the probability of such events: increasing power increases the chance.

For the characterization of the gate the pulsed pump laser was set to an average power of $I = 0.15W$, resulting in

$$\mathcal{V}_{\text{HOM}} = 75.1 \pm 0.5\%$$
$$\Rightarrow \; Q = 93.9 \pm 0.7\% \,.$$

4.3 Testing the gate: Indicative measures

During alignment it is necessary to repeatedly check the current status of the gate to evaluate the progress. A full quantum process tomography, as described in Section 4.5.1, involves an increasingly large number of measurements. Though it is the only comprehensive analysis of a gate's properties, some insight can already be gained by looking at simpler measures.

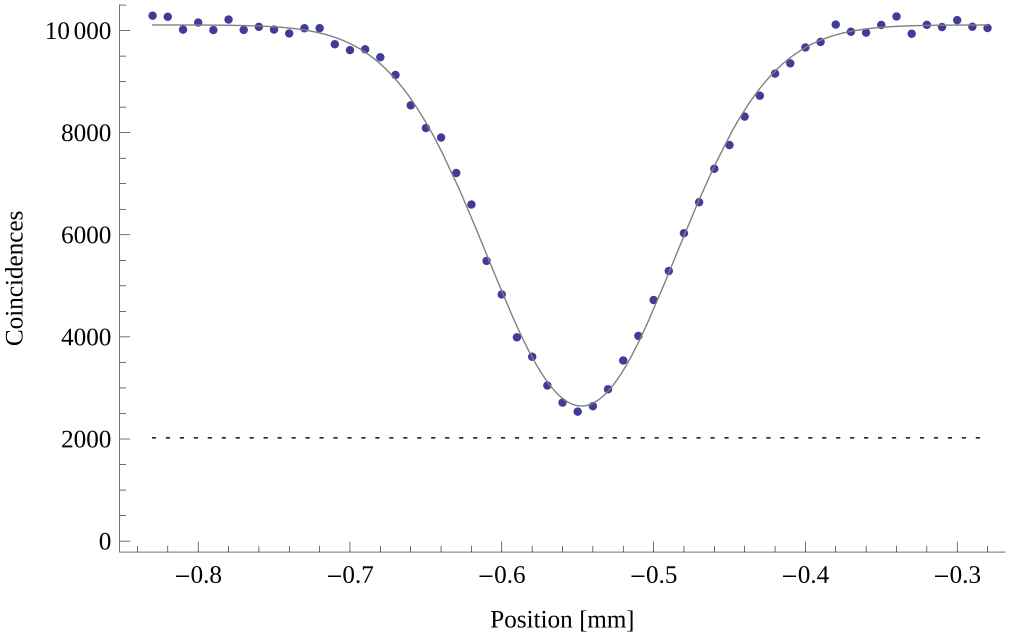

Figure 4.9: *Experimentally determined HOM-dip in* VV *coincidence counting rate.*

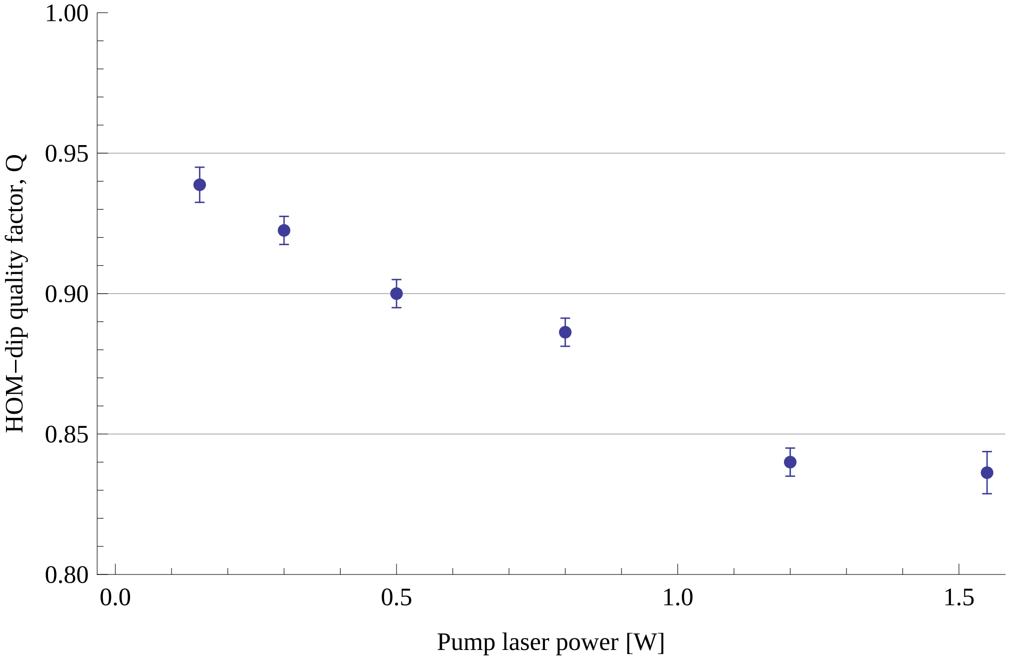

Figure 4.10: *Influence of the SPDC pump laser power on the HOM-dip quality factor. Increasing power increases the number of spurious higher-order emissions that wash out the visibility of the dip.*

4.3.1 Truth table

A good starting point for any gate is to evaluate its truth table. A truth table lists the output of a given operation for each basis state. Table 4.2 and 4.3 show the truth tables of CSIGN and CNOT, respectively. Experimentally the best approximation to a truth table is to make a statistic and calculate output state probabilities for each input. Obviously this makes some truth tables less suitable than others. For instance the sign flip in the CSIGN truth table is lost, whereas the CNOT remains conclusive.

CSIGN		**Output**			
		$\vert HH\rangle$	$\vert HV\rangle$	$\vert VH\rangle$	$\vert VV\rangle$
Input	$\vert HH\rangle$	1	0	0	0
	$\vert HV\rangle$	0	1	0	0
	$\vert VH\rangle$	0	0	1	0
	$\vert VV\rangle$	0	0	0	-1

Table 4.2: CSIGN *truth table*

CNOT		**Output**			
		$\vert HH\rangle$	$\vert HV\rangle$	$\vert VH\rangle$	$\vert VV\rangle$
Input	$\vert HH\rangle$	1	0	0	0
	$\vert HV\rangle$	0	1	0	0
	$\vert VH\rangle$	0	0	0	1
	$\vert VV\rangle$	0	0	1	0

Table 4.3: CNOT *truth table*

For the CNOT gate the experimental results are shown in Figure 4.11 with numbers given in Table 4.4. A first observation yields that there is a certain chance that the CNOT is replaced by an identity operation, visible in the terms where the control qubit is set to $|V\rangle$.

The inquisition $\mathcal{I}$ [58]

$$\mathcal{I} = \frac{\mathrm{Tr}[\mathcal{T}_{exp}\mathcal{T}_{id}^{T}]}{\mathrm{Tr}[\mathcal{T}_{id}\mathcal{T}_{id}^{T}]} \tag{4.18}$$

is a measure of the overlap between the ideal $\mathcal{T}_{id}$ and the experimental $\mathcal{T}_{exp}$ truth table– CNOT: $\mathcal{I} = 92.5 \pm 0.3\%$.

A truth table is by no means a complete description of a gate operation. A general two-qubit input can live in an arbitrary superposition of the basis states or a mixture of these. An interesting feature is that for certain (product state) inputs a CNOT outputs a maximally entangled state, e.g.

$$|A\rangle \otimes |V\rangle \xrightarrow{\text{CNOT}} = |\psi^-\rangle = \frac{1}{\sqrt{2}}(|HV\rangle - |VH\rangle). \tag{4.19}$$

CNOT		**Output**			
		$\lvert HH\rangle$	$\lvert HV\rangle$	$\lvert VH\rangle$	$\lvert VV\rangle$
Input	$\lvert HH\rangle$	0.980	0.005	0.012	0.003
	$\lvert HV\rangle$	0.000	0.982	0.000	0.018
	$\lvert VH\rangle$	0.001	0.001	0.111	0.887
	$\lvert VV\rangle$	0.001	0.008	0.853	0.138

Table 4.4: *Experimental* CNOT *truth table. Errors are less than 0.003.*

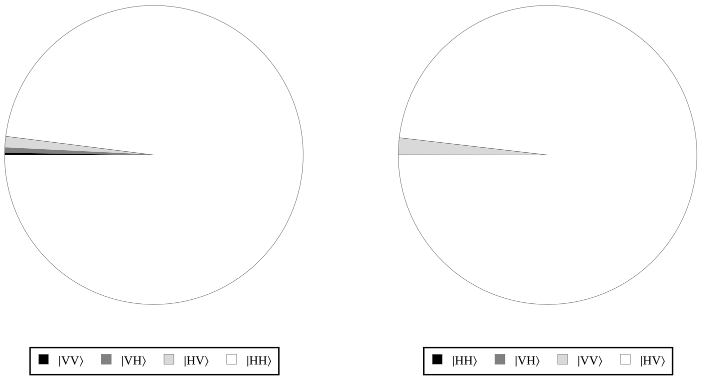

(a) *Input:* $|HH\rangle$ **(b)** *Input:* $|HV\rangle$

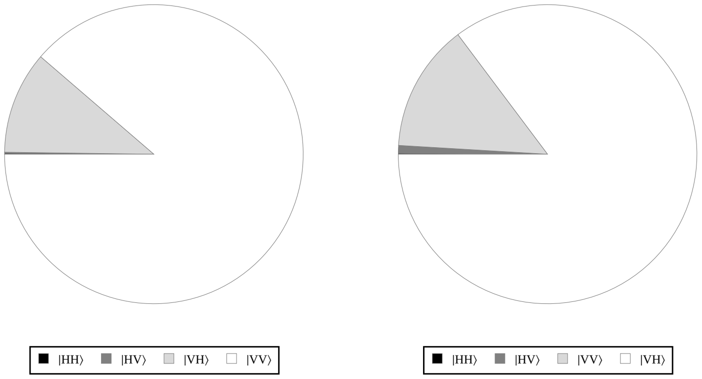

(c) *Input:* $|VH\rangle$ **(d)** *Input:* $|VV\rangle$

Figure 4.11: *Experimentally determined* CNOT *truth table. In each graph (a)-(d) a different computational basis state is used as input. The observed fractions after the* CNOT *operation are shown in the pie chart. The white slice always corresponds to the theoretically expected output, whereas the gray parts belong to spurious outcomes as labelled below each subfigure. Numbers are given in Table 4.4.*

This procedure can also be reversed, hence a CNOT gate is a fully capable Bell state analyser [59, 54].

4.3.2 Bell state visibility

Entanglement production is with no doubt one of the hardest tasks a quantum gate must perform and can thus be prolonged as a good indication of the gate's general performance. Entangled states express nonclassical correlations; ideally a $|\psi^-\rangle$ will only trigger HV and VH coincidence detections. A quick way of checking is to look at the Bell state visibility

$$\mathcal{V}_B = \frac{(-1)^{\psi}\left(C_{HH} - C_{HV} - C_{VH} + C_{VV}\right)}{C_{HH} + C_{HV} + C_{VH} + C_{VV}}\,, \tag{4.20}$$

where $\psi = 0(1)$ if the input Bell state is $|\phi^{\pm}\rangle$ $(|\psi^{\pm}\rangle)$ and C_{XY} is the number of clicks belonging to a XY coincidence, $X, Y = \{H, V\}$. Unity visibility characterizes an ideal CNOT gate. A commendable test is also to compute $\mathcal{V}_B$ for other bases. Table A.3 in the appendix lists the correlations of the four Bell states in the D/A and R/L basis. In Table 4.5, below, the average visibilities of all Bell state outputs from the CNOT are given.

	H/V	D/A	R/L
$\mathcal{V}_B$	$85 \pm 6\%$	$83 \pm 2\%$	$78 \pm 9\%$

Table 4.5: *Bell state visibility in the standard bases.*

4.4 Testing the gate: State measures

A more quantitative picture of the output states' properties can be made, once we have assembled a full description of these states.

4.4.1 Quantum state tomography

The purpose of quantum state tomography (QST) is to reconstruct the density matrix ρ of an unknown quantum state. That is to gain a complete representation of the state and its properties. The theoretical foundation of this procedure is described in [51, 41] and can be adopted to many quantum systems, including photonic qubits. In Figure 4.12 the idea of QST is depicted schematically.

From the no-cloning theorem [60] it is apparent that this technique requires more than a single copy of a state to function. In general the tomographic set for a N-qubit state consists of 4^N measurements and, consequently, at least that many copies of a state are needed. For example the polarization degree of freedom of a photon can be reconstructed by 4 measurements, e.g. in H, V, D and R direction [61]. However,

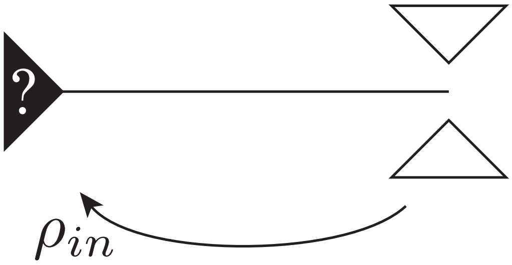

Figure 4.12: *A schematic drawing of quantum state tomography. For an unknown input state, the density matrix can be reconstructed by performing a tomographic set of measurements.*

in the lab, when applied to experimental data, this method typically fails to deliver a physical[7] density matrix. The observed finite counting statistic does not always belong to a valid state. To avoid this problem one can employ a maximum likelihood strategy[8]. The approach differs in that rather to algebraically compute ρ, it attempts to answer the question: What is the *physical* density matrix most likely to yield a set of measurements outcomes? Physicality is enforced by parametrizing $\rho(\vec{t})$ such that it automatically fulfils its requirements [61]. The search is limited to only this set of density matrices.

How can the above question be translated into a mathematical form? If one can assume that the underlying set of data $\{n_b\}$, e.g. the number of clicks at the detector for each measurement basis M_b, was collected independently and forms a sufficiently large statistic[9], the probability of obtaining a certain measurement result is approximately Gaussian distributed. The standard deviation, $\sigma_{n_b} \simeq \sqrt{n_b}$, can be estimated by the Poisson error. The joint probability of the whole set of measurements is then the product of the probabilities of all independent submeasurements

$$P_{\vec{t}}(n_b) = \prod_b exp[-\frac{(n_b - \bar{n}_b)^2}{2\sigma_{n_b}^2}]\,. \tag{4.21}$$

The parameters $\vec{t}$ are included via $\bar{n}_b = \mathcal{N} \times \mathrm{Tr}[M_b\,\rho(\vec{t})]$ and $\mathcal{N}$ is the total number of counts in a measurement setting. The set $\vec{t}$ that maximizes the likelihood function (4.21) specifies the density matrix $\rho(\vec{t})$ closest to the observed measurement data. From the viewpoint of implementation it is favourable to minimize the negative logarithm of the likelihood function instead, which has no effect on the optimal parameters $\vec{t}$.

---

[7] A density matrix ρ is physical, i.e. a normalized, Hermitian, positive-semidefinit operator, if it fulfils the conditions: $Tr\,\rho = 1, \rho = \rho^\dagger$, Eigenvalues : $0 \leq \lambda \leq 1$ and $\Sigma\lambda = 1$.

[8] It is not without difficulties either: while the experimental data leads to an unphysical density matrix of questionable value, the valid one, returned by this method, can only be a fit to the original data.

[9] According to the central limit theorem the Poisson distribution $f(x;n) = \frac{n^x e^{-n}}{x!}$ becomes approximately normal for large values of n, the mean value.

As a final remark to this section Table A.4 and A.5 in the appendix list an efficient setting for overcomplete[10] two-qubit QST that requires to change only the angle of a single wave plate between measurements. For details see the tables' captions.

4.4.2 State measures

Quantum state tomography provides us with a density matrix ρ reconstructed from experimental data. We can use this representation to further analyse the properties of the states created by the CNOT process.

An ideal CNOT operation maps pure states onto pure states. It is instructive to test this attribute for the experimental gate. A suitable measure is linear entropy

$$S_L(\rho) = \frac{N}{N-1}\mathrm{Tr}[\rho^2]. \tag{4.22}$$

For a two-qubit state the dimension $N = 4$. Linear entropy is a simplified version of the von Neumann entropy and as such a measure of the degree of mixedness in a quantum state. A totally mixed state has $S_L = 1$, while a pure state computes to $S_L = 0$.

The other important aspect we want to review again is the creation of entanglement. There are several measures that quantify entanglement and a comprehensive summary of their differences can be found in [62]. Representative to them, we consider entanglement of formation E_F which has a closed form in the two-qubit case [63] and is suitable to pure and mixed states likewise.

As an intuitive reference, Figure 4.13 shows a simulation of both linear entropy and entanglement of formation for the Werner states

$$\rho_W(k) = (1-k)\,\frac{\rho_{\mathbb{1}}}{4} + k\,\rho_{\psi^-}\,, \quad k \in [0,1]. \tag{4.23}$$

The Werner states, parametrized by k, gradually transform from $k = 0$, a totally mixed state $\rho_{\mathbb{1}}$, staying separable until $k = \frac{1}{3}$, to a pure, maximally entangled Bell state ρ_{ψ^-} when $k = 1$. As is required from any general entanglement measure, entanglement of formation is zero for separable states and nonzero when there is entanglement present. Furthermore, it reaches its maximum for the maximal entangled Bell states.

Finally, as a simple measure of the overlap between the expected and the measured output states, we look at the state fidelity expressed in its general form for two density operators [64]

$$F_S(\rho,\sigma) = \mathrm{Tr}\left[\sqrt{\sqrt{\rho}\,\sigma\sqrt{\rho}}\right]^2. \tag{4.24}$$

---

[10] The quality of the fit benefits from using 6^N instead of the minimal 4^N measurement settings [41].

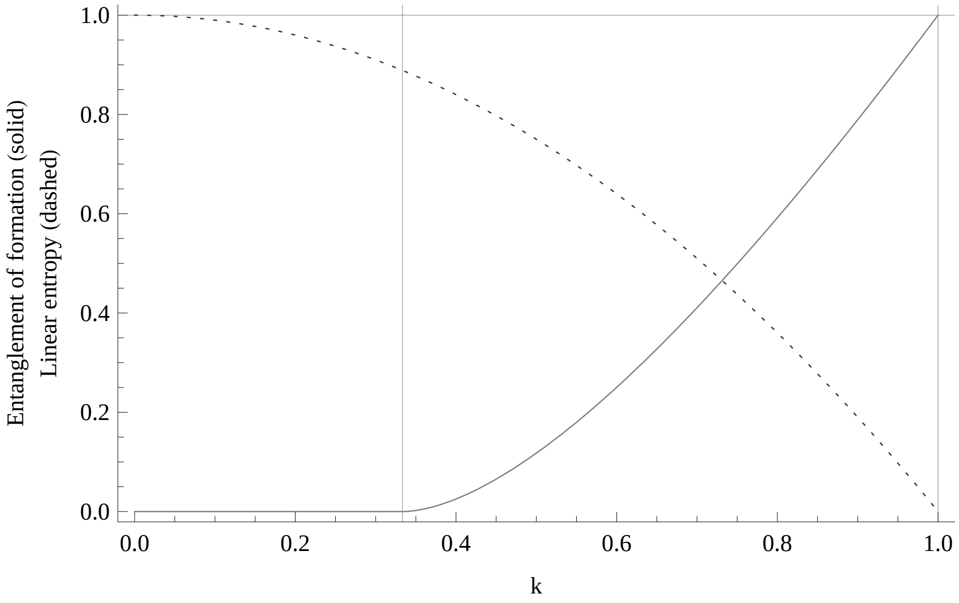

Figure 4.13: *Simulation of linear entropy (dashed) and entanglement of formation (solid) for the Werner states.* $k = 1$ *is a totally mixed state,* $S_L = 1$*, with no entanglement.* $k = 0$ *is a pure,* $S_L = 1$*, maximally entangled state.*

Input	**Output**	F_S	S_L	E_F
$\|HH\rangle$	$\|HH\rangle$	$97.3 \pm 0.2\%$	$4.3 \pm 0.6\%$	$2.8 \pm 0.6\%$
$\|DD\rangle$	$\|DD\rangle$	$97.3 \pm 0.2\%$	$4.6 \pm 0.6\%$	$2.7 \pm 0.7\%$
$\|DV\rangle$	$\|\psi^+\rangle$	$85.3 \pm 0.5\%$	$28 \pm 1\%$	$78 \pm 2\%$
$\|DR\rangle$	$(\frac{\sigma_y+\sigma_z}{\sqrt{2}} \otimes \mathbb{1}) \|\phi^-\rangle$	$86.6 \pm 0.6\%$	$23 \pm 1\%$	$77 \pm 1\%$

Table 4.6: *Experimental values of fidelity, linear entropy and entanglement of formation for some exemplary states produced by the* CNOT *gate.*

Unsurprisingly, the gate works a lot better for inputs that are only subjected to an identity transformation (see Table 4.6). The increased linear entropy suggests the presence of the mixing effect due to imperfect interference as prognosed by the model of Section 4.1.4.

4.4.3 Error estimation

The errors for all measures were estimated by Monte Carlo simulation. To model a photon counting statistic the procedure is outlined below:

1. Calculate the Poisson standard deviation, $\sqrt{n_b}$, for each data point, n_b, corresponding to the number of clicks.

2. Generate a random sample, i, of fluctuated data points, $\tilde{n}_b$, from a Gaussian distribution with standard deviation $\sigma_b = \sqrt{n_b}$.
3. Perform a maximum likelihood QST for the fluctuated data to gain $\tilde{\rho}_i$.
4. Calculate any relevant physical quantity, $f(\tilde{\rho}_i)$, using the reconstructed density matrix and save the result.
5. Repeat steps 2. to 4. a large number, M, times.
6. For the set of M simulations evaluate the standard deviation and use it as an error estimate for the physical quantity f.

As QST is a computationally intensive task an immediate question arises: What is a sufficient value for M? In [41] it was concluded that 200 is– independent of the system size –an adequate number of samples to achieve good convergence for the error estimate. Ideally, convergence should be verified for each measure individually.

Furthermore, it is important to ask what error sources this estimate accounts for? The number of photons that are collected by a detector varies, and follows a Poisson distribution, which describes the occurrence of independent random events, such as the detection of single photons [34]. By randomly selecting the fluctuated samples from a Poisson distribution the error attributed to the counting statistic is simulated.

4.5 Testing the gate: Process measures

The measures introduced in the previous sections provide useful insight in the functioning of the studied gate. However, to fully characterize a quantum gate for arbitrary inputs, a complete description of the process itself is needed. This is where quantum process tomography (QPT) comes into play. As the name already suggests QST and QPT are two related procedures with similar objectives. It turns out that QST is used as a subroutine in QPT. Figure 4.14 shows a schematic representation of QPT. The reader is encouraged to compare it to Figure 4.12 to understand the differences of both scenarios.

4.5.1 Quantum process tomography

Any quantum process $\mathcal{E}$ on an arbitrary input state ρ can be written in the operator-sum representation (or Kraus representation) as [51]:

$$\rho_{\text{out}} \equiv \mathcal{E}(\rho) = \sum_k E_k \rho E_k^\dagger \, . \tag{4.25}$$

The operation elements (or Kraus operators) E_k adhere to the condition $\Sigma_j E_j^\dagger E_j \leq \mathbb{1}$, where equality is met by trace preserving maps. For a given process the operator-sum representation is not unique, yet any valid set $\{E_k\}$ completely characterizes the operation.

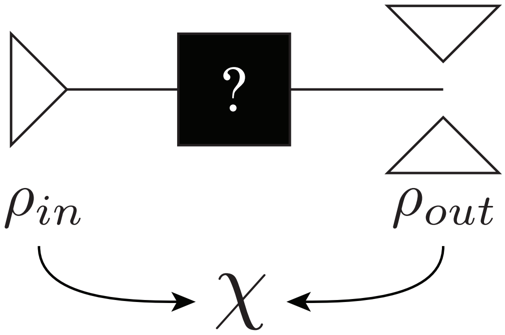

Figure 4.14: *A schematic drawing of quantum process tomography. For an unknown quantum process, the process matrix χ can be reconstructed by performing QST on each state of a tomographic set of input states.*

To relate different processes to each other it is convenient to choose a fixed operator basis[11] $\{\tilde{E}_j\}$. By the transformation rule $E_i = \Sigma_m a_{im} \tilde{E}_m$, we get

$$\mathcal{E}(\rho) = \sum_{m,n} \chi_{mn} \tilde{E}_m \rho \tilde{E}_n^\dagger, . \tag{4.26}$$

where $\chi_{mn} = \Sigma_i a_{im} a_{in}^*$ is a completely positive[12] Hermitian matrix that describes the process in the chosen basis. Hence χ_{mn} is commonly referred to as *process matrix*. The operation elements E_k may be reconstructed from it. Since χ_{mn} is positive, it can be brought to diagonal form $\chi = UDU^\dagger$ by some unitary operator U. Then

$$E_k = \sqrt{D_{kk}} \sum_m U_{mk} \tilde{E}_m \tag{4.27}$$

are operation elements for $\mathcal{E}$ [51].

As was pointed out in Figure 4.14 the setting of QPT contains an initially unknown process– a black box –which can be studied only by observing its effect on an arbitrarily chosen input. A basis of linear independent states[13], $\{\tilde{\rho}_i\}$, suggests itself as a reasonable choice. Performing QST on the output $\mathcal{E}(\rho_i)$ of each basis state ρ_i contains all necessary information to find

$$\mathcal{E}(\rho) = \mathcal{E}(\sum_i \mu_i \tilde{\rho}_i) = \sum_i \mu_i \mathcal{E}(\tilde{\rho}_i)\,, \tag{4.28}$$

for an arbitrary input. The process matrix can then be inferred by solving a system of linear equations [51, 58].

---

[11] A common choice is the Pauli basis, consisting of mutual tensor products of the Pauli operators $\{\mathbb{1}, \mathrm{X}, \mathrm{Y}, \mathrm{Z}\}$.

[12] A *completely positive map* transforms a positive operator, e.g. a density operator, to another positive operator. In contrast to a *positive map* this holds true also when acting nontrivially only on a subspace of the whole system.

[13] In this context also referred to as a tomographic set of input states.

Precise implementation of this procedure will run into the same problems already encountered for QST; the resulting process matrix is likely to be malformed, predicting unphysical states. Alternatively, we can pursue a maximum likelihood strategy. At this point there seem to be two valid options to proceed:

(i) Use the measured data to reconstruct physical states via maximum likelihood QST. Then calculate the process matrix algebraically as outlined above.

(ii) Use the measured data to directly infer a physical process matrix in an adapted maximum likelihood search.

Option (i) comes with the benefit that we can repurpose the implementation used for QST. A closer look reveals, however, that (i) delivers an unphysical process matrix:

```
Eigenvalues@cnotpmI
{-0.0861267, -0.0570671, -0.0462674 , -0.0408027 ,
 -0.0250175, -0.019107 , -0.00161173,  0.00698909,
  0.0107476,  0.0286284,  0.0383255 ,  0.0472131 ,
  0.0648666,  0.086464 ,  0.122097  ,  0.870669   }
```

Some of the eigenvalues are negative. This is not case for (ii)

```
Eigenvalues@cnotpmII
{ 0        , 0        , 0          , 0          ,
  0        , 0        , 0          , 0          ,
  0        , 0        , 0.00050129,  0.00148846,
  0.0087337, 0.0189628, 0.09772420,  0.87259000 },
```

or the theoretical CNOT process matrix

```
Eigenvalues@cnotpmIDEAL
{ 0        , 0        , 0          , 0          ,
  0        , 0        , 0          , 0          ,
  0        , 0        , 0          , 0          ,
  0        , 0        , 0          , 1          }.
```

Why does method (i) fail? It makes the implicit assumption that any set of physical output states is related by a physical and *consistent* process matrix. This seems[14] not to be the case. By performing the maximum likelihood reconstructions independently for each input, the resulting states randomly drift apart leaving the boundaries of a consistent set. In (ii) this problem is avoided by obtaining the process reconstruction in a single unified procedure that restricts its solutions to only completely positive process matrices.

The downside of any physical process matrix reconstruction is that it yields only an approximation to the experimental process. Initially, there is no information about how faithfully it describes the raw data.

---

[14] Private discussion with J. Kofler, N. K. Langford and S. Ramelow

A first attempt is to compare the output states predicted by the reconstructed process matrix with the experimentally determined output states of the tomographic set. This returns an average fidelity of 97 ± 2%. However, to be able to compute the fidelity we used the density matrices of the experimental states. This implicitly included a maximum likelihood search. So the average fidelity is more a measure of how much the output states are drifted apart from a consistent set, than it is a measure of how close the process matrix is to the experimental data.

We need to relate the predictions of the reconstructed process matrix $\tilde{\chi}$ directly to the measurement outcomes. One option is to calculate the residuals

$$\begin{aligned}\Delta_{ab} &= p_{ab} - \mathrm{Tr}[M_b\,\mathcal{E}(\rho_a)] = \\ &= p_{ab} - \sum_{m,n} \langle b|\,\tilde{P}_m\,|a\rangle\,\langle a|\,\tilde{P}_n\,|b\rangle\,\tilde{\chi}_{mn}\,.\end{aligned} \tag{4.29}$$

Given the experimentally determined measurement probabilities p_{ab}, they contain the differences between them and the corresponding probabilities predicted from $\tilde{\chi}$. The process, $\mathcal{E}$, represented in the Pauli basis, $\tilde{P}_m$, acts on a set of input states, $\{\rho_a\}$, while a measurement setting, M_b, is applied. A histogram of the residuals is shown in Figure 4.15. The width of the distribution, $\sigma(\Delta_{ab}) = 0.044 \pm 0.005$, gives an idea of how close the predictions of the process matrix are to the raw data.

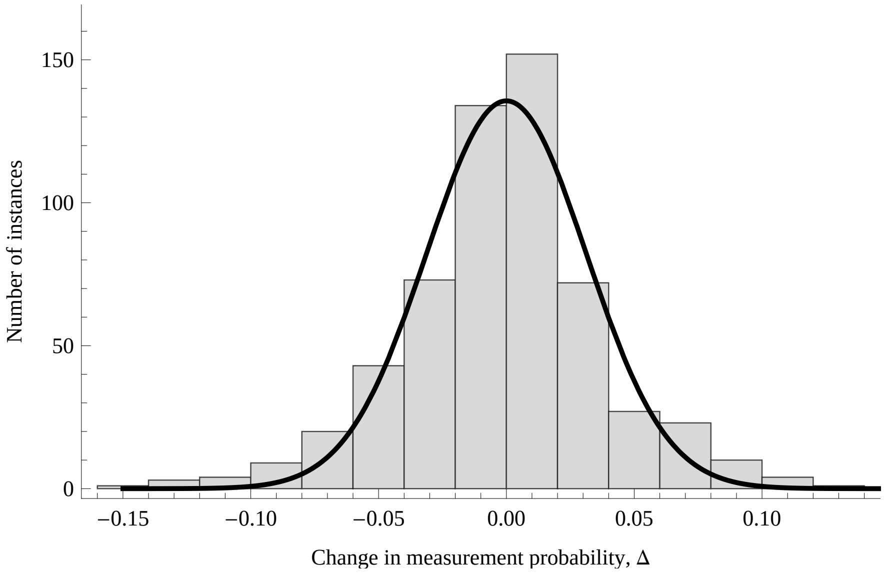

Figure 4.15: *A histogram of the differences between measurement probabilities predicted by $\tilde{\chi}$ and those observed in the experiment. The width of the distribution provides information about the proximity of $\tilde{\chi}$ to the data.*

4.5.2 Process measures

Proximity of $\tilde{\chi}$ to the experimental data is one part, now we want to study how well the gate implements the intended CNOT operation. We can again evaluate the average fidelity of the tomographic set. In this case comparing the experimental and theoretical output states: $90 \pm 7\%$.

But since we have obtained a description of the process itself, we want to use it for characterizing the gate. In [65] a set of measures suited for this purpose have been identified, along with a catalogue of requirements: Most importantly it should (i) be a metric; (ii) be easy to calculate; (iii) be easy to measure; and (iv) have a nice physical interpretation.

The *process fidelity*

$$F_p(\tilde{\chi}, \chi) \equiv \mathrm{Tr}[\tilde{\chi} \cdot \chi] \tag{4.30}$$

and the *process distance*

$$D_p(\tilde{\chi}, \chi) \equiv \frac{\mathrm{Tr}[|\tilde{\chi} - \chi|]}{2} \tag{4.31}$$

both match the above criteria. Their physical interpretation is that they bound on the average probability of error $\bar{P}_e$, i.e. a calculation performed with the gate is opt fail[15] on average less than $\bar{P}_e$,

$$\bar{P}_e \leq 1 - F_p(\tilde{\chi}, \chi), \tag{4.32}$$

$$\bar{P}_e \leq D_p(\tilde{\chi}, \chi). \tag{4.33}$$

These measures evaluated for the CNOT gate are

$$\begin{aligned} F_p &= 86.0 \pm 0.3\% & \Rightarrow \quad & \bar{P}_e \leq 14.0 \pm 0.3\% \\ D_p &= 22.9 \pm 0.6\% & \Rightarrow \quad & \bar{P}_e \leq 22.9 \pm 0.6\% \,. \end{aligned}$$

Figure 4.16 compares $\tilde{\chi}$ to the theoretical process matrix. The ideal CNOT with respect to the Pauli operator basis is real and has 16 nonzero matrix elements. In Figure 4.17 the relative size of the corresponding elements in $\tilde{\chi}$ is shown.

It is difficult to directly interpret the process matrix in an intuitive way, as it makes sense only in conjunction with the chosen operator basis and for a specific input state. The size of the χ_{11} element indicates the increased tendency of the gate to act as an identity operation

$$\rho_{\text{out}} = \sum_{m,n} \tilde{P}_m \, \rho_{\text{in}} \, \tilde{P}_n \, \tilde{\chi}_{mn} \tag{4.34}$$

$$\xrightarrow{m,n=1} (\mathbb{1} \otimes \mathbb{1}) \, \rho_{\text{in}} \, (\mathbb{1} \otimes \mathbb{1}) \tilde{\chi}_{11} \,. \tag{4.35}$$

---

[15] This assumes that a probabilistic gate has successfully functioned in the first place. In our case this chance is 1/9 and indicated by a coincidence detection.

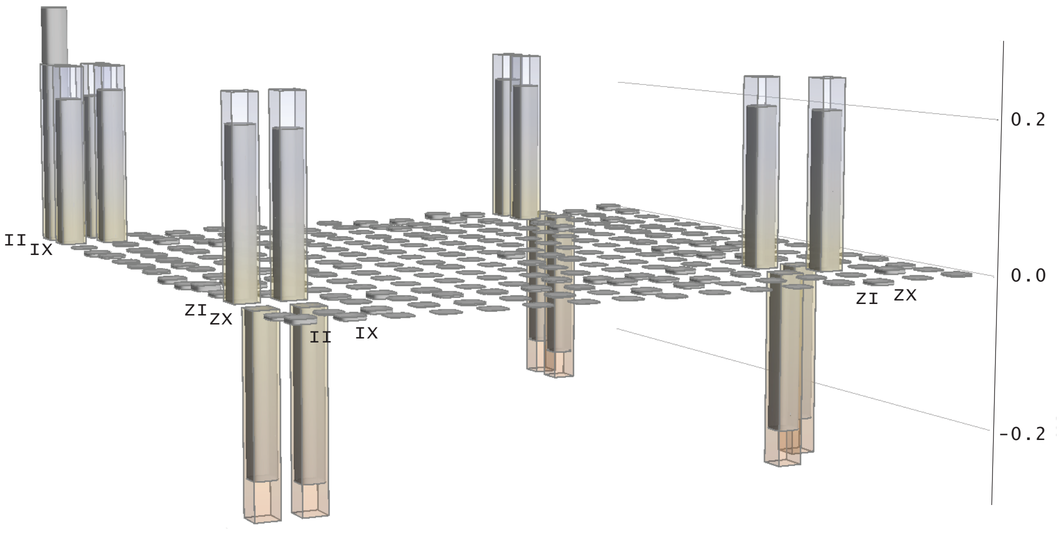

Figure 4.16: *Comparing the ideal* CNOT *process matrix (wireframe) to the one reconstructed from experimental data (solid bars). The matrix is represented in the Pauli operator basis and only the real part is shown. Imaginary parts are smaller than 0.03.*

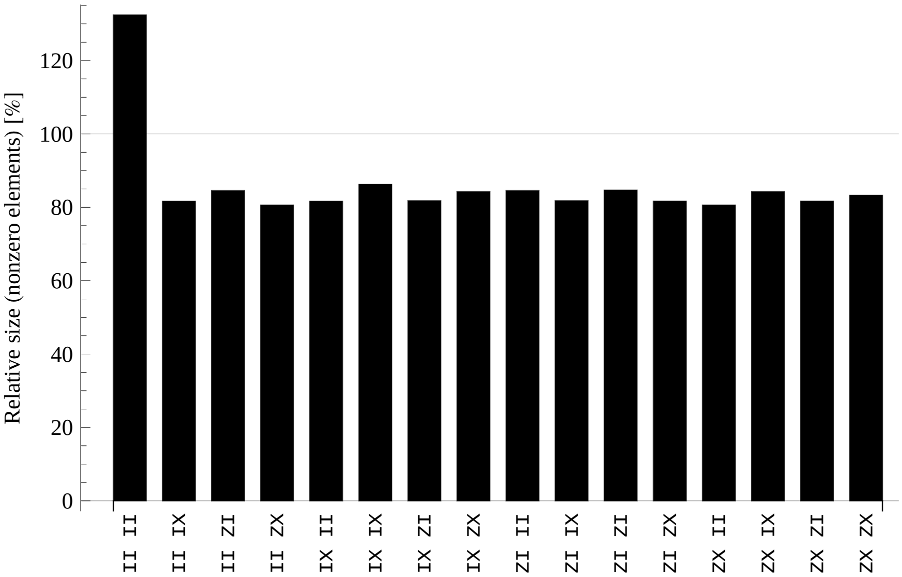

Figure 4.17: *Relative size of ideally nonzero elements in the experimental* CNOT *process matrix.*

4.5.3 Error analysis

Do these results line up with our expectations? We previously identified two critical components that are likely to disturb the process: (i) the T_V transmission probability for vertically polarized light of the PDBS and (ii) the HOM-dip visibility, which is affected by the mode overlap, multiple-pair emissions and how indistinguishable the cases both photons reflected/transmitted are. The effect of either error source on the process fidelity F_p has been simulated in Figure 4.2 and 4.5, where the quality of the latter is expected to have a much greater impact. In Section 4.2.2 we measured $T_V = 33.4 \pm 0.5\%$ and evaluated the HOM-dip quality factor to be $Q = 93.9 \pm 0.7\%$.

By virtue of the maximum likelihood technique used for QPT we can determine the model closest to the data. Instead of parametrizing the process matrix $\tilde{\chi}$ such that it is physical, an already physical model[16] $\tilde{\chi}(\tilde{Q})$ based on the HOM-dip quality factor is applied. The adapted likelihood function is maximized for $\tilde{Q} = 94.001\%$, which is in good agreement to the experimentally determined value.

But to assess the validity of this result, we must first examine how close this model actually is to the data? We can repurpose the earlier approach of calculating the residuals (4.29) that contain the change in measurement probabilities compared to the raw data. The width of the distribution (Figure 4.18) is $\sigma_{\tilde{Q}}(\Delta) = 0.06 \pm 0.01$. As expected it is higher than the width $\sigma(\Delta) = 0.044 \pm 0.005$ corresponding to $\tilde{\chi}$ of the QPT maximum likelihood reconstruction (cf. Figure 4.15). Nevertheless, the model appears to hold a good description of the observed process.

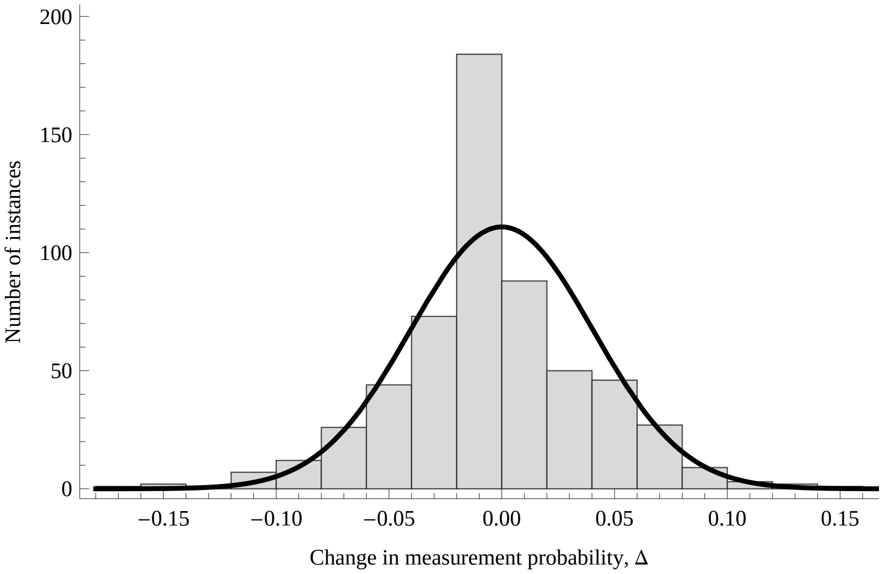

Figure 4.18: *A histogram of the differences between measurement probabilities predicted by* $\tilde{\chi}(\tilde{Q})$ *and those observed in the experiment. The width of the distribution is an estimate of how close the model describes the raw data.*

---

[16] see (4.14)

Chapter 5

Increasing the computational depth

5.1 Universal two-qubit quantum computer

A universal two-qubit quantum computer is a device that can implement any 4×4 unitary operation $U \in \mathrm{U}(4)$. It is widely known [66, 67, 68] for a general U to be decomposable into three CNOT gates together with single-qubit unitaries w_i

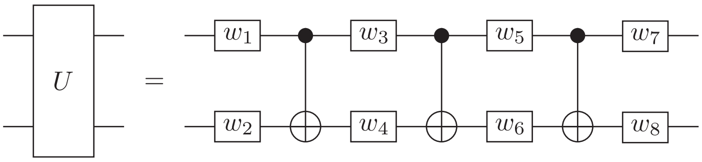

The above circuit is not uniquely determined. Each w_i has three free parameters, making it 24 in total. In contrast, the 4×4 unitary matrix we seek to implement, is characterized by only 16. Any $U \in \mathrm{U}(4)$ may additionally be transformed to $\mathrm{SU}(4)$ by multiplying it with a global phase $(\det U)^{-1/4}$. The additional constraint, $\det U = 1$, fixes another parameter, leaving 15 unset. Using this freedom we choose

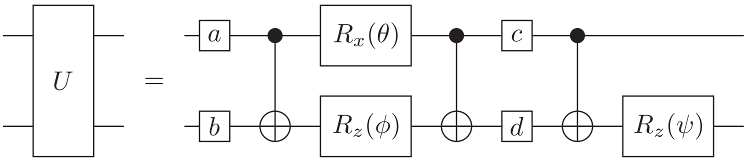

another valid decomposition. For a particular algorithm the single-qubit unitaries a, b, c, d as well as the angles α, β, γ for the Bloch rotations R_x and R_z must be computed. The procedure is described in [69]. Refer to Chapter 3 for how to implement the unitaries with wave plates.

We can try to further lower the resources required on the quantum side. In order for an algorithm to be useful it must have some return value. The output is obtained from a measurement on the final state.

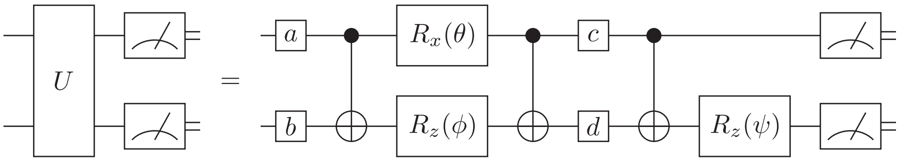

We can assume that the measurement will take place in the computational basis H/V. If otherwise, the basis change can be incorporated into U and the total matrix decomposed again. This justifies our earlier choice for the w_i. A rotation about the z axis of the Bloch sphere leaves the result of a projective Z measurement unchanged. The final R_z is obsolete and can be removed. The third CNOT operation is now immediately followed by the readout. Prior to this CNOT the state of the computation– some two-qubit state –can be written as $|\psi\rangle = c_{HH}\,|HH\rangle + c_{HV}\,|HV\rangle + c_{VH}\,|VH\rangle + c_{VV}\,|VV\rangle$. Measuring control and target qubit in the computational basis does nothing else than projecting onto one of these four terms. From its truth table (cf. Table 4.3) we know that the effect of a CNOT is to interchange the amplitudes c_{VH} and c_{VV}. But this operation can be performed in a classical postprocessing step. Whenever $|VH\rangle$ is observed it is counted as $|VV\rangle$ and vice versa. In circuit language the following holds true

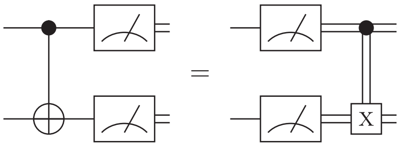

and applied to the full circuit brings us

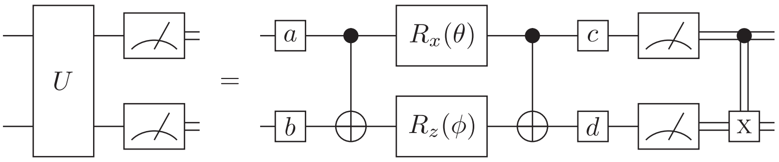

This is a considerable relaxation to the requirements of a universal two-qubit quantum computer [69].

5.2 Towards an experimental implementation

There exist several CNOT gate architectures for linear optics [70, 71, 72, 73, 74, 54, 55, 56] shown in Figures 5.2 to 5.5. The working principle of each gate is explained in the caption. All symbols appearing in the schematic drawings are labelled in Figure 5.1.

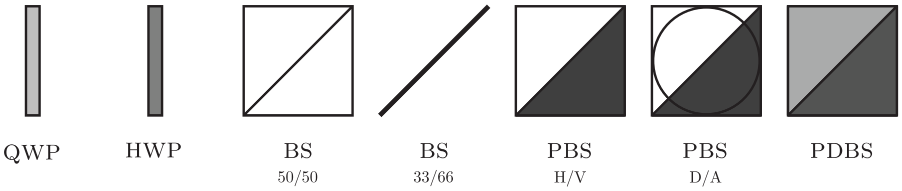

Figure 5.1: *The optical elements used in the various* CNOT *architectures.*

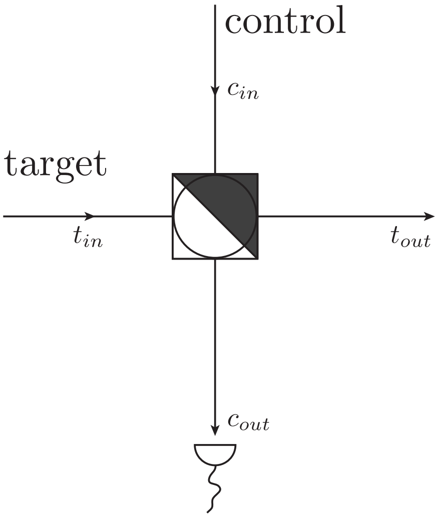

Figure 5.2: *Setup **A** — is a simple implementation of a destructive* CNOT *that uses only a PBS operating in D/A basis. The gate's success is conditioned to the detection of the control qubit in a specific state [70].*

Table 5.1 holds a side-by-side comparison of important features found in the different CNOT gate architectures.

As much as the CNOT gates play a crucial part in the universal two-qubit quantum computer, it is necessary to uphold the freedom to perform single-qubit gates in between. All gate architectures rely on measurement-based nonlinearities and thus apply some kind of postselection on the detected events. The type of success notification becomes relevant: single-qubit unitaries in succession to the gate operation

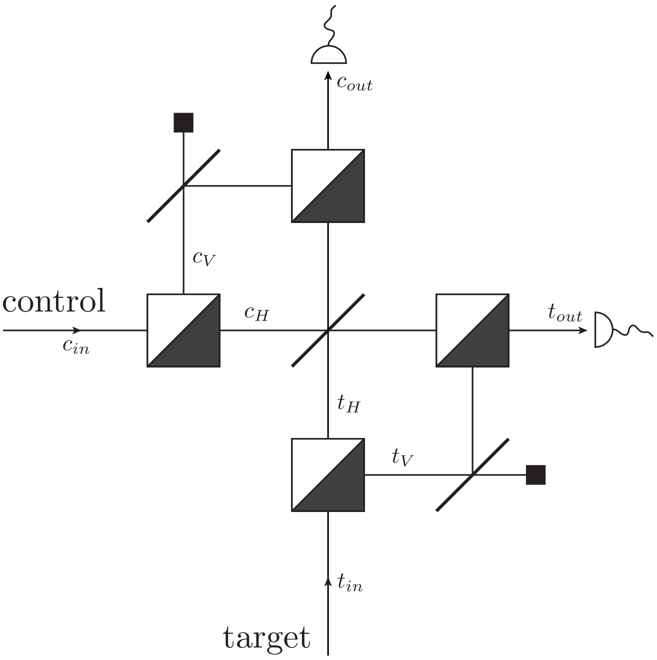
c_{out}
c_V
control
c_{in}
c_H
t_{out}
t_H
t_V
t_{in}
target

Figure 5.3: *Setup **B** — temporarily converts control and target qubit to path encoding [73]. An interferometric structure of BS with transmission probability $\frac{2}{3}$ applies a* CSIGN *conditioned on a coincidence detection [72, 74]. The gate operation can be changed to* CNOT *by appending half-wave plates to the target arm (not shown).*

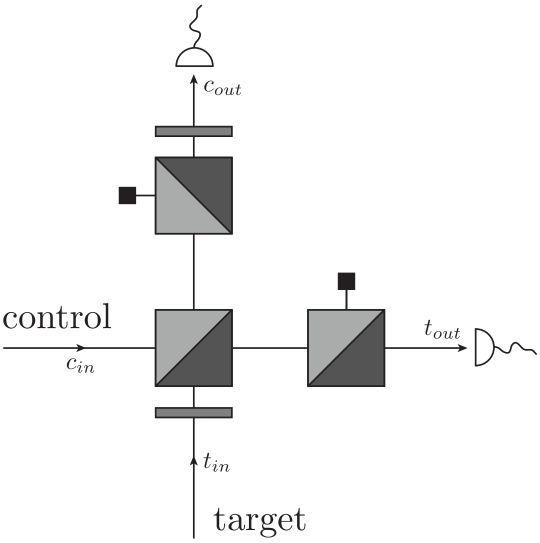
c_{out}
control
c_{in}
t_{out}
t_{in}
target

Figure 5.4: *Setup **C** — is the* CNOT *gate already presented in Chapter 4. The gate makes use of PDBSs and a two-photon interference effect to achieve the controlled operation [54, 55, 56].*

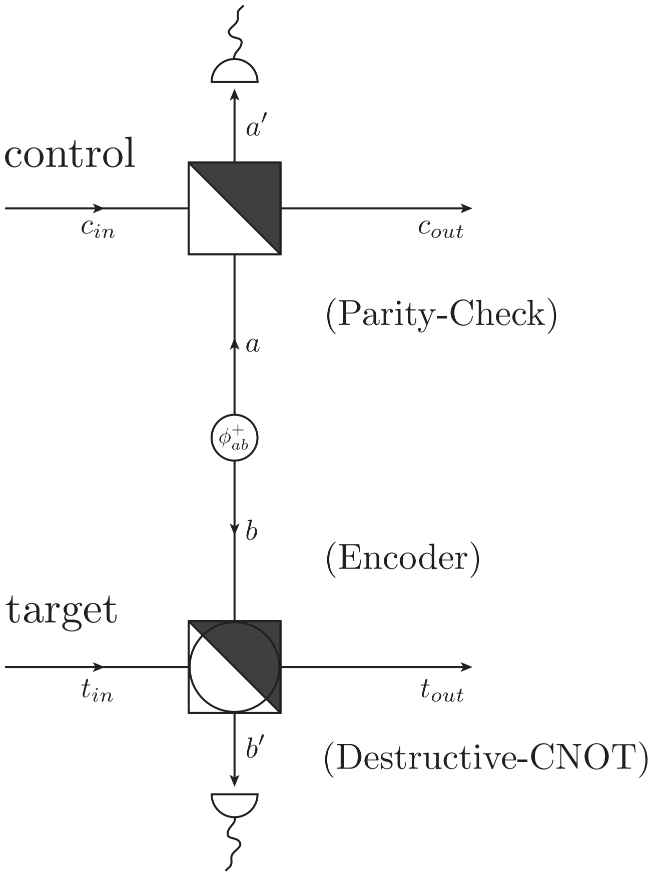

Figure 5.5: *Setup **D** — combines three smaller entities to a feed-forwardable* CNOT *[70, 71]. The parity-check uses a PBS to transfer the value of the qubit in mode c_{in} into mode c_{out}, provided that its value is the same as that of the second input qubit in mode a. A pair of ancilla qubits, $|\phi^+\rangle$, assures that the value of the control qubit is also encoded to mode b. Together with the target qubit it is committed to the destructive* CNOT *of setup **A**.*

alter the state of the qubits. In case of setup **A** this conflicts with requirement to detect a specific state to indicate a successful run. **A** must therefore be removed from the list of suitable candidates. Note that although setup **D** is based on the same postselection method, it applies only to the ancilla qubits whose state remains unchanged. The coincidence detection based scheme of setup **B** and **C** is robust against further single-qubit operations.

Basically, their design is very similar. The most notable difference is the use of path and polarization encoding of the qubits. While it is possible to convert one into the other, the required additional interferometric paths in **B** are a source of instability, particularly, in free space implementations. In terms of stability **C** is also favourable to the more complicated architecture of gate **D**. The conclusion should therefore be to use CNOT gates of type **C** to implement the universal quantum

	A	**B**	**C**	**D**
	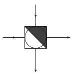	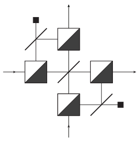	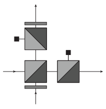	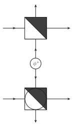
Qubits	2	2	2	2+2
Encoding	pol.	path	pol.	pol.
Interferometric elem.	one	multiple	one	multiple
Nonlinearity	— measurement-induced —			
Success indication	state	coinc.	coinc.	state (ancilla)
Destructive	yes	yes	yes	no

Table 5.1: *A side-by-side comparison of linear optics two-qubit gates.*

computer scheme. But when concatenating **C**, a new problem emerges: The spurious events related to two photons ending up in the same mode after the operation of the first gate, previously sifted out by filtering for coincidences, suddenly can lead to false positive events. The two photons regain the opportunity to distribute themselves during the operation of the second CNOT. A simultaneous detection in target and control arm is no longer an unambiguous indication of a successful run. Gate **C** is not feed-forwardable, the immediate detection of the logical qubits is mandatory, i.e. its attribute to be destructive.

In **D** this problem is compensated by introducing another pair of photons (ancilla). The gate operation is monitored by the state of these ancilla photons. The photons corresponding to control and target qubit can pass through unhindered and are available for further processing. However, this happens at the cost of an additional two ancilla photons per CNOT. While six-photon experiments have been carried out [75, 76] the they suffer from low count rates leading to exceedingly long measurement times.

With present technology this approach seems unsuitable. A closer look reveals that feed-forwardability is required only for the first of the two CNOT. A combination of **C** and **D**, requiring only four photons, may serve as an alternative. Starting with a gate of type **D**, the output can be feed-forwarded to **C** being used as an endpiece. Figure 5.6 combines both setups to an universal two-qubit quantum computer. A fourfold-coincidence at detectors D1-D4 confirms a successful run.

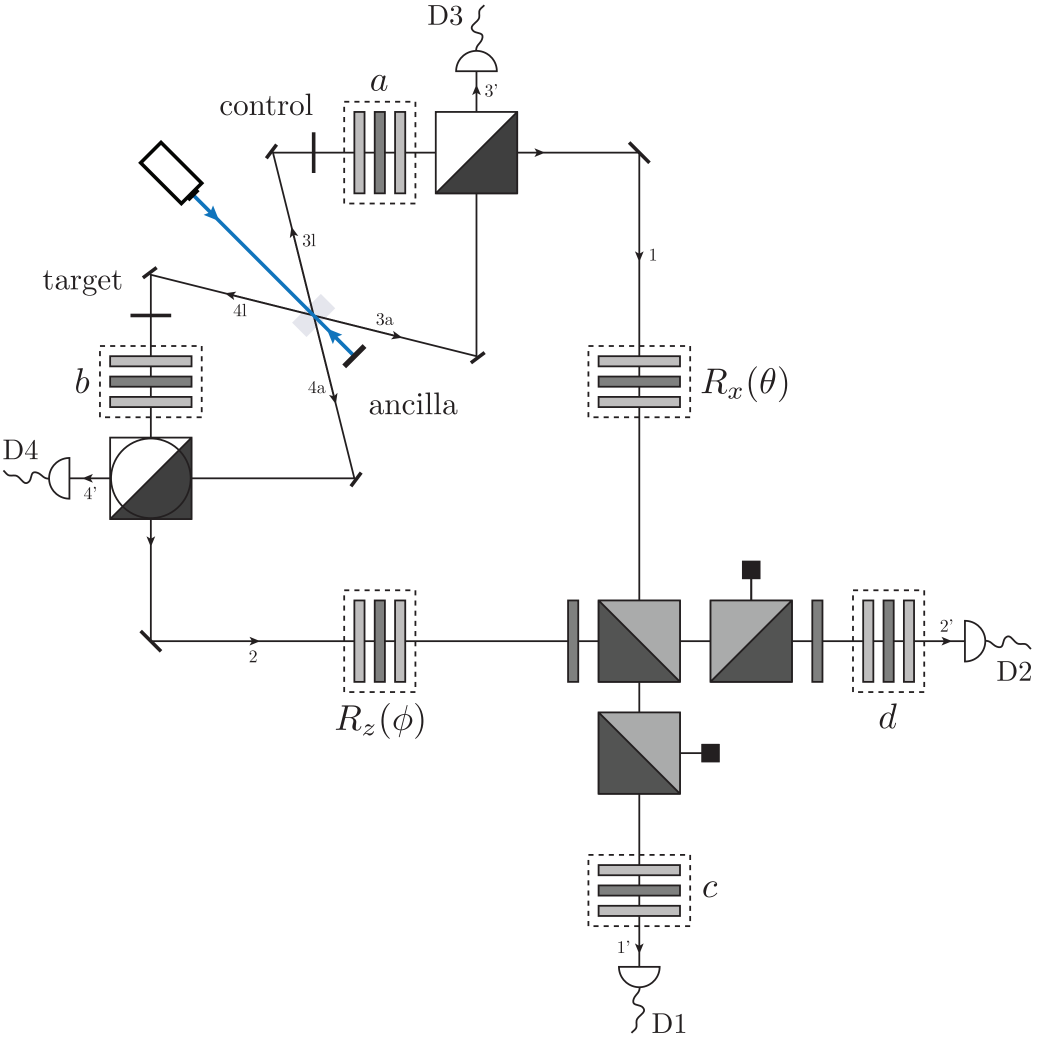
D3
3'
a
control
3l
1
target
4l
3a
b
4a
ancilla
$R_x(\theta)$
D4
4'
2
2'
D2
$R_z(\phi)$
d
c
1'
D1

Figure 5.6: *Experimental implementation of a universal two-qubit quantum computer. The setup is a combination of **C** and **D**. In addition to the control and target qubit, two ancilla qubits are needed in the first* CNOT*. A successful run is indicated by a fourfold-coincidence at detectors D1-D4. Not shown is the concluding* CNOT *applied through classical postprocessing.*

5.3 Possible issues

A problem inherited from setup **D** is due to the probabilistic nature of the SPDC photon source. To properly function one pair must exit the nonlinear crystal in forward direction, while the other is created on the return pass. That way two photons are in the control/target arm and two more occupy the ancillary Bell state modes. It is, however, equally likely that both pairs are produced in a single pass [77]. This may disturb the success indication required for postselection. Let us examine each case individually: When two $|\phi^+\rangle$-pairs are created in the ancillary arm a fourfold-coincidence in detectors D1-D4 is impossible. This is obvious when both photons are either reflected or transmitted at the PBS before D3. The other possibility– the photons split up at this PBS –implies that they have different polarizations. A quick calculation

$$\begin{aligned} H_4V_4 &= \frac{1}{2}(D_{4l}+A_{4l})(D_{4l}-A_{4l}) = \frac{1}{2}(D_{4l}D_{4l}-D_{4l}A_{4l}+A_{4l}D_{4l}-A_{4l}A_{4l}) \\ &= \frac{1}{\sqrt{2}}(D_{4l}D_{4l}-A_{4l}A_{4l}) \\ \overset{PBS^{D/A}}{\longrightarrow} &\quad \frac{1}{\sqrt{2}}(D_{4'}D_{4'}+A_2A_2) \end{aligned} \tag{5.1}$$

confirms that the photons will take the same path at the lower PBS, which again excludes a fourfold-coincidence.

The situation is less comfortable when the double-pair emission is directed towards the logical arm. A universal quantum computer needs to process arbitrary inputs. This includes cases where the four photons end up in all four detector modes 1'-4', usually expected to indicate a successful gate operation. The contribution of this error source depends on the particular input state, see Figure 5.7. When we assume the input to be a product state a double-pair emission in the logical arm yields on the control side (3l)

$$(\eta_c H+\nu_c V)\otimes(\eta_c H+\nu_c V) = \underbrace{\eta_c^2\,HH+\nu_c^2\,VV}_{neutral}+\underbrace{\eta_c\nu_c\,HV+\eta_c\nu_c\,VH}_{unwanted} \tag{5.2}$$

and on the target side (4l)

$$\begin{aligned} (\eta_t H+\nu_t V)\otimes(\eta_t H+\nu_t V) =& \underbrace{(\frac{\eta_t^2}{2}+\eta_t\nu_t+\frac{\nu_t^2}{2})\,DD+(\frac{\eta_t^2}{2}-\eta_t\nu_t+\frac{\nu_t^2}{2})\,AA}_{neutral} \\ &+\underbrace{(\frac{\eta_t^2}{2}-\frac{\nu_t^2}{2})\,DA+(\frac{\eta_t^2}{2}-\frac{\nu_t^2}{2})\,AD}_{unwanted}\ . \end{aligned} \tag{5.3}$$

If the control qubit is either $|V_{3l}\rangle$ or $|H_{3l}\rangle$, i.e. $\eta_c=\{0,1\}$, no spurious fourfold coincidences occur[1]. The same holds true when on the target side $\eta_t = 1/\sqrt{2}$.

---

[1] We recall that the amplitudes are related by normalization $|\eta|^2+|\nu|^2=1$.

Differently, if the two-qubit input is of the kind $|D_{3l}H_{4l}\rangle$, meaning that $\eta_c = 1/\sqrt{2}$ and $\eta_t = 1$, $\frac{1}{16}$ of the double-pair emissions trigger a false success notification. Quite notably regarding the same $\frac{1}{16}$ chance of the gate to truthfully succeed. Note that due to the PBSs in both the control and target arm the spurious state after the CNOT gate is always $|H_1 D_2\rangle$. So the effective impact of the four-photon noise depends on the input state[2]

$$F_S(\, \rho_{\text{in}}(\eta_c, \eta_t), |HD\rangle\, \langle HD|\,)\,. \tag{5.4}$$

Furthermore, the ratio between *neutral* and *unwanted* events is not constant either, see (5.2) and (5.3).

A way to reduce the impact of this error is by deliberately attenuating or defocusing the pump beam on the return trip. Assuming that p (q) is the probability for pair creation event on the first (second) pass, the chances for the three four-photon emissions scale like:

- p^2 : both in the first pass (*neutral*)
- pq : one in each pass (*desired*)
- q^2 : both in the second pass (*unwanted*)

By lowering q as described, the signal-to-noise ratio, p/q, can be set appropriately, so that the contribution of the *unwanted* events becomes negligible. It should be noted that the previous discussion is irrespective of the concatenation with setup **C**.

Another challenge is constituted by higher-order emissions. Three or more photon pairs completely erode the reliability of the coincidence success indicator. Unless number resolving detectors are used, the only way to cope with them is to limit the introduced noise by reducing the pump beam power. The setup also looses its immunity against noise from the ancilla arm when subjected to multi-pair emissions. Thus improving the signal-to-noise ratio, p/q, necessarily means lowering q rather than increasing p.

---

[2] It is possible to consider the input state here as the fidelity is invariant under unitary transformation: $F_S(U\,\rho\,U^\dagger, U\,\sigma\,U^\dagger) = F_S(\rho, \sigma)$. Also, CNOT $|HD\rangle = |HD\rangle$.

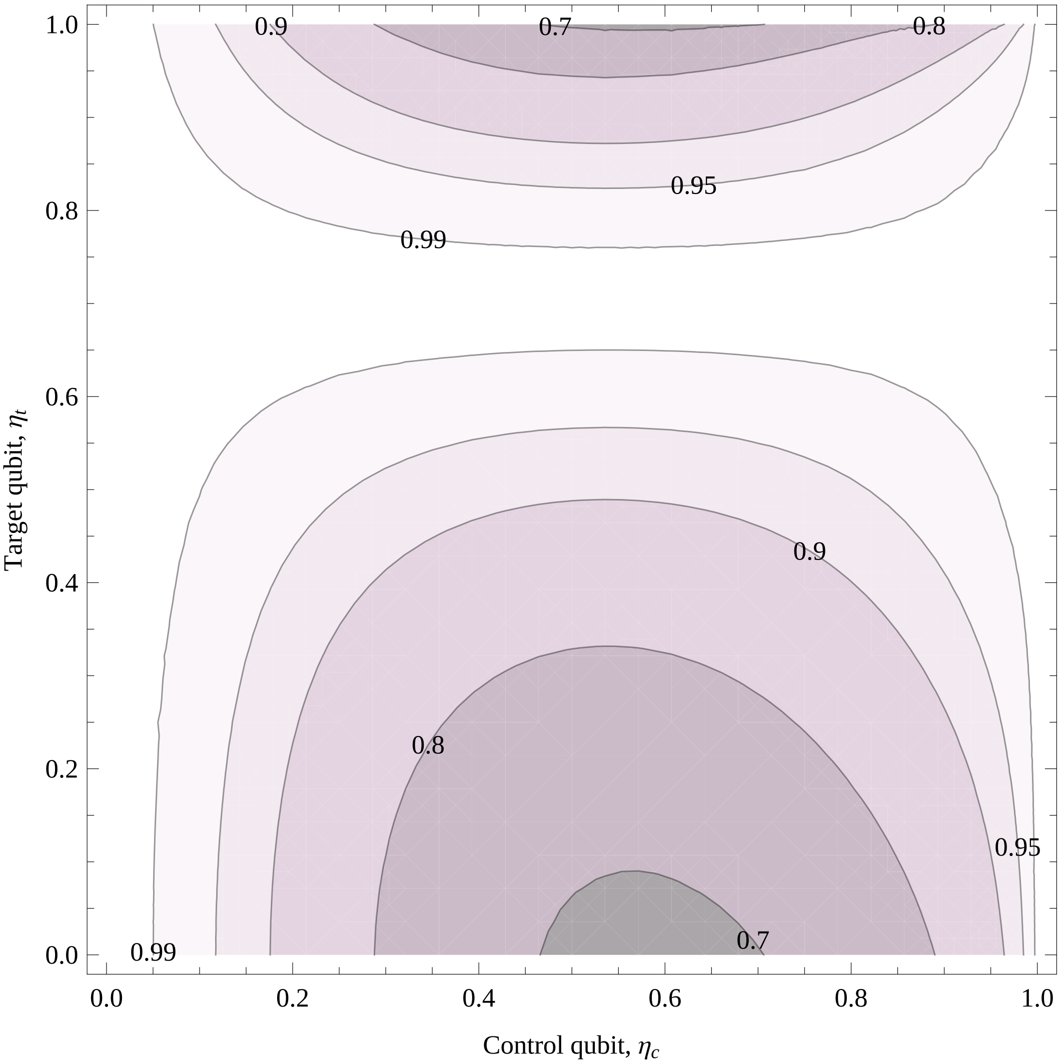

Figure 5.7: *Simulating the impact of four-photon noise on the output state fidelity for arbitrary product state inputs. The weights, η_c and η_t (axes), define the input state of control and target qubit, respectively. The labels denote the output state fidelity in the enclosed region, where a lighter shading corresponds to a better fidelity. In this plot the signal-to-noise ratio, p/q, is set to 1 and the* CNOT *is assumed to be ideal.*

5.4 Applications

We propose two applications adapted to the two-qubit quantum computer: A version of the algorithm for solving systems of linear equations [8] and a circuit for simulating the quantum Heisenberg XY model in a transverse magnetic field.

5.4.1 Quantum algorithm for systems of linear equations

The algorithm for solving systems of linear equations is a versatile addition to list of quantum algorithms that achieve an exponential speedup over their best known classical counterparts.

Reviewing the algorithm

The solution to a system of linear equations, represented by matrix A and a vector b, is given by

$$x = A^{-1} b \tag{5.5}$$

We intend to implement this procedure on a quantum computer, therefore the registers x and b must be valid quantum states and A a Hermitian operator[3]. Without loss of generality they can be rescaled to have $||b|| = ||x|| = 1$. Then, given $|b\rangle$, we seek

$$|x\rangle = \frac{A^{-1}|b\rangle}{||A^{-1}|b\rangle||} \tag{5.6}$$

In the eigenbasis of A, $|u_1\rangle, ..., |u_N\rangle$ with eigenvalues $\lambda_1, ..., \lambda_N$

$$|b\rangle = \sum_{i=1}^{N} \beta_i |u_i\rangle \ , \tag{5.7}$$

and using the spectral decomposition

$$A^{-1} = \sum_{j=1}^{N} \frac{1}{\lambda_j} |u_j\rangle \langle u_j| \ , \tag{5.8}$$

the solution is, up to normalization,

$$|x\rangle = \sum_{i,j=1}^{N} \frac{1}{\lambda_j} \beta_i |u_j\rangle \langle u_j|u_i\rangle = \sum_{j=1}^{N} = \frac{1}{\lambda_j} \beta_j |u_j\rangle \ . \tag{5.9}$$

To prepare this state we apply the phase estimation algorithm [78, 79] to $|b\rangle$ using the the unitary $U = e^{2\pi i A}$ and add an empty register for storing the eigenvalue $|\lambda_i\rangle$

$$\sum_{j=1}^{N} \beta_j |u_j\rangle |\lambda_j\rangle \ . \tag{5.10}$$

---

[3] A should also be sparse and well-conditioned, see [8] for full list of requirements.

This implies that the eigenvalues of A lie in the interval $(0;1)$, which is always achievable by rescaling. To bring it into the desired form (5.9) we need to implement the nonunitary map $|\lambda_j\rangle \to \frac{1}{\lambda_j}|\lambda_j\rangle$. This operation can be accomplished with the help of an ancilla qubit and postselection. A controlled rotation

$$R_y(\theta) = e^{-i\mathrm{Y}\theta/2} = \begin{pmatrix} \cos\frac{\theta}{2} & -\sin\frac{\theta}{2} \\ \sin\frac{\theta}{2} & \cos\frac{\theta}{2} \end{pmatrix} \tag{5.11}$$

conditioned on the value of $|\lambda_j\rangle$ transforms the ancilla register $|0\rangle$ into

$$\cos\frac{\theta}{2}\,|0\rangle + \sin\frac{\theta}{2}\,|1\rangle \; . \tag{5.12}$$

For our purposes we want

$$\sin\frac{\theta}{2} \overset{!}{=} \frac{C}{\lambda_j} \leq 1 \quad \Rightarrow \quad \theta = 2\,\arcsin\left(\frac{C}{\lambda_j}\right) , \tag{5.13}$$

such that

$$\sum_{j=1}^{N} \beta_j\,|u_j\rangle\,|\lambda_j\rangle \left(\sqrt{1-\frac{C^2}{\lambda_j^2}}\,|0\rangle + \frac{C}{\lambda_j}\,|1\rangle\right) . \tag{5.14}$$

The factor $\sqrt{1-\frac{C^2}{\lambda_j^2}}$ is due to normalization. We then undo the phase estimation. A measurement on the ancilla qubit returning $|1\rangle$, indicates that the state register has taken the form of the solution vector $|x\rangle$. To optimize the success probability we choose C as large as the normalization constraint allows, i.e. $C = \min_j \lambda_j$.

It should be noted that reading out all the components of $|x\rangle$ would require the procedure to be performed at least N times which annihilates the exponential speedup. However, if not $|x\rangle$ itself is of interest, but some expectation value $\langle x|M|x\rangle$ the algorithm remains applicable. For the particular case we seek to implement this has no implication, as the input state $|b\rangle$ is a single qubit.

The simplest case

An implementation on a two-qubit quantum computer restricts A to be a 2×2 matrix. Furthermore, its eigenvalues λ_j must be distinguishable by a single bit. The simplest case is to choose $\lambda_1 = 0.10$ and $\lambda_2 = 0.11$, corresponding to 0.5 and 0.75 in decimal. The phase estimation then needs to read out the second digit, i.e. by applying $U = e^{4\pi i A}$ instead of $U = e^{2\pi i A}$, which would give the first. For $\lambda_1 = \frac{1}{2}$ the rotation is

$$R_y(2\arcsin\frac{C}{\lambda_1}) = R_y(\pi) = -i\mathrm{Y} \quad \text{with} \quad C = \min_j \lambda_j = \frac{1}{2} \, . \tag{5.15}$$

Since $-i\mathrm{Y}\,|0\rangle = |1\rangle$, we can initialize the ancilla as $|1\rangle$ making the rotation obsolete. The map reduces to an identity operation when the eigenvalue qubit is $|0\rangle$ and a $R_y(-2\arccos\frac{2}{3})$ when it is $|1\rangle$. In other words we need to implement a controlled $R_y(-2\arccos\frac{2}{3})$. In a circuit picture it looks like this

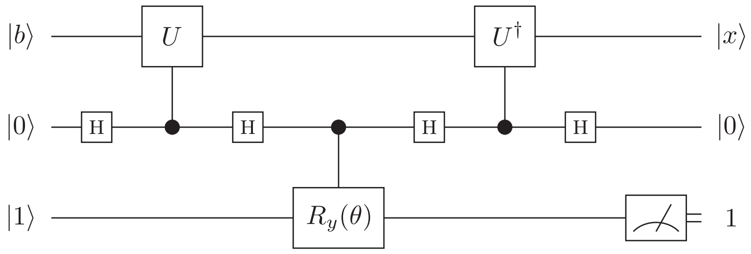
$|b\rangle$
U
$U^\dagger$
$|x\rangle$
$|0\rangle$
H
H
H
H
$|0\rangle$
$|1\rangle$
$R_y(\theta)$
1

where the first line corresponds to the state qubit, the second to the eigenvalue qubit and the third to the ancilla qubit.

We required A to be Hermitian, so there is a unitary R that diagonalizes it

$$A = R^\dagger \begin{pmatrix} \frac{1}{2} & 0 \\ 0 & \frac{3}{4} \end{pmatrix} R \quad \text{and} \quad U = e^{4\pi i A} = R^\dagger \begin{pmatrix} 1 & 0 \\ 0 & -1 \end{pmatrix} R = R^\dagger \mathrm{z} R\,. \tag{5.16}$$

Substituting the controlled version of U

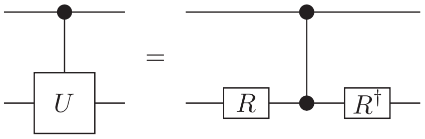

brings us to

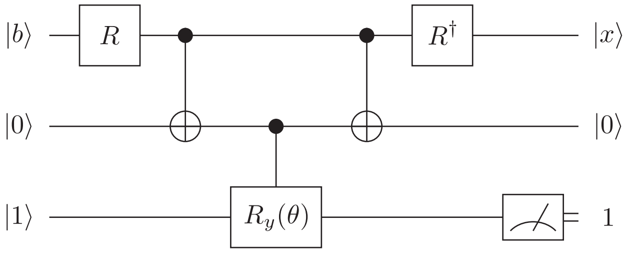
$|b\rangle$
R
$R^\dagger$
$|x\rangle$
$|0\rangle$
$|0\rangle$
$|1\rangle$
$R_y(\theta)$
1

where the identity relation between CSIGN and CNOT was used. The circuit can be further simplified by noting that the control qubit for R_y can be directly obtained from the input line

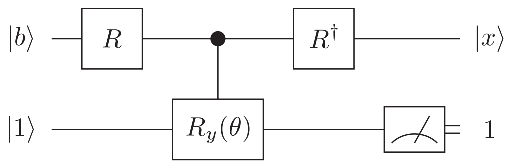
$|b\rangle$
R
$R^\dagger$
$|x\rangle$
$|1\rangle$
$R_y(\theta)$
1

What remains is a two-qubit unitary operation. Hence it can be decompose into a form suitable for the universal two-qubit quantum computer

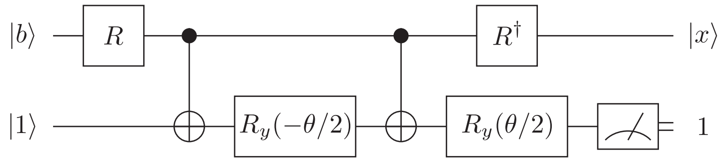
$|b\rangle$
R
$R^\dagger$
$|x\rangle$
$|1\rangle$
$R_y(-\theta/2)$
$R_y(\theta/2)$
1

Comments on the implementation

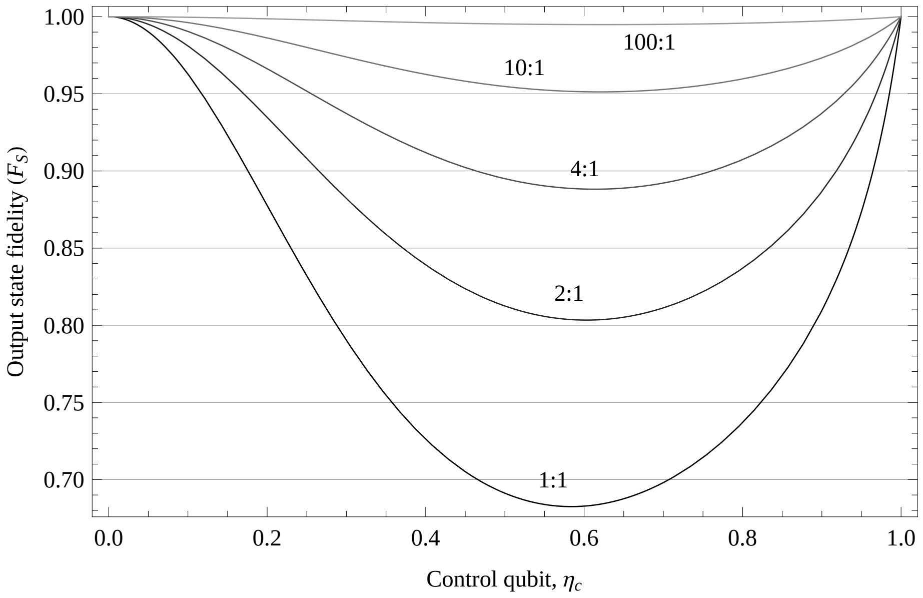

Figure 5.8: *Simulation of the output state fidelity for an arbitrary control qubit* $\eta_c |H\rangle + \nu_c |V\rangle$ *and several signal-to-noise ratios,* $p : q$*. Only the noise introduced from four-photon events is considered. The actual* CNOT *operation is assumed to be ideal and the target qubit is set to* $|V\rangle$ *as required by the circuit. For a 1:1 ratio the fidelity greatly depends on the input state. By increasing it the noise contribution can become arbitrarily small. However, this will result in lower count rates.*

From Figure 5.7 we know that independent of the actual quality of the CNOT gate, the input state does have a considerable influence on the output state fidelity due to spurious four-photon emissions. The proposed demonstration of the algorithm for systems of linear equations could avoid this behaviour by choosing the state of the control qubit $R\,|b\rangle \approx |H\rangle$ or $|V\rangle$. In this way the effect of the four-photon noise can be limited. Alternatively, a better fidelity is achieved by adjusting the signal-to-noise ratio, p/q, yet at the expense of a lower count rate. Figure 5.8 compares several ratios with the target qubit set to $|1\rangle = |V\rangle$ as found in the circuit. Another aspect that will contribute beneficially is to consider that the CNOT gate suggested for this experiment is less error-prone when the control qubit is $|H\rangle$ and the applied operation is the identity.

5.4.2 Simulating the two-qubit Heisenberg XY model

The Hamiltonian of a two-qubit Heisenberg XY model in a transverse field B is

$$H = J_x\,\sigma_x \otimes \sigma_x + J_y\,\sigma_y \otimes \sigma_y + \frac{1}{2}B\,(\mathbb{1} \otimes \sigma_z + \sigma_z \otimes \mathbb{1}), \tag{5.17}$$

where J_x and J_y describe the spin coupling.

In [80] a method for obtaining a unitary transformation U that takes a Hamiltonian to diagonal (noninteracting) form is presented. For the explicit case of the two-qubit XY model, the unitary is

$$U = \begin{pmatrix} \cos\frac{x}{2} & 0 & 0 & \sin\frac{x}{2} \\ 0 & \frac{1}{\sqrt{2}} & \frac{1}{\sqrt{2}} & 0 \\ 0 & -\frac{1}{\sqrt{2}} & \frac{1}{\sqrt{2}} & 0 \\ -\sin\frac{x}{2} & 0 & 0 & \cos\frac{x}{2} \end{pmatrix} \tag{5.18}$$

with $\tan x = \frac{J_x - J_y}{B}$. U maps (5.17) to the free-particle Hamiltonian $\tilde{H} = UHU^\dagger = \omega_1\ \mathbb{1} \otimes \sigma_z + \omega_2\ \sigma_z \otimes \mathbb{1}$, where $\omega_1 = \frac{1}{2}(E_1 - E_2)$ and $\omega_2 = \frac{1}{2}(E_1 + E_2)$ are the quasi-particle energies.

This opens up a number of interesting opportunities: The transformation preserves the complete physical content of H. With the knowledge of U we gain access to all– ground and excited –eigenstates of $H\,|\psi_i\rangle = E_i\,|\psi_i\rangle$, by applying it to the computational basis states

$$|\psi_1\rangle = U\,|00\rangle\ , \tag{5.19}$$

$$|\psi_2\rangle = U\,|01\rangle\ , \tag{5.20}$$

$$|\psi_3\rangle = U\,|10\rangle\ , \tag{5.21}$$

$$|\psi_4\rangle = U\,|11\rangle\ . \tag{5.22}$$

They are

$$|\psi_1\rangle = \cos\frac{x}{2}\,|00\rangle + \sin\frac{x}{2}\,|11\rangle\ , \qquad E_1 = \sqrt{B^2 + (J_x - J_y)^2} \tag{5.23}$$

$$|\psi_2\rangle = \frac{1}{\sqrt{2}}\,(|01\rangle - |10\rangle)\,, \qquad E_2 = -J_x - J_y \tag{5.24}$$

$$|\psi_3\rangle = \frac{1}{\sqrt{2}}\,(|01\rangle + |10\rangle)\,, \qquad E_3 = J_x + J_y \tag{5.25}$$

$$|\psi_4\rangle = -\sin\frac{x}{2}\,|00\rangle + \cos\frac{x}{2}\,|11\rangle\ , \qquad E_4 = -\sqrt{B^2 + (J_x - J_y)^2}\,. \tag{5.26}$$

Without the presence of an external field B the eigenstates are formally equivalent to Bell states. At the same time we gain a procedure of how to experimentally prepare these states with a quantum computer– implement U. Moreover, by bringing H into diagonal form, the external field B, present in the parameter x, can be controlled by single-qubit gates. In particular we can find a decomposition applicable to the universal two-qubit quantum computer [69]

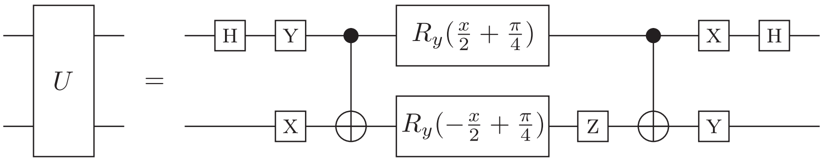
U
=
H
Y
X
$R_y(\frac{x}{2}+\frac{\pi}{4})$
$R_y(-\frac{x}{2}+\frac{\pi}{4})$
Z
X
H
Y

The same circuit can be used to produce superpositions of $|\psi_i\rangle$ and also the thermal state

$$\rho_{\text{th}} = e^{-\frac{H}{kT}} = U\,e^{-\frac{\tilde{H}}{kT}}\,U^\dagger \tag{5.27}$$

by using a mixture of product states as input [80].

Comments on the implementation

When we attempt to use the above circuit for preparing the eigenstates of H, i.e. by applying it to the computational basis states, we are confronted with the difficulty that the single-qubit unitaries in front of the first CNOT map them to states that are particularly susceptible to the discussed four-photon noise (cf. Figure 5.7)

$$(\textsc{y h} \otimes \textsc{x})\ |HH\rangle = |AV\rangle\ , \tag{5.28}$$

$$(\textsc{y h} \otimes \textsc{x})\ |HV\rangle = |AH\rangle\ , \tag{5.29}$$

$$(\textsc{y h} \otimes \textsc{x})\ |VH\rangle = |DV\rangle\ , \tag{5.30}$$

$$(\textsc{y h} \otimes \textsc{x})\ |VV\rangle = |DH\rangle\ . \tag{5.31}$$

It possible to reduce the impact by increasing the signal-to-noise ratio p/q as shown in Figure 5.9.

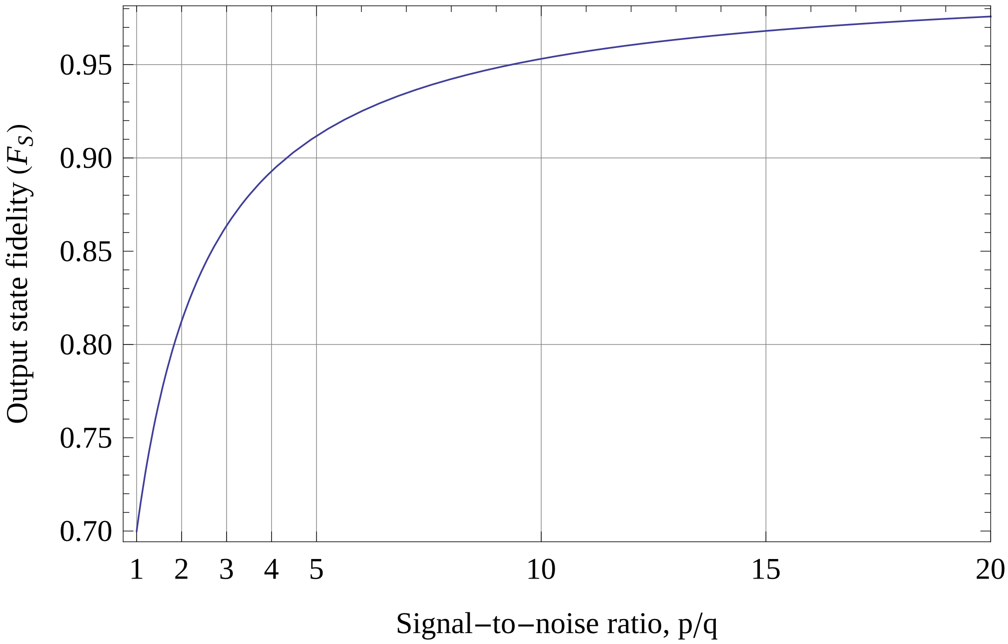

Figure 5.9: *Simulation of the output state fidelity for computational basis states inputs. Again, only the noise introduced from four-photon events is considered and the underlying* CNOT *and single-qubit operations are assumed to be ideal. Increasing the signal-to-noise ratio can attenuate the noise contribution at the expense of a lower count rate.*

Another option reveals itself when we proceed to the next element in the circuit. We realize that the subsequent CNOT transforms these states into the four Bell states,

$$\text{CNOT}\ |AV\rangle = |\psi^-\rangle\ . \tag{5.32}$$

and hence we may skip the entire part including the first CNOT by directly using the entangled states of the SPDC source.

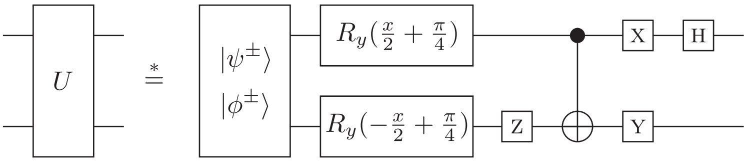
U
$\overset{*}{=}$
$|\psi^\pm\rangle$
$|\phi^\pm\rangle$
$R_y(\frac{x}{2}+\frac{\pi}{4})$
$R_y(-\frac{x}{2}+\frac{\pi}{4})$
Z
X
H
Y

The asterisk (*) is to remind us that this simplification is valid only for certain inputs.

Chapter 6

Conclusion and outlook

In the experimental work accompanying this thesis we have realized a scheme for an interferometric two-qubit gate [54, 55, 56]. Our main objective was to reproduce this gate with attention to quality and stability to be able to later combine it with another two-qubit gate [70, 71], eventually forming a universal two-qubit quantum computer.

After construction, we subjected the gate to a series of tests including a process tomography. We have identified imperfect interference to be the primary source of error for this type of gate. Future optimization will benefit from this knowledge as this aspect can be tested with less effort than required for a full process tomography. Furthermore, the described tests can be adopted as a guideline for evaluating quantum gates in general.

From our discussion in Chapter 5 it is clear that the task of building two consecutive two-qubit gates cannot be reduced to simply duplicating a setup. Many existing architectures prove to be incompatible, which is mostly related to the probabilistic nature of current photon sources, gate architectures and detection devices. In many cases the techniques used to indicate successful operation become unreliable when the setup is extended. All gates are designed to work with a specific number of photons. While a number smaller than the intended is usually innocuous, erratic behaviour stems from supernumerary photons. Possible solutions to these problems lie at both ends of a quantum circuit. Apparently, a deterministic source emitting a precise number of photons would dispose of most of the difficulties. But also detectors that accurately register the number of photons would mean a huge leap forward as they would help to set aside successful from incorrect runs.

Nonetheless, we have argued that a functional two-qubit quantum computer is feasible with current technology.

A notable deficit of the proposed scheme is that the quality of the circuit depends on the input state. For some inputs almost no additional errors are introduced by concatenation, while in other cases the impact will be substantial. We have outlined a way to mitigate this effect by increasing the signal-to-noise ratio, but this path is only applicable if interference is close to perfect.

At the end of this thesis we have compiled two interesting applications suitable for this setup. To provide a basis for their implementation we have included a detailed investigation of the expected errors for both experiments.

Appendix A

Useful tables

HWP(α) $\rightarrow$	0°(0)	22.5°($\frac{\pi}{8}$)	45°($\frac{\pi}{4}$)	67.5°($\frac{3\pi}{8}$)	90°($\frac{\pi}{2}$)
$\|H\rangle = \left(\begin{smallmatrix}1\\0\end{smallmatrix}\right)$	$\|H\rangle$	$\|D\rangle$	$\|V\rangle$	$\|A\rangle$	$\|H\rangle$
$\|V\rangle = \left(\begin{smallmatrix}0\\1\end{smallmatrix}\right)$	$\|V\rangle$	$\|A\rangle$	$\|H\rangle$	$\|D\rangle$	$\|V\rangle$
$\|D\rangle = \frac{1}{\sqrt{2}}\left(\begin{smallmatrix}1\\1\end{smallmatrix}\right)$	$\|A\rangle$	$\|H\rangle$	$\|D\rangle$	$\|V\rangle$	$\|A\rangle$
$\|A\rangle = \frac{1}{\sqrt{2}}\left(\begin{smallmatrix}1\\-1\end{smallmatrix}\right)$	$\|D\rangle$	$\|V\rangle$	$\|A\rangle$	$\|H\rangle$	$\|D\rangle$
$\|R\rangle = \frac{1}{\sqrt{2}}\left(\begin{smallmatrix}1\\i\end{smallmatrix}\right)$	$\|L\rangle$	$\|L\rangle$	$\|L\rangle$	$\|L\rangle$	$\|L\rangle$
$\|L\rangle = \frac{1}{\sqrt{2}}\left(\begin{smallmatrix}1\\-i\end{smallmatrix}\right)$	$\|R\rangle$	$\|R\rangle$	$\|R\rangle$	$\|R\rangle$	$\|R\rangle$

Table A.1: *The effect of rotating the optical axis of a half wave plate in the plain perpendicular to the beam direction with respect to horizontally polarized light.*

QWP(β) $\rightarrow$	0°(0)	45°($\frac{\pi}{4}$)	90°($\frac{\pi}{2}$)	135°($\frac{3\pi}{4}$)	180°(π)
$\|H\rangle = \left(\begin{smallmatrix}1\\0\end{smallmatrix}\right)$	$\|H\rangle$	$\|R\rangle$	$\|H\rangle$	$\|L\rangle$	$\|H\rangle$
$\|V\rangle = \left(\begin{smallmatrix}0\\1\end{smallmatrix}\right)$	$\|V\rangle$	$\|L\rangle$	$\|V\rangle$	$\|R\rangle$	$\|V\rangle$
$\|D\rangle = \frac{1}{\sqrt{2}}\left(\begin{smallmatrix}1\\1\end{smallmatrix}\right)$	$\|L\rangle$	$\|D\rangle$	$\|R\rangle$	$\|D\rangle$	$\|L\rangle$
$\|A\rangle = \frac{1}{\sqrt{2}}\left(\begin{smallmatrix}1\\-1\end{smallmatrix}\right)$	$\|R\rangle$	$\|A\rangle$	$\|L\rangle$	$\|A\rangle$	$\|R\rangle$
$\|R\rangle = \frac{1}{\sqrt{2}}\left(\begin{smallmatrix}1\\i\end{smallmatrix}\right)$	$\|D\rangle$	$\|V\rangle$	$\|A\rangle$	$\|H\rangle$	$\|D\rangle$
$\|L\rangle = \frac{1}{\sqrt{2}}\left(\begin{smallmatrix}1\\-i\end{smallmatrix}\right)$	$\|A\rangle$	$\|H\rangle$	$\|D\rangle$	$\|V\rangle$	$\|A\rangle$

Table A.2: *The effect of a quarter wave plate.*

H/V	D/A	R/L
$\|\psi^-\rangle$	$\|\psi^-\rangle$	$\|\psi^-\rangle$
$\|\psi^+\rangle$	$\|\phi^-\rangle$	$\|\phi^-\rangle$
$\|\phi^-\rangle$	$\|\psi^+\rangle$	$\|\phi^+\rangle$
$\|\phi^+\rangle$	$\|\phi^+\rangle$	$\|\psi^+\rangle$

Table A.3: *Bell states in different computational bases.*

1:2	HWP1	QWP1	HWP2	QWP2
ZZ	**0**	**0**	**0**	**0**
ZY	0	0	0	**45**
XY	**22.5**	0	0	45
XZ	22.5	0	0	**0**
XX	22.5	0	**22.5**	0
ZX	**0**	0	22.5	0
YX	0	**45**	22.5	0
YZ	0	45	**0**	0
YY	0	45	0	**45**

Table A.4: *An efficient wave plate setting for overcomplete two-qubit QST. It is assumed that both outputs of the measurement setup in Figure 2.5 are used. All angles are given in degrees °.*

1:2	H1H2	H1V2	V1H2	V1V2
ZZ	HH	HV	VH	VV
ZY	HR	HL	VR	VL
XY	DR	DL	AR	AL
XZ	DH	DV	AH	AV
XX	DD	DA	AD	AA
ZX	HD	HA	VD	VA
YX	RD	RA	LD	LA
YZ	RH	RV	LH	LV
YY	RR	RL	LR	LL

Table A.5: *Using the wave plate settings of Table A.4 the observed counts correspond to the measurement settings given in this table. When taken as a list from left to right and top to bottom the permutation $\mathcal{P}$ = [1, 2, 21, 22, 5, 6, 3, 4, 23, 24, 7, 8, 13, 14, 17, 18, 9, 10, 15, 16, 19, 20, 11, 12, 29, 30, 25, 26, 33, 34, 31, 32, 27, 28, 35, 36] rearranges the counts into the standard form: HH, HV, HD, HA, HR, HL, VH, ..., RR.*

Appendix B

Source code

Copyright 2011 Yannick Ole Lipp

    This program is free software: you can redistribute it and/or modify
    it under the terms of the GNU General Public License as published by
    the Free Software Foundation, either version 3 of the License, or
    (at your option) any later version.

    This program is distributed in the hope that it will be useful,
    but WITHOUT ANY WARRANTY; without even the implied warranty of
    MERCHANTABILITY or FITNESS FOR A PARTICULAR PURPOSE. See the
    GNU General Public License for more details.

    You should have received a copy of the GNU General Public License
    along with this program. If not, see <http://www.gnu.org/licenses/>.

```
(* ------------------------------------------------------------------------ *)
(* arbitrarymeasurementbasis.nb (Mathematica):
::   returns quarter and half wave plate angles for a measurement
::   along an arbitrary direction on the Bloch sphere, defined by
::
::   (theta, phi) -> cos(theta/2) |H> + exp(i Pi phi) sin(theta/2) |V>
::
::   Experimental setup:
::   |input> --> (QWP)(a) --> (HWP)(b) --> [PBS]
*)
(* ------------------------------------------------------------------------ *)
arbitrarymeasurementbasis[ {theta_, phi_},
                           indegrees_:False ] := Module[
    {thetarad, phirad, hwpangle, qwpangle},

    If[indegrees,
        thetarad = Pi*theta/180; phirad = Pi*phi/180; ,
        thetarad = theta;        phirad = phi;
    ];

    Switch[thetarad,
        (* V *)
        Pi,   qwpangle = 0;    hwpangle = Pi/4,
        (* XY plane *)
        Pi/2, qwpangle = Pi/4; hwpangle = Pi/8 + phirad/4,



        (* General case *)
        _,
        qwpangle = Limit[ArcTan[Tan[x] Cos[phirad]]/2, x -> thetarad];

        hwpangle = 2/4 * ArcTan[
                                (Cos[thetarad] Sin[2 qwpangle] Cos[2 qwpangle] +
                                 Sin[thetarad] (Cos[phirad] Sin[2 qwpangle]^2 +
                                 Sin[phirad] Cos[2 qwpangle]) ) /
                                (1 + Cos[thetarad] Cos[2 qwpangle]^2 +
                                 Sin[thetarad] Sin[2 qwpangle]
                                 (Cos[2 qwpangle] Cos[phirad] - Sin[phirad]) )
                                ];
    ];

    (* Map to positive angles *)
    qwpangle = Mod[qwpangle, 2 Pi];
    hwpangle = Mod[hwpangle, 2 Pi];

    (* Output *)
    If[indegrees,
    {a -> 180*qwpangle/Pi, b -> 180*hwpangle/Pi},
    {a -> qwpangle,        b -> hwpangle}]
]//N;
(* ------------------------------------------------------------------------ *)
(* ^ arbitrarymeasurementbasis.nb                                           *)
(* ------------------------------------------------------------------------ *)
(* ------------------------------------------------------------------------ *)
(* arbitrarytoarbitarystate.nb (Mathematica):
::   returns wave plate angles for transforming an arbitrary state
::   to another arbitrary state on the Bloch sphere, defined by
::
::   (theta, phi) -> cos(theta/2) |H> + exp(i Pi phi) sin(theta/2) |V>
::
::   Experimental setup:
::   |input> --> (QWP)(a) --> (HWP)(b) --> (QWP)(c) --> |target>
*)
(* ------------------------------------------------------------------------ *)
arbitrarytoarbitarystate[ {thetainput_, phiinput_},
                          {thetatarget_, phitarget_},
                          indegrees_:False            ] := Module[
    {thetainputrad, phiinputrad, thetatargetrad, phitargetrad,
     aangle, intermediatea, bangle, cangle, intermediatec},

    If[indegrees,
        thetainputrad = Pi*thetainput/180;   phiinputrad = Pi*phiinput/180;
        thetatargetrad = Pi*thetatarget/180; phitargetrad = Pi*phitarget/180; ,
        thetainputrad = thetainput;          phiinputrad = phiinput;
        thetatargetrad = thetatarget;        phitargetrad = phitarget;
    ];

    Switch[thetainputrad,
        (* V *)
        Pi, aangle = 0; intermediatea = Pi;,

        (* General case *)
        _,
        aangle = Limit[ArcTan[Tan[x] Cos[phiinputrad]]/2, x -> thetainputrad];

        intermediatea = 2 * ArcTan[
                                (Cos[thetainputrad] Sin[2 aangle] Cos[2 aangle] +
                                 Sin[thetainputrad] (Cos[phiinputrad] Sin[2 aangle]^2 +
                                 Sin[phiinputrad] Cos[2 aangle]) ) /
                                (1 + Cos[thetainputrad] Cos[2 aangle]^2 +
                                 Sin[thetainputrad] Sin[2 aangle]
                                 (Cos[2 aangle] Cos[phiinputrad] - Sin[phiinputrad]) )
                                ];
    ];

    Switch[thetatargetrad,
        (* V *)
        Pi, cangle = 0; intermediatec = Pi;,

        (* General case *)
        _,
        cangle = Limit[ArcTan[Tan[x] Cos[phitargetrad]]/2, x -> thetatargetrad];

        intermediatec = 2 * ArcTan[
                                (Cos[thetatargetrad] Sin[2 cangle] Cos[2 cangle] +
                                 Sin[thetatargetrad] (Cos[phitargetrad] Sin[2 cangle]^2 -
                                 Sin[phitargetrad] Cos[2 cangle]) ) /
                                (1 + Cos[thetatargetrad] Cos[2 cangle]^2 +
                                 Sin[thetatargetrad] Sin[2 cangle]
                                 (Cos[2 cangle] Cos[phitargetrad] + Sin[phitargetrad]) )
                                ];
    ];

    bangle = (intermediatea + intermediatec)/4;
    (* Map to positive angles *)
    aangle = Mod[aangle, 2 Pi];
    bangle = Mod[bangle, 2 Pi];
    cangle = Mod[cangle, 2 Pi];

    (* Output *)
    If[indegrees,
    {a -> 180*aangle/Pi, b -> 180*bangle/Pi, c -> 180*cangle/Pi},
    {a -> aangle,        b -> bangle,        c -> 180*cangle}]
]//N;
(* ------------------------------------------------------------------------ *)
(* ^ arbitrarytoarbitarystate.nb                                            *)
(* ------------------------------------------------------------------------ *)
```

List of Figures

1.1 Bloch sphere . . . 3

2.1 Aligning a nonlinear crystal to be used for SPDC. . . . 6
2.2 Aligning a wave plate. . . . 8
2.3 Some applications of wave plates and beam splitters. . . . 10
2.4 Postponed compensation experiment. . . . 11
2.5 Polarization analysis of light . . . 13

3.1 Single-qubit transformation process visualized on the Bloch sphere . . . 19
3.2 Theoretical (cones) and experimental (bars) density matrices of input state $|s'\rangle$. . . . 20
3.3 Theoretical (cones) and experimental (bars) density matrices of the state after applying $U_{qhq} = \textsc{qwp}(\gamma)\,\textsc{hwp}(\beta)\,\textsc{qwp}(\alpha)$ to $|s'\rangle$. The angles α, β and γ were determined by the described method. . . . 21

4.1 Basic idea for the implementation of a CSIGN gate. . . . 25
4.2 Simulating the CNOT process fidelity for a varying transmission probability T_V of the main PDBS. . . . 29
4.3 Simulating the CNOT process fidelity for a varying transmission probability T_H of the attenuation PDBS. . . . 30
4.4 A simulation of the effect of imperfect PDBS on the CNOT process fidelity. 31
4.5 A simulation of the CNOT process fidelity based on the model (4.14) for partial interference. . . . 32
4.6 A detailed sketch of the PDBS-based CNOT gate. . . . 33
4.7 Verifying the coupler stability. . . . 34
4.8 A picture of the completed setup. . . . 36
4.9 Experimentally determined HOM-dip in VV coincidence counting rate. . . 38
4.10 Influence of the SPDC pump laser power on the HOM-dip quality factor. 38
4.11 Experimentally determined CNOT truth table. . . . 40
4.12 A schematic drawing of quantum state tomography. . . . 42
4.13 Simulation of linear entropy and entanglement of formation for the Werner states. . . . 44
4.14 A schematic drawing of quantum process tomography. . . . 46

4.15 Histogram of the changes in the measurement probabilities (experimental data). 48
4.16 Comparing the theoretical CNOT process matrix to the one reconstructed from experimental data. 50
4.17 Relative size of ideally nonzero elements in the experimental CNOT process matrix. 50
4.18 Histogram of the changes in the measurement probabilities (model). . . 51

5.1 The optical elements used in the various CNOT architectures. 55
5.2 Setup **A** — simple destructive CNOT 55
5.3 Setup **B** — CNOT using path encoding 56
5.4 Setup **C** — CNOT using PDBSs 56
5.5 Setup **D** — feed-forwardable CNOT 57
5.6 Experimental implementation of a universal two-qubit quantum computer. 59
5.7 Simulating the impact of four-photon noise on the output state fidelity for arbitrary product state inputs. 62
5.8 Simulation of the output state fidelity for an arbitrary control qubit and several signal-to-noise ratios. 66
5.9 Simulation of the output state fidelity for computational basis states inputs. 69

List of Tables

2.1 How to transform standard bases to the H/V basis using a QWP and a HWP. 8

3.1 Single-qubit gates and how to experimentally realize them using wave plates. 15

4.1 Optimal values of transmission and reflection probabilities for the PDBS to be used in the CSIGN setup. 28
4.2 CSIGN truth table 39
4.3 CNOT truth table 39
4.4 Experimental CNOT truth table. Errors are less than 0.003. 40
4.5 Bell state visibility in the standard bases. 41
4.6 Experimental values of fidelity, linear entropy and entanglement of formation for some exemplary states produced by the CNOT gate. 44

5.1 A side-by-side comparison of linear optics two-qubit gates. 58

A.1 The effect of rotating the optical axis of a half wave plate in the plain perpendicular to the beam direction with respect to horizontally polarized light. 73
A.2 The effect of a quarter wave plate. 73
A.3 Bell states in different computational bases. 74
A.4 An efficient wave plate setting for overcomplete two-qubit QST. 74
A.5 The measurement bases corresponding to the wave plate settings of Table A.4. 74

Bibliography

[1] R. Feynman. Simulating Physics with Computers. *Int. J. Theor. Phys.*, 21:467, 1982. 1

[2] I. L. Chuang, L. M. K. Vandersypen, X. Zhou, D. W. Leung, and S. Lloyd. Experimental realization of a quantum algorithm. *Nature*, 393:143–146, 1998. 1

[3] J. A. Jones, M. Mosca, and R. H. Hansen. Implementation of a quantum search algorithm on a quantum computer. *Nature*, 393:344–346, 1998. 1

[4] L. M. K. Vandersypen, M. Steffen, G. Breyta, C. Costantino, S. Yannoni, M. H. Sherwood, and I. L. Chuang. Experimental realization of shor's quantum factoring algorithm using nuclear magnetic resonance. *Nature*, 414:883–887, 2001. 1

[5] D. Deutsch. Quantum theory, the Church-Turing principle and the universal quantum computer. *Proc. Roy. Soc. A*, 400:97, 1985. 1

[6] P. W. Shor. Polynomial-time algorithms for prime factorization and discrete logarithms on a quantum computer. *SIAM J. Comput.*, 26:1484, 1997. 1

[7] L. K. Grover. A fast quantum mechanical algorithm for database search. *Proc. 28th Ann. ACM Symp. Theor. Comput.*, pages 212–219, 1996. 1

[8] A. W. Harrow, A. Hassidim, and S. Lloyd. Quantum algorithm for linear systems of equations. *Phys. Rev. Lett.*, 103:150502, 2009. 1, 63

[9] A. Broadbent, J. Fitzsimons, and E. Kashefi. Universal blind quantum computation. *Proc. 50th Ann. IEEE Symp. Found. Comput. Sci.*, pages 517–526, 2009. 1

[10] A scheme for efficient quantum computation with linear optics. Quantum algorithm for linear systems of equations. *Nature*, 409:46, 2001. 1

[11] T. C. Ralph, A. G. White, W. J. Munro, and G. J. Milburn. Simple scheme for efficient linear optics quantum gates. *Phys. Rev. A*, 65:12314, 2001. 1

[12] J. D. Franson, M. M. Donegan, M. J. Fitch, B. C. Jacobs, and T. B. Pittman. High-Fidelity Quantum Logic Operators using Linear Optical Elements. *Phys. Rev. Lett.*, 89:137901, 2002. 1

[13] N. Yoran and B. Reznik. Deterministic Linear Optics Quantum Computation with Single Photon Qubits. *Phys. Rev. Lett.*, 91:037903, 2003. 1

[14] J. C. F. Matthews, A. Politi, A. Stefanov, and J. L. O'Brien. Manipulation of multiphoton entanglement in waveguide quantum circuits. *Nature Photon.*, 3:346–350, 2009. 2

[15] A. Politi, M. J. Cryan, J. G. Rarity, S. Yu, and J. L. O'Brien. Silica-on-Silicon Waveguide Quantum Circuits. *Science*, 320:646–649, 2008. 2

[16] M. G. Thompson, A. Politi, J. C. F. Matthews, and J. L. O'Brien. Integrated waveguide circuits for optical quantum computing. *IET Circuits, Devives & Systems*, 5:94–102, 2011. 2

[17] P. G. Kwiat, K. Mattle, H. Weinfurter, and A. Zeilinger. New High-Intensity Source of Polarization-Entangled Photon Pairs. *Phys. Rev. Lett.*, 75:4337–4342, 1995. 2, 5

[18] R. Raussendorf and H. J. Briegel. A One-Way Quantum Computer. *Phys. Rev. Lett.*, 86:5188–5191, 2001. 2, 16

[19] D. Deutsch. Quantum computational networks. *Proc. R. Soc. London A*, 425:73, 1989. 2, 23

[20] D. S. Abrams and S. Lloyd. Simulation of many-body Fermi systems on a quantum computer. *Phys. Rev. Lett.*, 79:2586–2589, 1997. 2, 23

[21] R. Raussendorf, D. E. Browne, and H. J. Briegel. Measurement-based quantum computation on cluster states. *Phys. Rev. A*, 68:022312, 2003. 2, 16

[22] L.-M. Duan and R. Raussendorf. Efficient quantum computation with probabilistic quantum gates. *Phys. Rev. Lett.*, 95:080503, 2005. 2

[23] P. Walther, K. J. Resch, T. Rudolph, E. Schenck, H. Weinfurter, V. Vedral, and A. Zeilinger. Experimental one-way quantum computing. *Nature*, 434:169–176, 2005. 2

[24] R. Prevedel, P. Walther, F. Tiefenbacher, P. Böhi, R. Kaltenbaek, T. Jennewein, and A. Zeilinger. High-speed linear optics quantum computing using active feed-forward. *Nature*, 445:65–69, 2007. 2

[25] I. Buluta and F. Nori. Quantum Simulators. *Science*, 326:517–526, 2009. 2

[26] S. Lloyd. Universal Quantum Simulators. *Science*, 273:1073, 1996. 2

[27] A. Aspuru-Guzik, A. D. Dutoi, P. J. Love, and M. Head-Gordon. Simulated Quantum Computation of Molecular Energies. *Science*, 309:1704–1707, 2005. 2

[28] B. P. Lanyon, J. D. Whitfield, G. G. Gillet, M. E. Goggin, M. P. Almeida, I. Kassal, J. D. Biamonte, M. Mohseni, B. J. Powell, M. Barbieri, A. Aspuru-Guzik, and A. G. White. Towards quantum chemistry on a quantum computer. *Nature Chem.*, 2:106–111, 2010. 2

[29] K. Temme, T. J. Osborne, K. G. Vollbrecht, D. Poulin, and F. Verstraete. Quantum Metropolis sampling. *Nature*, 471:87, 2011. 2

[30] B. Schumacher. Quantum coding. *Phys. Rev. A*, 51:2738–2747, 1995. 2

[31] P. G. Kwiat. Hyper-entangled states. *J. Mod. Opt.*, 44:2173–2184, 1997. 2

[32] Wei-Bo Gao, Chao-Yang Lu, Xing-Can Yao, Ping Xu, Otfried Gühne, Alexander Goebel, Yu-Ao Chen, Cheng-Zhi Peng, Zeng-Bing Chen, and Jian-Wei Pan. Experimental demonstration of a hyper-entangled ten-qubit Schrödinger cat state. *Nature Phys.*, 6:331–335, 2010. 2

[33] P. Kok, W. J. Munro, K. Nemoto, T. C. Ralph, J. P. Dowling, and G. J. Milburn. Linear optical quantum computing with photonic qubits. *Rev. Mod. Phys.*, 79:135–174, 2007. 5

[34] M. Fox. *Quantum Optics.* Oxford University Press, New York, 2006. 5, 45

[35] L. Mandel and E. Wolf. *Optical Coherence and Quantum Optics.* Cambridge University Press, 1995. 5

[36] G. Weihs. *Ein Experiment zum Test der Bellschen Ungleichung unter Einsteinscher Lokalität.* PhD thesis, Universität Wien, 2005. 5, 6

[37] N. Kiesel. *Experiments on Multiphoton Entanglement.* PhD thesis, Ludwig-Maximilians-Universität München, 2007. 5, 30

[38] S. Barz. Eine Quelle polarisationsverschränkter Photonenpaare für das physikalische Praktikum für Fortgeschrittene, 2008. 6

[39] W. P. Grice and I. A. Walmsley. Spectral information and distinguishability in type-II down-conversion with broadband pump. *Phys. Rev. A*, 56:1627, 1997. 6

[40] W. Demtröder. *Experimentalphysik 2.* Springer-Verlag, Berlin Heidelberg New York, 2004. 7, 11

[41] N. Langford. *Encoding, Manipulating and Measuring Quantum Information in Optics.* PhD thesis, The University of Queensland, 2007. 7, 41, 43, 45

[42] C. K. Hong, Z. Y. Ou, and L. Mandel. Measurement of subpicosecond time intervals between two photons by interference. *Phys. Rev. A*, 59:2044–2046, 1992. 9

[43] T. B. Pittman, D. V. Strekalov, A. Migdall, M. H. Rubin, A. V. Sergienko, and Y. H. Shih. Can Two-Photon Interference be Considered the Interference of Two Photons? *Phys. Rev. Lett.*, 77:1917–1920, 1996. 9, 11

[44] S. Lehar. An Intuitive Explanation of Fourier Theory. http://sharp.bu.edu/ slehar/fourier/fourier.html. 11

[45] P. L. Ramazza, S. Ducci, A. Zavatta, M. Bellini, and F. T. Arecchi. Second-harmonic generation from a picosecond Ti:Sa laser in LBO: conversion efficiency and spatial properties. *Appl. Phys. B*, 75:53–58, 2002. 11

[46] Newport. Strahlformung mit Zylinderlinsen. http://www.newport.com/Strahlformung-mit-Zylinderlinsen/144888/1031/content.aspx. 11

[47] Newport. Polarization in Fiber Optics. http://www.newport.com/Tutorial-Polarization-in-Fiber-Optics/849671/1033/content.aspx. 12

[48] R. H. Hadfield. Single-photon detectors for optical quantum information applications. *Nature Photon.*, 3:696–705, 2009. 13

[49] *In preparation.* 16

[50] Inc. Wolfram Research. JohnsonDistribution. http://reference.wolfram.com/mathematica/ref/JohnsonDistribution.html. 18

[51] M. A. Nielsen and I. L. Chuang. *Quantum Computation and Quantum Information.* Cambridge University Press, Cambridge, 2000. 23, 41, 45, 46

[52] D. Gottesman. *The Heisenberg Representation of Quantum Computers.* arXiv:quant-ph/9807006. 23

[53] D. Gottesman. *Stabilizer codes and quantum error correction.* PhD thesis, California Institute of Technology, 2003. arXiv:quant-ph/9705052. 23

[54] N. K. Langford, T. J. Weinhold, R. Prevedel, K. J. Resch, A. Gilchrist, J. L. O'Brien, G. J. Pryde, and A. G. White. Demonstration of a Simple Entangling Optical Gate and Its Use in Bell-State Analysis. *Phys. Rev. Lett.*, 95:210504, 2005. 24, 41, 55, 56, 71

[55] N. Kiesel, C. Schmid, U. Weber, R. Ursin, and H. Weinfurter. Linear Optics Controlled-Phase Gate Made Simple. *Phys. Rev. Lett.*, 95:210505, 2005. 24, 30, 55, 56, 71

[56] R. Okamoto, H. F. Hofmann, S. Takeuchi, and K. Sasaki. Demonstration of an Optical Quantum Controlled-NOT Gate without Path Interference. *Phys. Rev. Lett.*, 95:210506, 2005. 24, 55, 56, 71

[57] U. Weber. Das optische Phasengatter und Beobachtung eines vier-Photonen Cluster-Zustands, 2005. 30, 32, 34, 35, 37

[58] A. G. White, A. Gilchrist, G. Pryde, J. L. O'Brien, M. Bremner, and N. K. Langford. Measuring two-qubit gates. *J. Opt. Soc. Am. B*, 24:172–183, 2007. 39, 46

[59] P. Walther and A. Zeilinger. Experimental realization of a photonic bell-state analyser. *Phys. Rev. A*, 72:010302, 2005. 41

[60] W. K. Wootters and W. H. Zurek. A single quantum cannot be cloned. *Nature*, 299:802–803, 1982. 41

[61] D. James, P. Kwiat, W. Munro, and A. White. Measurement of qubits. *Phys. Rev. A*, 64:52312, 2001. 41, 42

[62] M. B. Plenio and S. Virmani. An introduction to entanglement measures. 2006. arXiv:quant-ph/0504163. 43

[63] W. K. Wootters. Entanglement of formation of an arbitrary state of two qubits. *Phys. Rev. Lett.*, 80:2245–2248, 1998. 43

[64] P. Kok and B. W. Lovett. *Optical Quantum Information Processing.* Cambridge University Press, Cambridge, 2010. 43

[65] A. Gilchrist, N. K. Langford, and M. A. Nielsen. Distance measures to compare real and ideal quantum processes. *Phys. Rev. A*, 71:062310, 2005. 49

[66] G. Vidal and C. M. Dawson. Universal quantum circuit for two-qubit transformations with three controlled-NOT gates. *Phys. Rev. A*, 69:010301, 2004. 53

[67] F. Vatan and C. Williams. Optimal quantum circuits for general two-qubit gates. *Phys. Rev. A*, 69:032315, 2004. 53

[68] V. V. Shende, S. S. Bullock, and I. L. Markov. Minimal universal two-qubit controlled-NOT-based circuits. *Phys. Rev. A*, 69:062321, 2004. 53

[69] I. Kassal. *Quantum Computation for Chemical Problems.* PhD thesis, Harvard University Cambridge, Massachusetts, 2003. 54, 68

[70] T. B. Pittman, B. C. Jacobs, and J. D. Franson. Probabilistic quantum logic operations using polarizing beam splitters. *Phys. Rev. A*, 64:062311, 2001. 55, 57, 71

[71] T. C. Ralph, N. K. Langford, T. B. Bell, and A. G. White. Realization of a Photonic Controlled-NOT Gate Sufficient for Quantum Computation. *Phys. Rev. Lett.*, 93:020504, 2004. 55, 57, 71

[72] T. C. Ralph, N. K. Langford, T. B. Bell, and A. G. White. Linear optical controlled-not gate in the coincidence basis. *Phys. Rev. A*, 65:062324, 2002. 55, 56

[73] J. L. O'Brien, G. J. Pryde, A. G. White, T. C. Ralph, and D. Branning. Demonstration of an all-optical quantum controlled-NOT gate. *Nature*, 426:264–267, 2003. 55, 56

[74] H. F. Hofmann and S. Takeuchi. Quantum phase gate for photonic qubits using only beam splitters and postselection. *Phys. Rev. A*, 66:024308, 2002. 55, 56

[75] W. Wieczorek, R. Krischek, N. Kiesel, P. Michelberger, G. Tóth, and H. Weinfurter. Experimental entanglement of a six-photon symmetric dicke state. *Phys. Rev. Lett.*, 103:020504, 2009. 58

[76] S. Barz, G. Cronenberg, A. Zeilinger, and P. Walther. Heralded generation of entangled photon pairs. *Nature Photon.*, 4:553, 2010. 58

[77] C. Schmid. *Multi-photon entanglement and applications in quantum information.* PhD thesis, Ludwig-Maximilians Universität, München, 2008. 60

[78] D. S. Abrams and S. Lloyd. Simulation of Many-Body Fermi Systems on a Universal Quantum Computer. *Phys. Rev. Lett.*, 79:2586, 1997. 63

[79] D. S. Abrams and S. Lloyd. Quantum Algorithm Providing Exponential Speed Increase for Finding Eigenvalues and Eigenvectors. *Phys. Rev. Lett.*, 83:5162, 1999. 63

[80] F. Verstraete, J. I. Cirac, and J. I. Latorre. Quantum circuits for strongly correlated quantum systems. *Phys. Rev. A*, 79:032316, 2009. 67, 68

Acknowledgements

I am grateful to my supervisor Anton Zeilinger for offering me the opportunity to become part of the Vienna quantum group and participate in scientific research.

Likewise, I owe great thanks to Philip Walther for his confidence and support. He has always been available for a chat and was a fountain of helpful ideas. Furthermore, he deserves my gratitude for proofreading and constant feedback on my thesis.

In my time here I have benefited greatly from the expertise and guidance of Stefanie Barz. I would like to give a special thanks to her for invaluable discussions and showing me the nuts and bolts of everyday's lab work.

Thanks to Jie Zhang who contributed a large portion of her time in the process of obtaining an explicit solution on how to use wave plates for arbitrary unitaries. An equal share of gratitude belongs to Martin Ringbauer for his assistance in finding a numerical solution to this problem and who has always been available when I needed a helping hand in the lab.

I would also like to value the efforts of Johannes Kofler, Nathan Langford and Sven Ramelow for discussing with me the subtleties of quantum process tomography.

Ivan Kassal and Borivoje Dakic, both indispensable for providing the theoretical background to the two-qubit quantum computer and possible applications— my thanks to you.

I was fortunate to have great collegueas all around me and I am thankful to everybody who has helped me out on numerous occasions.

This work was supported by the *Fonds zur Förderung der wissenschaftlichen Forschung* (Grant No. `FWF SFB F 4007-N16`) and the *European Research Council* (Grant No. `QIT4QAD-227844`).

Experimental realization of an interferometric quantum circuit to increase the computational depth

Abstract

A quantum computer is a versatile tool whose applications extend beyond the field of physics. In this work we describe a scheme and realize missing building blocks of a universal two-qubit quantum computer within the framework of linear optics and photonic qubits.

To this end we compare several existing two-qubit gate architectures and examine their suitability for concatenation. We discuss experimental challenges and motivate the reasons for our choice. Simultaneously, we find methods to minimize the required resources on the quantum part without compromising the universality of the approach.

Elaborating on existing infrastructure in our lab, we complete the list of required components and perform extensive characterization thereof. In particular a quantum process tomography of a Controlled-NOT gate is shown.

Furthermore we present applications that can be realized with our setup. To the prospect of quantum computation we outline a minimal implementation of the algorithm for solving systems of linear equations. On the simulation side, we explain how to use our quantum computer to simulate a two-qubit Heisenberg XY model in a transverse field. The quantum simulator allows to prepare ground and excited states as well as superpositions and thermal states. Moreover, the system parameters are controllable by single-qubit operations only.

Experimentelle Realisierung eines interferometrischen Quantengatters zur Erweiterung der Berechnungsmöglichkeiten

Zusammenfassung

Ein Quantencomputer bietet Anwendungsmöglichkeiten über das Feld der Physik hinaus. In dieser Arbeit beschreiben wir ein Konzept und realisieren fehlende Bestandteile eines universellen Zwei-Qubit-Quantencomputers mit den Möglichkeiten von linearer Optik und Photonen als Qubits.

Hierzu vergleichen wir verschiedene existierende Realisierungen von Zwei-Qubit-Gattern und untersuchen die Möglichkeit mehrere davon hintereinander zu setzen. Wir betrachten die experimentellen Schwierigkeiten und argumentieren unsere Wahl. Gleichzeitig suchen wir nach Wegen, wie die benötigten Resourcen auf der Quanten-Seite minimiert werden können, ohne dadurch die Universalität des Ansatzes zu beeinträchtigen.

Aufbauend auf der bestehenden Infrastruktur in unserem Labor vervollständigen wir die Liste der notwendigen Bauteile und führen eine umfassende Analyse dieser durch. Insbesondere machen wir eine Prozess-Tomografie eines Controlled-NOT Gatters.

Im Anschluss daran eröffnen wir Anwendungen, die sich mit diesem Quantencomputer bewerkstelligen lassen. Im Rahmen von „Quantum Computation“ beschreiben wir eine minimale Implementierung des Algorithmus zur Lösung von linearen Gleichungssystemen. Auf dem Gebiet der Simulation zeigen wir, wie der Quantencomputer dazu verwendet werden kann das Zwei-Qubit Heisenberg XY Model bei Vorhandensein eines transversalen Feldes zu simulieren. Dies ermöglicht es den Grundzustand und die angeregeten Zustände zu präparieren, aber auch Superpositionen dieser und thermische Zustände. Außerdem können die Systemparameter allein durch Ein-Qubit-Gatter kontrolliert werden.

Curriculum Vitae

Yannick Ole Lipp

Contact

Institute for Quantum Optics | Nanophysics | Information

Faculty of Physics

University of Vienna

Boltzmanngasse 5, 1090 Wien (Austria)

yannick-ole.lipp@univie.ac.at

+43 (0) 1 4277 72567

Education

1998-2006	Bundesgymnasium Baden Biondekgasse
July 2002	Summer School, Cambridge (UK)
March 2005	Costa Mesa High School, CA (USA)
2006	Matura, Bundesgymnasium Baden Biondekgasse
2006 – 2011	Study of Physics, University of Vienna
2010 – present	Diploma thesis, University of Vienna

Version: 2011-11